

ESD-TR-75-362

MTR-3073

ECB LIST

DEFIC II No. 84070

Copy No. 1 of 2

INTENSIFIED SILICON DIODE-ARRAY
TARGET TV-CAMERA TUBE (EBSICON);
DESCRIPTION AND MATHEMATICAL MODEL
cys.

JANUARY 1976

Prepared for

DEPUTY FOR SURVEILLANCE AND NAVIGATION SYSTEMS
ELECTRONIC SYSTEMS DIVISION
AIR FORCE SYSTEMS COMMAND
UNITED STATES AIR FORCE
Hanscom Air Force Base, Bedford, Massachusetts



Approved for public release;
distribution unlimited.

Project No. 6290
Prepared by
THE MITRE CORPORATION
Bedford, Massachusetts
Contract No. F19628-76-C-0001

ADA020994

When U.S. Government drawings, specifications, or other data are used for any purpose other than a definitely related government procurement operation, the government thereby incurs no responsibility nor any obligation whatsoever; and the fact that the government may have formulated, furnished, or in any way supplied the said drawings, specifications, or other data is not to be regarded by implication or otherwise, as in any manner licensing the holder or any other person or corporation, or conveying any rights or permission to manufacture, use, or sell any patented invention that may in any way be related thereto.

Do not return this copy. Retain or destroy.

REVIEW AND APPROVAL

This technical report has been reviewed and is approved for publication.

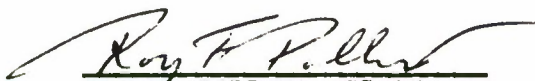


JOHN E. DUNKLE, Maj
GEODSS Project Manager



JAMES E. TROUTMAN, 1Lt
GEODSS Project Engineer

FOR THE COMMANDER



ROY F. POLLINO, GS-15
System Program Director
Weather Instrumentation SPO
Deputy for Surveillance and Navigation Systems

UNCLASSIFIED

SECURITY CLASSIFICATION OF THIS PAGE (When Data Entered)

REPORT DOCUMENTATION PAGE		READ INSTRUCTIONS BEFORE COMPLETING FORM
1. REPORT NUMBER FSD-TR-75-362	2. GOVT ACCESSION NO.	3. RECIPIENT'S CATALOG NUMBER
4. TITLE (and Subtitle) INTENSIFIED SILICON DIODE-ARRAY TARGET TV-CAMERA TUBE (EBSICON); DESCRIPTION AND MATHEMATICAL MODEL		5. TYPE OF REPORT & PERIOD COVERED
7. AUTHOR(s) K. F. Muller G. O. Sauermann		6. PERFORMING ORG. REPORT NUMBER MTR-3073
9. PERFORMING ORGANIZATION NAME AND ADDRESS The MITRE Corporation Box 208 Bedford, MA 01730		8. CONTRACT OR GRANT NUMBER(s) F19628-76-C-0001
11. CONTROLLING OFFICE NAME AND ADDRESS Deputy for Surveillance and Navigation Systems Electronic Systems Division, AFSC Hanscom Air Force Base, Bedford, MA 01731		10. PROGRAM ELEMENT, PROJECT, TASK AREA & WORK UNIT NUMBERS Project No. 6290
14. MONITORING AGENCY NAME & ADDRESS (if different from Controlling Office)		12. REPORT DATE JANUARY 1976
		13. NUMBER OF PAGES 125
		15. SECURITY CLASS. (of this report) UNCLASSIFIED
		15a. DECLASSIFICATION / DOWNGRADING SCHEDULE
16. DISTRIBUTION STATEMENT (of this Report) Approved for public release; distribution unlimited.		
17. DISTRIBUTION STATEMENT (of the abstract entered in Block 20, if different from Report)		
18. SUPPLEMENTARY NOTES		
19. KEY WORDS (Continue on reverse side if necessary and identify by block number) CAMERA TUBES OPTICAL GAIN EBSICON PHOTON NOISE IMAGE INTENSIFICATION POINT SOURCE DETECTION INTENSIFIED VIDICON SILICON DIODE STORAGE TARGET		
20. ABSTRACT (Continue on reverse side if necessary and identify by block number) In this document the mechanical configuration and the electrical operation of a low light level TV scanning image tube which incorporates high optical gain and image storage is described. The physical phenomena associated with these properties are described. From analytical descriptions of the phenomena, a mathematical model		

is developed. The computer program implementations of the model provide economical tools for overall system design considerations. These implementations of the model are flexible enough to encompass all sensor tube characteristics and their operating modes conceivable at this time. Where sufficiently accurate tube and operating parameters were available, comparisons of the model performance with experimental data showed very good quantitative agreement.

ACKNOWLEDGEMENTS

This report has been prepared by The MITRE Corporation under Project 6290. The contract is sponsored by the Electronic Systems Division, Air Force Systems Command, Hanscom Air Force Base, Massachusetts.

The authors want to thank Mr. James E. Barry of the MITRE Corporation for many helpful contributions to, and his continued constructive critical review of, the material presented in this report. Additionally, the authors want to thank the following persons who, on various occasions, assisted with helpful discussions and the provision of useful data:

Dr. R. D. Graft, Mr. R. Franseen and Mr. R. L. Brooks from Army Night Vision Laboratory; Mr. G. J. Sandorfi from Itek Corporation; Dr. J. A. Hall, Dr. A. B. Laponski, and Mr. F. Schaff from Westinghouse Corporation; Dr. D. W. Tufts and Mr. W. V. McCollough from the University of Rhode Island; Mr. S. Campana from the Naval Air Development Center; Mr. M. J. Cantella and Mr. M. W. Stewich from RCA Corporation; and Dr. D. Boone and Dr. J. Hickman from Texas Instruments Corporation.

TABLE OF CONTENTS

LIST OF ILLUSTRATIONS	5
SECTION I INTRODUCTION	7
SECTION II DESCRIPTION OF SENSOR TUBE	10
2.1 MECHANICAL LAYOUT	10
2.1.1 General	10
2.1.2 The Image Section	13
2.1.3 The Storage Target	14
2.1.4 The Read Section	17
2.2 ELECTRICAL OPERATION	17
2.2.1 General	17
2.2.2 Electrical Potentials	19
2.2.3 The Scan Process	22
2.2.4 The Composite Video Signal	23
SECTION III PHYSICAL PHENOMENA IN IMAGE TUBES	25
3.1 THE PHOTOCATHODE	25
3.2 THE GAIN MECHANISM	27
3.3 PHYSICAL EFFECTS CONNECTED WITH CHARGE STORAGE	30
3.4 THE READOUT PROCESS	34
3.4.1 The Equivalent Electrical Circuit	34
3.4.2 The Current/Voltage Characteristic	39
3.4.3 The Approximation of the I/V Characteristic	40
3.4.4 The Signal Current	42
3.4.5 The Lag	44

TABLE OF CONTENTS Continued

SECTION IV	THE MATHEMATICAL TUBE MODEL	46
4.1	DESCRIPTION AND DERIVATION OF EQUATIONS	46
4.1.1	The Readout Process	46
4.1.2	Statistics of Photoelectrons Emitted by the Photocathode	51
4.1.3	Gain and Loss Mechanisms	53
4.1.4	Target Saturation	55
4.2	IMPLEMENTATION IN TERMS OF COMPUTER PROGRAMS	57
4.2.1	Simulation Program	58
4.2.2	Statistical Evaluation Programs	62
4.2.3	Program Listings	68
SECTION V	RESULTS AND COMPARISONS WITH EXPERIMENTAL DATA	69
5.1	FLAT FIELD RESPONSE	69
5.2	POINT SOURCE RESPONSE	74
5.3	POINT SOURCES IN THE PRESENCE OF BACKGROUND NOISE	82
5.4	RESOLUTION	96
SECTION VI	SUMMARY AND RECOMMENDATIONS	103
6.1	SUMMARY	103
6.2	RECOMMENDATIONS	106
APPENDIX A:	SIMULATION PROGRAM LISTINGS	109
APPENDIX B:	STATISTICAL EVALUATION PROGRAM (NO. 1) LISTING	113
APPENDIX C:	STATISTICAL EVALUATION PROGRAM (NO. 2) LISTING	119
REFERENCES		125

LIST OF ILLUSTRATIONS

<u>Figure Number</u>		<u>Page</u>
II-1	Outline of Typical EBSICON	11
II-2	Photograph of Typical EBSICON	12
II-3	Schematic Diagram of Target Structure	15
II-4	Schematic of Diode Array	16
II-5	Basic Structure of Read Section	18
II-6	Typical Potential Distribution Along Axis of EBSICON Tube	21
II-7	Typical Structure of Video Signal	24
III-1	Typical Blooming Characteristics of EBSICON	35
III-2	Equivalent Circuit for Read Process	36
III-3	Distribution of Potentials Across Storage Target	38
III-4	Typical I-V Characteristic of EBSICON Target	41
III-5	Approximation of Experimentally Obtained I-V Characteristic by Function $I_s = I_o(1 - e^{-bV_t})$	43
IV-1	Simulated Video Output	61
V-1	EBSICON Camera Broad Area Transfer Characteristics and Camera Noise	70
V-2	Exposure on Photocathode	72
V-3	Point Response	75
V-4	Experimentally Measured Point Source Response	77
V-5	Point Response	78
V-6	Point Response	79
V-7	Spot Image Response/Broad Area Response vs Spot Size	81
V-8	Point Source Plus Background	83
V-9	Point Source Plus Background	84
V-10	Extended Point Source Plus Background	86
V-11	Measured PDF of Output Noise	88
V-12	PDF's of Signal & Background and Background Alone	89
V-13	PDF's Signal & Background and Background Alone	90
V-14	SNR Transfer From Output to Target	92

LIST OF ILLUSTRATIONS (Continued)

<u>Figure Number</u>		<u>Page</u>
V-15	SNR Transfer From Output to Target	93
V-16	Normalized Autocovariance Function	95
V-17	Typical Response to a Bar Chart	97
V-18	Horizontal Square Wave Response of Different Targets	98
V-19	Point Source Resolution With One Diode Separation	100
V-20	Point Source Resolution With Two Diode Separation	101
V-21	Point Source Resolution With Three Diode Separation	102

SECTION I

INTRODUCTION

The Ground Electro-Optical Deep Space Surveillance System (GEODSS) is tasked to detect faint space objects in orbits exceeding 3000 miles altitude. The surveillance function is performed by optical telescopes equipped with electro-optical sensors. In this application the sensor has to combine high sensitivity with high resolution and a large number of independent resolution cells.

All these requirements call for a TV type sensor; the specific device chosen for the GEODSS system was the FBSICON image tube.

The FBSICON Sensor tube (Electron Bombarded Silicon Target Sensor Tube) combines high sensitivity with high resolution, while maintaining mechanical structural compactness and simplicity. In the special case of space surveillance systems, the high resolution allows for the observation of faint objects in large fields, while the high sensitivity permits operation in the photon-noise limited domain.

Television systems in general are designed to observe scenes with limited ranges in illumination and contrast. Many of the operational parameters of a given TV system are specifically chosen to maximize the output for human observers watching the scenes on phosphor screens. The performance specifications furnished by the manufacturers consist mainly of signal-transfer and modulation transfer curves. This information is usually quite sufficient to design commercial TV systems and, therefore, has become standardized.

In astronomy and space surveillance, however, the objects of interest are point images of very different intensities, riding on a relatively uniform background. In many cases the video signal is processed directly and, therefore, scan patterns, integration times and readout times can be optimized for any given operation. The specific application of EBSICON sensor tubes in the GEODSS system requires the knowledge of tube performance data for a wide variety of operational parameters. Furthermore, the performance of sensor tubes not yet in existence must be projected and their usefulness in various system configurations must be analyzed.

The signal-transfer and sensor modulation-transfer functions do not adequately measure the sensor tube performance in this application or the response characteristics for point images. Furthermore, the literature does not provide guidelines for extrapolating performance characteristics from one set of given operational parameters to another. To accomplish the tasks specifically required in the GEODSS program, it was necessary to develop a mathematical model as a tool, based on the physical effects taking place inside the sensor; and to trace the signal and the noise through the different stages of the sensor, up to and including the video signal output. This mathematical model can be used to aid the laboratory test programs and tube development programs by providing a proper theoretical basis for explanation of observed effects and by predicting the results of the experiments.

The tube model, as it is presented in this report, provides signal transfer characteristics both for point sources and flat fields. It also provides the noise transfer characteristics of EBSICON tubes for photon noise limited inputs for a large variety of operational parameters. The noise characteristics of the output are described in terms of the actual density distribution functions both for the signal and noise. These are of special importance for calculation of detection probability and false alarms. The model gives the proper lag data and such special effects as signal splitting in point images. The model is quantitative, i.e., all the physical parameters, such as material constants and physical dimensions, are chosen to very closely represent actual sensor tubes.

This report consists of four major parts. The mechanical layout and electrical operation is described to put the mathematical model in perspective. The physical effects taking place in the sensor are analyzed to a level of detail which is required to delineate the mathematical model. The physical effects are translated into the mathematical model; the equations derived and solved. And finally, the results, as they are obtained by the mathematical model, are presented and compared with laboratory results.

SECTION II

DESCRIPTION OF SENSOP. TUBE

2.1 MECHANICAL LAYOUT

2.1.1 General

An EBSICON tube consists basically of three parts, all enclosed in one single vacuum envelope: The image section, the storage target and the read section. The overall dimensions of the envelope vary, depending on the specific tube model and manufacturer. A separate cylindrical magnetic focusing and deflection coil assembly surrounds the read section. A detailed outline and a photograph of a typical EBSICON are shown in Figures II-1 and II-2 respectively. Except for the field mesh and the heater of the read gun, the tubes have complete rotational symmetry. All electrodes of the image section and the storage target assembly are mounted on circular disks which are held in place either by glass or ceramic spacer rings. These spacer rings are braced to the circular mounting disks of the electrodes, and form the actual vacuum envelope. The mounting disks protrude beyond the spacers in order to apply the necessary voltages directly. The electron gun is a compact assembly of tightly spaced electrodes connected to a standard pin-type tube socket, which is inserted as a subunit into the end of the read section. This type of design provides for a very rugged and clean device, with short electrical connections and no mechanical adjustments, except for the placement of the magnetic coil assembly.

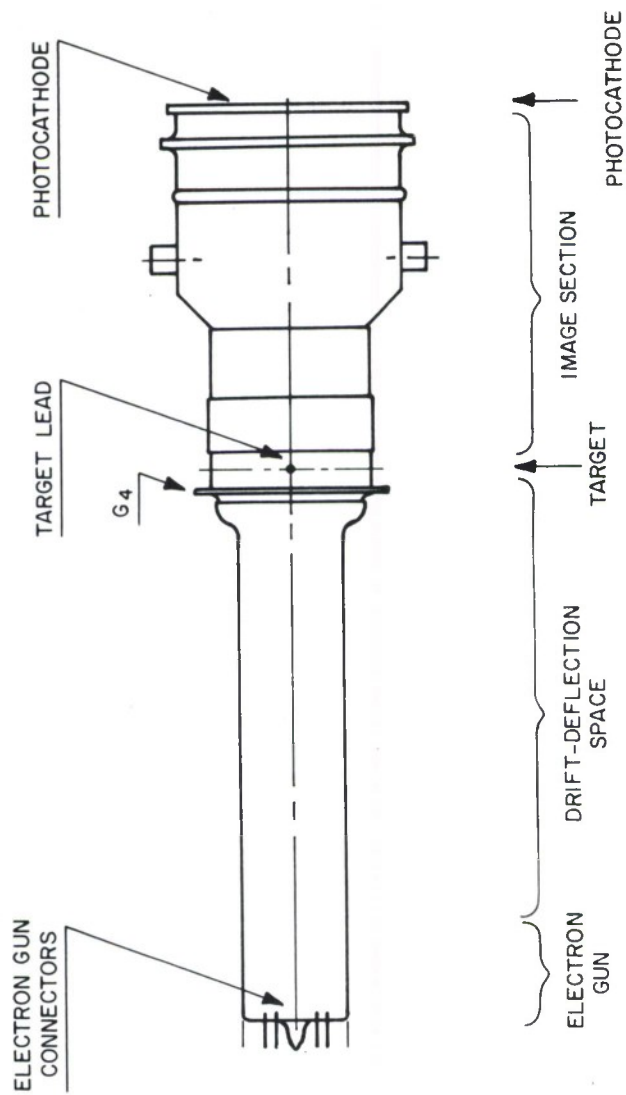


Figure II-1 OUTLINE OF TYPICAL EBSICON

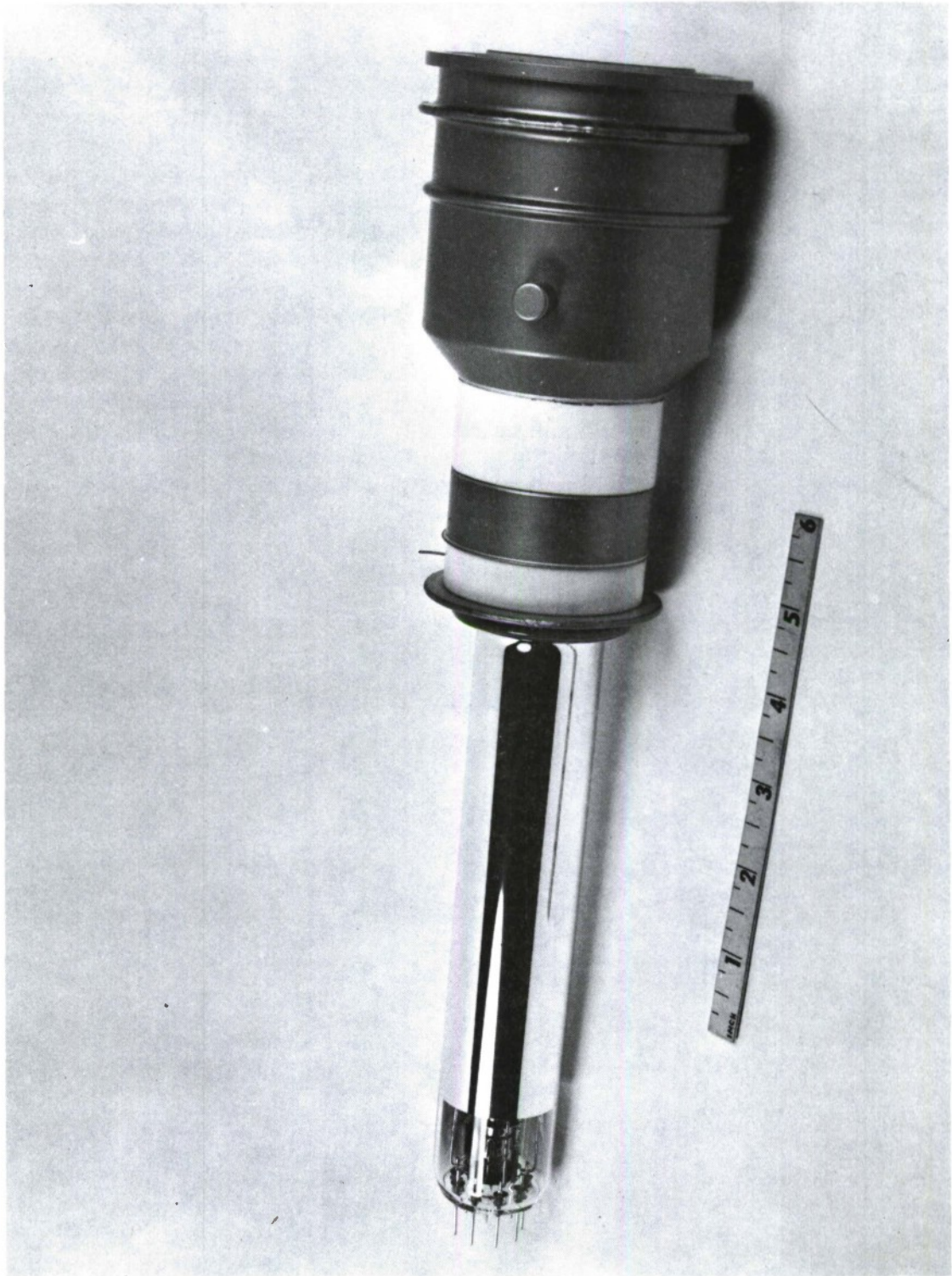


Figure II-2 PHOTOGRAPH OF TYPICAL EBSICON

2.1.2 The Image Section

The image section has the function of converting the spatially-distributed optical image at the photocathode into a charge image which is stored in the target and subsequently read out electronically. The optical image on the photocathode causes photo electrons to be released from the photocathode. The number of photoelectrons released depend on the intensity of the optical radiation. The photo-sensitive material of the photocathode - typically an S20 or S25 - is deposited on the inside of the window of the vacuum envelope in order to allow the released photoelectrons to enter the vacuum section directly and to be imaged on the storage target. The imaging function is performed by the focusing electrode placed opposite the cathode, a cone or funnel-shaped piece of metal, which defines the electrostatic focusing field. Some image sections are equipped with additional electrodes to permit zooming or gating of the image. Behind the focusing electrodes is the storage target assembly, which holds the storage target and some additional components such as the target mesh.

A fiber-optic faceplate is attached to the vacuum envelope and serves as the entrance window, providing a flat surface for the optical image-plane interface and a curved surface on the other side to hold the photocathode. This curvature is necessary to correct for aberration in the image section, which in the case of a flat cathode would reduce the resolution significantly.

2.1.3 The Storage Target

The storage target of an EBSICON tube is a thin silicon wafer which carries an array of small diodes. The detailed target structure and the diode spacing differs depending on the manufacturer; in this report the most advanced target design, the Westinghouse "Deep Etched Gold Capped Diode Array Target" will be described. This type of target structure originated with Westinghouse Corporation and was chosen to become the target for the GFODSS sensor. Sponsored by the Electronic Systems Division of the Air Force, with the technical assistance of the Army Night Vision Laboratory, an EBSICON sensor tube development program was initiated. Texas Instruments is performing the target development and Westinghouse Corporation is handling the tube design to incorporate this type of target.

A square raster of deep furrows is etched into the silicon wafer, which leaves a number of square "mesas". These mesas are doped to form n-p diodes and have a solid gold cap attached, which covers the diode itself and most of the space between the diodes. The diode spacing is 12.5 μm center-to-center (2000 diodes/inch); the gap between gold caps is approximately 2-3 μm . A reflecting n⁺ layer and a separate buffer layer are added to the bulk of the silicon wafer on the opposite side from the diodes. Schematic diagrams of the target structure and of the diode array are shown in Figure II-3 and Figure II-4 respectively.

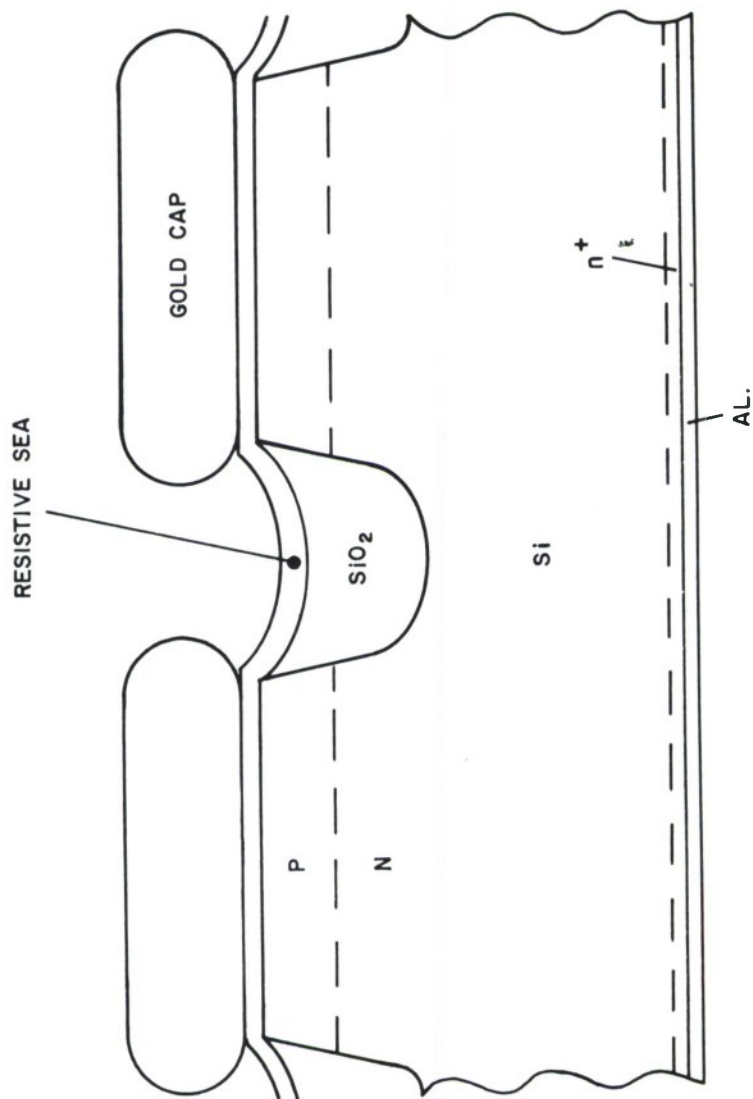
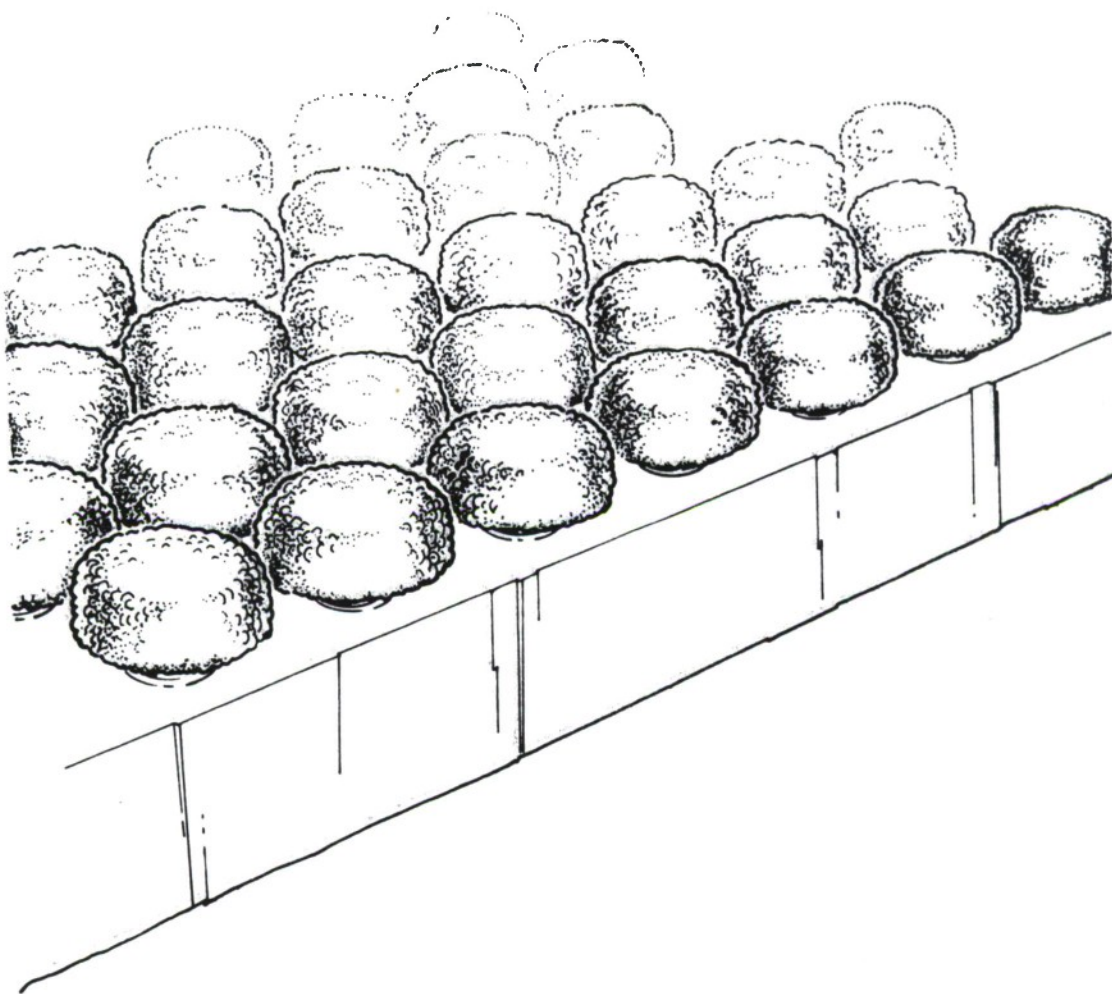


Figure II-3 SCHEMATIC DIAGRAM OF TARGET STRUCTURE



IA-46, 502

Figure II-4 SCHEMATIC OF DIODE ARRAY

2.1.4 The Read Section

The read section consists of the electron gun, the electron drift space and the magnetic deflection coils. The electron gun resembles a triode in principle; electrons emitted by a thermal cathode are focussed by a negative control electrode G_1 and accelerated by a plate at positive potential, G_2 . A fraction of the electrons passes through a small aperture in the positive plate and forms a well-defined, very narrow electron beam. Typical parameters of the beam are approximately 50 μm diameter and 1 to 3 μamp beam current. This electron beam enters the drift space. In this drift space the magnetic deflection of the beam takes place; the beam can be deflected both horizontally and vertically according to the applied magnetic field. The field mesh G_4 at the end of the drift space defines an equipotential surface opposite the target.

In this space between the field mesh and the storage target, the electrons are decelerated and land on the target with velocities close to zero. Since the beam scans the whole target, the spatial uniformity of this deceleration field between target and field mesh has to be maintained with high accuracy. A schematic drawing of the read section is presented in Figure II-5.

2.2 ELECTRICAL OPERATION

2.2.1 General

In this section the general principles for operating an image

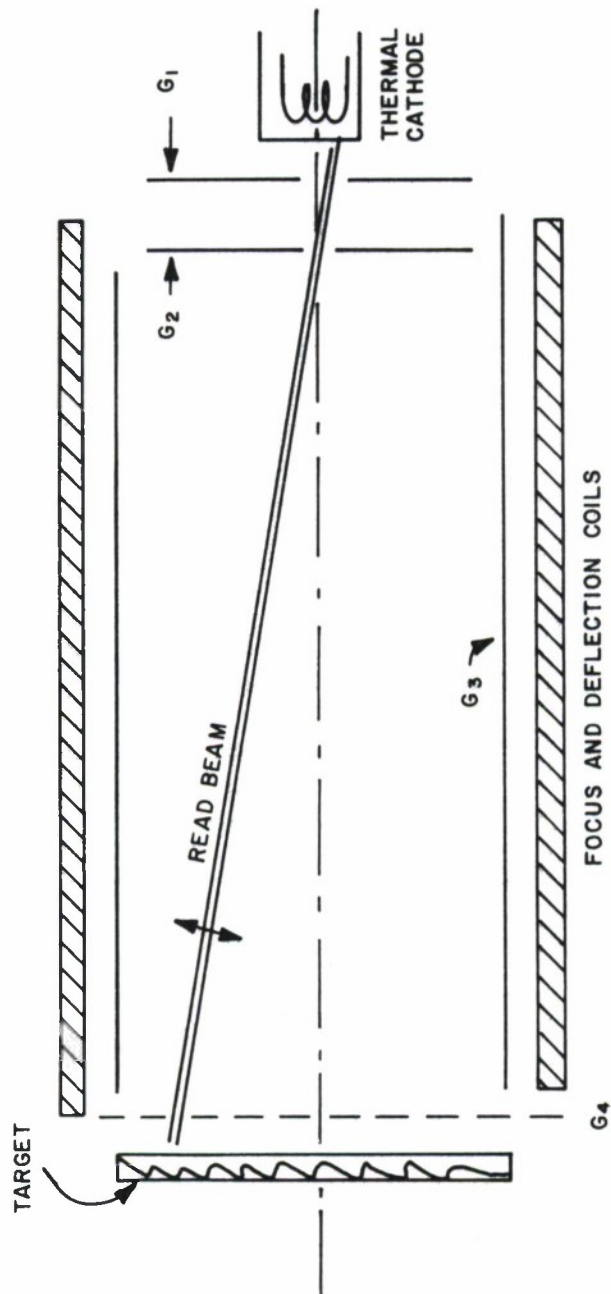


Figure II-5 BASIC STRUCTURE OF READ SECTION

tube will be discussed. A detailed description of the physical effects taking place at the different components of the tube will be presented in Section III of this report. Here they will be sketched only briefly, in order to aid in the understanding of the general sensor operation.

2.2.2 Electrical Potentials

The various electrical potentials as they are applied to the electrodes of the sensor tube are listed below:

<u>Electrode:</u>	<u>Function:</u>	<u>Potential:</u>
Thermal cathode	Emits electrons of read beam	Reference potential
G_1	Focuses and controls read beam	-50 to -150V
G_2	Accelerates read beam electrons	+300 to +350V
G_3	Defines potential in drift space	+750 to 800V
G_4	Defines uniformity of field gradient between drift space and storage target	+800 to 850V
Storage target	Stores photoelectrons for readout	+10V bias on illumination side 0 to +10V on read side
Photocathode	Emits photoelectrons depending on illumination	-14 to -10KV

A potential profile along the axis of the sensor tube is given in Figure II-6.

The following paragraphs give a brief account of the actual sensor tube functions in order to present a basis for the discussion of the physical effects analyzed in the next section.

The incident photon flux releases photoelectrons from the photocathode (which is at 4,000 to 10,000 volts negative). The electrons are accelerated and hit the target with high velocity, releasing additional charge carriers in the bulk of the storage target. The storage target itself is basically a capacitor whose surface facing the photocathode is connected to a low positive DC bias (7-10 volt). The other surface of the target (diode side) is left floating. The first scan of the read beam puts this surface at the potential of the gun cathode. This results in a voltage differential across the target equal to the applied DC bias. If photoelectrons reach the target, the released charge carriers discharge the target capacitors, therefore driving the diode surface which faces the read beam towards the level of the positive DC bias. During the following scan, electrons from the read beam find a positively charged surface and land on it until this surface has again reached gun cathode potential. The resulting current is the observed signal. Since the number of emitted photoelectrons the number of released charge carriers, the reduction in the voltage differential across the storage target, and the number of electrons

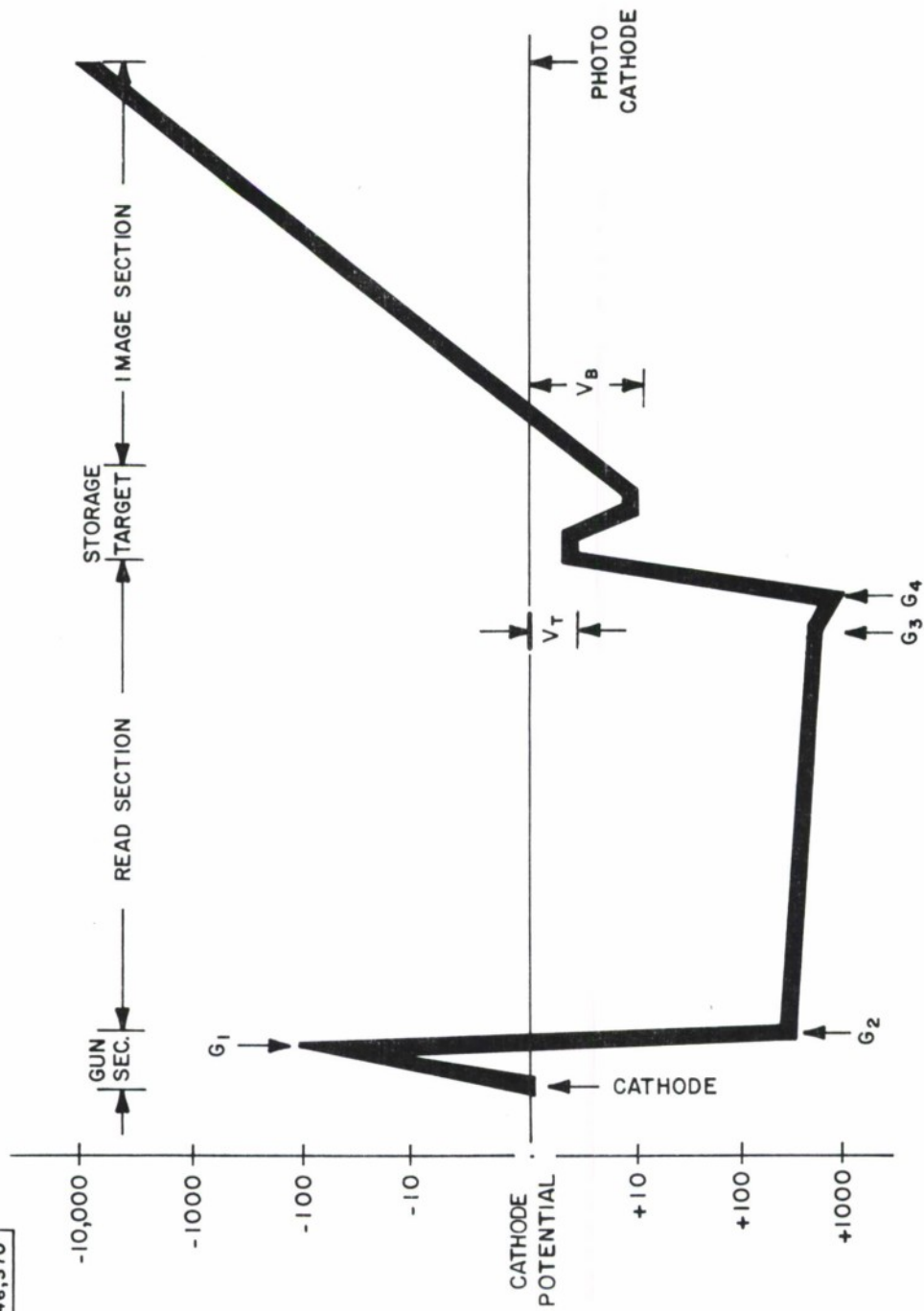


Figure II-6 TYPICAL POTENTIAL DISTRIBUTION ALONG AXIS OF EBSICON TUBE

recharging the storage target are all proportional to each other, the resulting signal current is a linear function of the incident light intensity. In a rough analogy, the storage target can be considered to be equivalent to a large number of individual capacitors in parallel, each capacitor having a variable, illumination-dependent shunt resistor with the read beam acting as a multiplexer switch.

2.2.3 The Scan Process

The electron beam scans the storage target in raster fashion. During readout the read beam travels across the storage target in a horizontal line. After each line scan the beam is retraced very fast compared to the horizontal scan velocity and at the same time is deflected downward to start a new horizontal line. During a given time, $\Delta\tau$, usually referred to as the frame time, the whole target area is scanned and the read beam is returned to the starting point of the raster. The number of scan lines, the size of the scanned target area, and the frame can be varied over a wide range of values.

In commercial television systems, the sensor tube is operated in the continuous mode, i.e., the target is exposed to photoelectrons continuously during the scanning process. In this case the effective integration time ΔT is equal to the frame time $\Delta\tau$. For astronomical and space surveillance work the snapshot or integrating mode is of more interest. In this case the target is exposed to photoelectrons

from the photocathode for an exposure time ΔT (integration time) while the scanning electron beam is turned off. After the target is exposed, the target is read out during a read or frame time $\Delta \tau$. This mode of operation is usually required where the incident light intensities are too low to produce reasonable signal levels in the continuous mode. The ratio $\frac{\Delta T}{\Delta \tau}$ can be set arbitrarily.

2.2.4 The Composite Video Signal

The scanning process converts the time-varying, two-dimensional energy distribution into a time-varying current. In order to reconstruct the original image, the individual scan lines have to be indexed accurately. After the signal leaves the preamplifier (which is mainly used to match impedances), timing pulses of opposite polarity are added to the signal, as well as a pulse to block any signal during line retrace. The pulses are adjusted to define a black level, from which the signal currents or voltages are measured. An example of a typical video output signal is given in Figure II-7.

For the purpose of this report, it is always assumed that the electrical bandwidth of the amplifier chain is sufficient to fully maintain the optical resolution of the device. No degradation of the optical resolution due to other limitations than that of the device itself are considered here.

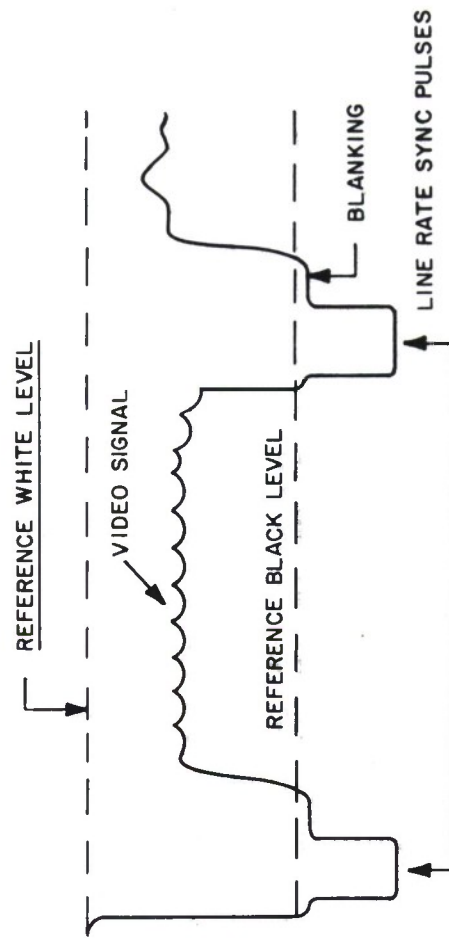


Figure II - 7 TYPICAL STRUCTURE OF VIDEO SIGNAL

SECTION III

PHYSICAL PHENOMENA IN IMAGE TUBES

In order to develop a credible mathematical model for the sensor tube performance, it is necessary to analyze the actual physical effects taking place at various sections of the sensor. This is especially important if a detailed statistical treatment of the signal transfer is required. The gain, storage and scan processes determine the statistical distributions of electrons and have to be incorporated into a final noise analysis. For this reason, four main areas are identified, where major changes in electron distributions occur. These are the photocathode, the gain effects in the target, the electron storage process and the read process. The physical effects taking place in these areas are discussed in the following paragraphs.

3.1 THE PHOTOCATHODE

The optical imaging system forms an image on the faceplate of the sensor tube. The optical image is transferred by the fiber-optics directly to the photocathode. There the optical flux (photons) causes the release of photoelectrons in numbers proportional to the intensity of the incoming radiation. A certain number of the photoelectrons physically leave the bulk of the photocathode and reach the vacuum of the image section. The photon-photoelectron transfer takes place extremely fast; the estimated times are less

than 1×10^{-12} sec. Nonetheless losses occur in the process; they can be classified as photon and electron losses. A certain number of the incident photons can penetrate the photocathode without any effect, or are reflected by the surface of the photocathode. Another fraction of the total number of photons is absorbed in the bulk of the photocathode, but fail to release photoelectrons. On the other hand, photoelectrons created too far in the bulk of the photocathode recombine before they can reach the surface of the photocathode.

Because of these effects, the efficiency of the photon-photoelectron conversion process is considerably less than unity. This ratio, the number of released photoelectrons to the total number of incoming photons, is called the "quantum efficiency". This quantum efficiency is strongly dependent on the energy of the incoming photons (spectral range of the radiation), but for all practical purposes an average quantum efficiency can be defined and used for the visible part of the optical spectrum. For photocathodes employed in modern sensors (S20 and S25) this average quantum efficiency varies between 5% and 20%. This implies that a large number of photons is lost in the conversation process and that in an analysis of the statistical distribution of the photoelectron counts, these loss effects can not be neglected.

The only physically observable quantities connected with the photoelectric effect are the mean of the photon flux, the mean of the photoelectron flux, and the distribution of the photoelectron

counts during any given integration time. The statistical distribution of the photons cannot be observed directly.

The statistical distribution of the photons is transferred with modifications into the statistics of the photoelectron counts.

The dominant factor in determining the statistics of the electron counts is the ratio of the sensor integration time to the coherence time of the incident photons. A detailed discussion of these statistics can be found in References 1 and 2. Three different domains can be defined: 1) If the integration time (observation time) is large compared to the coherence time, the observed statistical distributions in the photoelectron count follow Poisson statistics. 2) If the observation time is approximately equal to the coherence time, the classical Bose - Einstein distribution will be observed. 3) If the observation time is less than the coherence time of the incoming photons, then a complex quantum-mechanical description is required. Electro-optical photon-counting sensors, such as the EBSICON, always have large integration times compared to the coherence time and therefore the resultant observed photoelectron distribution will be Poisson.

3.2 THE GAIN MECHANISM

In the image section, the photoelectrons are accelerated up to 10 KeV and hit the n-type silicon of the storage target. The high-

energy electrons penetrate several micrometers and come to rest. The interaction of the high-energy electrons with the lattice results mainly in the creation of electron-hole pairs in the crystal, which has a well-defined threshold of 3.5 eV. Beyond this threshold the electron hole-pair combinations cannot carry any significant amount of energy, therefore the energy dissipation of the high-energy photoelectrons occurs in a very orderly, highly controlled way: In a step-by-step procedure each creation of an electron-hole pair subtracts 3.5 eV from the energy of the photoelectrons, until the energy of the photoelectrons is exhausted. The number of electron-hole pairs per high-energy photoelectron is called the primary gain and is the ratio

$$G_p = \frac{E_p}{E_s} \quad (3.2.1)$$

where E_p is the energy of the high-energy photoelectrons and E_s the energy of the secondary electron-hole pairs. For $E_p = 10,000$ eV and $E_s = 3.5$ eV the primary gain becomes approximately 3000. Losses occur due to absorption effects. A thin aluminum layer is deposited on the illumination side of the target. This layer acts as a light shield and prevents photons which have passed through the photocathode from entering the target bulk material. High-energy photoelectrons penetrate this aluminum layer, but lose some of their energy. If the layer is thin enough and uniform, the only losses occur in the

energy of the photoelectrons; the number stays constant. When the electrons reach the silicon bulk material, their effective energy is that corresponding to the acceleration voltage in the image section but reduced by an energy loss, E_L . This has a significant effect on the primary gain, G_p , and equation (3.2.1) can now be rewritten

$$G_p = \frac{E_p - E_L}{E_s} \quad (3.2.2)$$

The other important loss effects in the target are mainly recombinations of charge carriers before they reach the depletion layer in the p-n junction. The total number of secondary charge carriers is reduced, and therefore also the total gain of the target. If one defines the effective gain G_e as the primary gain G_p reduced by the loss factor L

$$G_e = G_p (1-L) \quad (3.2.3)$$

one obtains from equation (3.2.2)

$$G_e = \frac{E_p - E_L}{E_s} (1-L) \quad (3.2.4)$$

The changes in the statistical distribution of the charge carriers due to the gain process and the associated loss mechanism are significant. The electron hole-pair creation in the silicon bulk

constitutes a highly deterministic process with insignificant statistical scatter of the number of electron-hole pairs for any given photoelectron energy. This in conjunction with uniformity of the acceleration field in the image section, which is required for good optical resolution, guarantees the uniformity of the photoelectron energies; therefore the statistical scatter in the total number of electron-hole pairs is also insignificant. The original fluctuations in the number of photoelectrons released by the photocathode are maintained; their random arrival corresponds to packets of G_e electron-hole pairs each. Superimposed on this distribution are the distributions of the loss mechanisms. The effects leading to the losses E_L (electron penetration of the aluminum light shield) are basically the same, which create electron-hole pairs in the silicon: Energy is dissipated in small and uniform quantities, again a highly deterministic process, which does not change the original distribution in any significant way. Finally, the charge carrier recombination effects are a random process which, for lossy targets, can result in significant signal loss. The recombination losses for EBSICON targets are small and the corresponding statistical process is essentially deterministic.

A detailed mathematical treatment of the noise problems associated with the gain mechanism is presented in Section 4.1.

3.3 PHYSICAL EFFECTS CONNECTED WITH CHARGE STORAGE

The main function of the storage target is the integration

of the charge created by the photoelectrons and to store this charge until it is read out by the read beam. The electron-hole pairs created by the photoelectrons in the n-type silicon become separated. The electrons move towards the n⁺ layer and play no further role in the process. The positive holes (p-charges) are extracted by the depletion layer of the p-n junction. The depletion layer has an intrinsic capacitance with very low conductivity, which enables this layer to maintain a potential differential over an extended period of time. The storage target represents basically a large array of individual capacitors each originally charged with a voltage equivalent to the target bias voltage V_B .

The positive charge carriers partially discharge this potential to a new potential V_L . The potential difference $V_B - V_L = V_C$ is a function of the depletion layer capacitance $C(V)$ and the number of charge carriers. If the total charge of all charge carriers collected on one diode is Q_D the potential difference becomes

$$V_C = V_B - V_L = \frac{Q_D}{C} \quad (3.3.1)$$

The spatial distribution of the optical signal is now transferred into voltage differences of a large, two-dimensional array of capacitors, where the largest potential difference V_C corresponds to no optical signal (black) and zero potential difference to maximum optical signal (white).

The width of the depletion layer is basically proportional to the square root of the external voltage and since the capacitance C of the depletion layer is inversely proportional to the width of the depletion layer, the change of capacitance C with voltage can be expressed by

$$C(V) = C_0 \sqrt{\frac{1}{1 + V/v}} \quad (3.3.2)$$

where C_0 is the capacitance without external voltage, V , the external voltage and v , the contact potential. For a single diode of a deep-etched target the values for C_0 are 2×10^{-14} F and 0.4 volt. For normal operation the changes in capacitance are not critical. For voltages large compared with the contact potential the change in capacitance is proportional to the square root of the voltages, i.e., over a range from 10 volt to 3 volt the capacitance increases only by 50%. Furthermore the most rapid changes in capacitance take place when the capacitors are practically discharged, that is at very high light levels ($V_C \approx v$). In this case the nonlinearities between the stored charge and the resulting voltages (equation 3.3.2) are usually masked by other effects. For these reasons it is valid to assume an average capacitance for the depletion layer and neglect its changes with voltage.

It is obvious that the capacitors can only be discharged to zero, where the depletion layer has its smallest width. In case of overload, i.e., the incoming optical signal had created much more positive charge carriers than are necessary for discharging the capacitor, the charge carriers are attracted by the next diodes surrounding the discharged one. The charge carriers discharge these diodes in turn, and this effect repeats itself until all charge carriers have either reached a diode or have recombined in the bulk of the n-layer. This effect is called "blooming" which is particularly noticeable in the case where very bright point images are observed. A point image which actually covers less than 10^{-5} of the active area may appear to cover a substantial amount, 10% to 50% or even all of the active area, if it is bright enough.

Since blooming is caused by charges traveling laterally from diode to diode, anti-blooming provisions can be incorporated, which makes it very probable that charges will be absorbed before they reach the next diode. This, however, must not interfere with the vertical travel of the charges, which would reduce the gain of the target. The most effective anti-blooming targets today are the deep-etched devices developed by Westinghouse and Texas Instruments. The diodes are separated by deep furrows which prevent the depletion layer from extending into the bulk of the n-type silicon below the furrows. A typical curve describing the blooming characteristics of this target is

shown in Figure III-1. For comparison, a curve with a slope of $1/2$ would indicate the apparent size of a point source, if no anti-blooming provisions were present in the target.

3.4 THE READOUT PROCESS

3.4.1 Equivalent Electrical Circuit

As mentioned in the preceding section, the charge carriers created by the photoelectrons in the bulk n-type silicon partially discharge the capacitors formed by the diode p-n function. In other words, the reverse bias on the individual diodes is reduced from the original value V_B to V_C (Figure III-2). The electrons in the read-beam "see" different potentials and by landing on the target restore the original reverse bias on each diode. The number of electrons needed to recharge the individual capacitors is equal to the number of carriers created by the photoelectrons; these recharging electrons constitute the output signal.

To analyze the readout process, it is necessary to draw an equivalent electrical circuit for the target read beam interaction (Figure III-2). The electrons leave the thermal cathode and are accelerated by the voltage V_T between the cathode and the read side of the target. V_T is the net acceleration voltage for the electrons as can be seen in Figure II-6. The target itself can be considered to consist of a capacitance and a diode in parallel as shown in Figure III-2. A positive bias voltage V_B (10 Volt) is applied

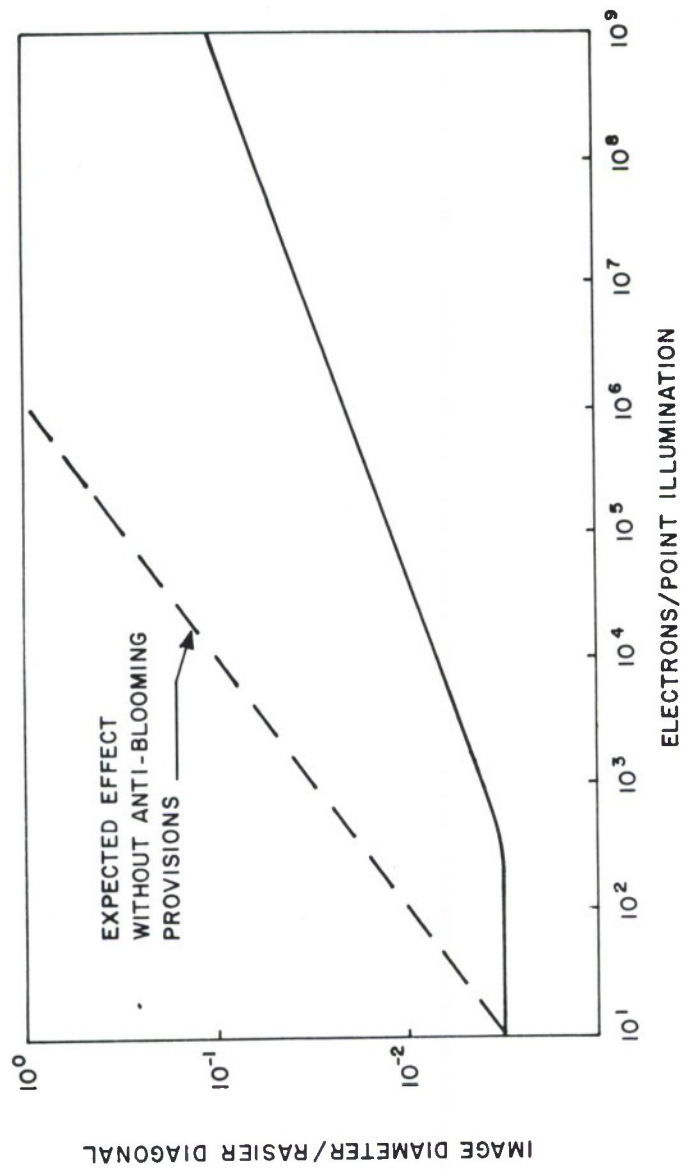


Figure III-1 TYPICAL BLOOMING CHARACTERISTICS OF EBSICON
(DATA FURNISHED BY S. CAMPANA, NAVAL AIR DEV. CENTR.)

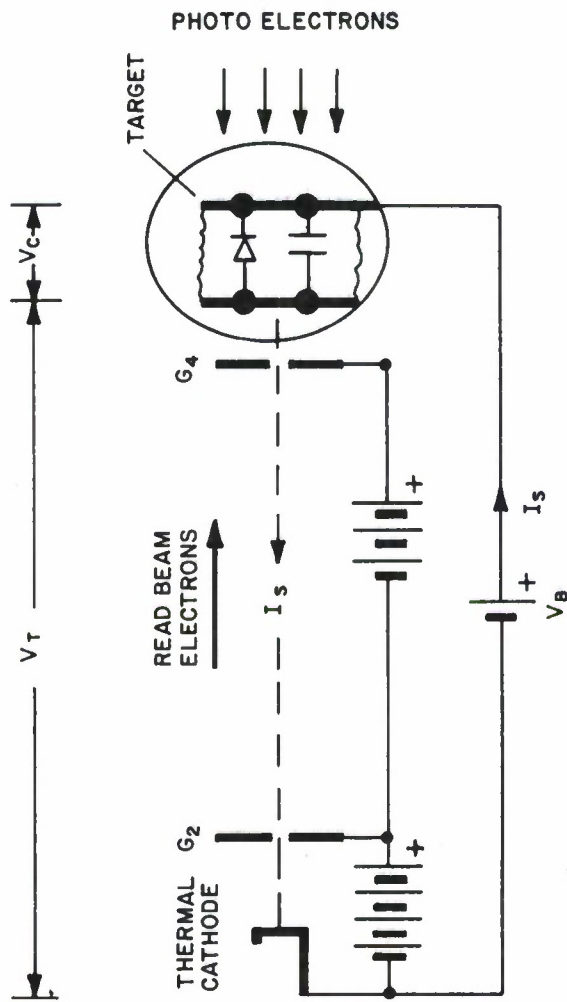


Figure III-2 EQUIVALENT CIRCUIT FOR READ PROCESS

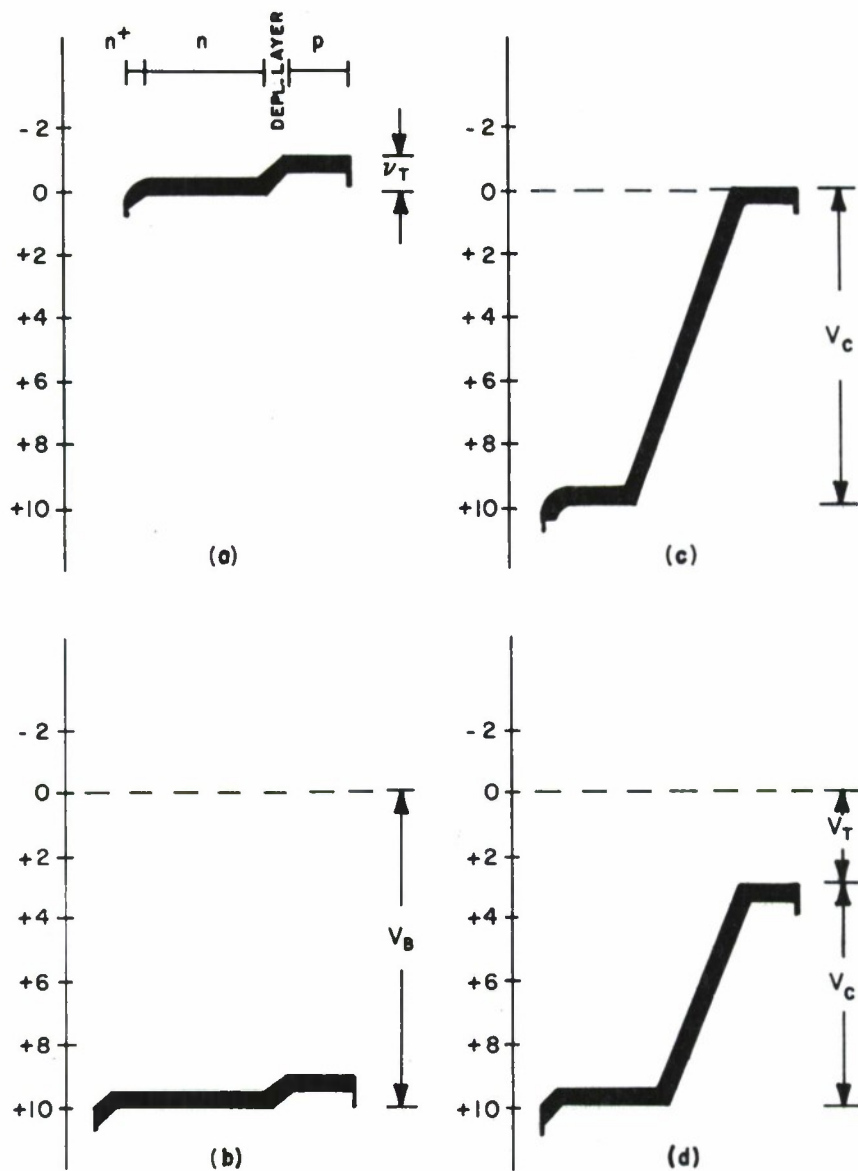
to the n-type silicon bulk (target connector). The potential distributions in the target as they change during read and exposure cycles are shown in Figure III-3.

The situation as it exists before any voltages are applied is shown in Figure III-3a. The target connector is at cathode potential, the p-n junction causes a small negative contact potential V_{CP} for the gold cap on top of the p-islands. ($V_{CP} \approx 0.3$ Volts, the contact potential on the n^+ junction is also approximately 0.3 V.) Figure III-3b shows the potential distribution, when the target is connected to the positive bias voltage, V_B , but before the first scan reaches the diode. During the first scan the p-islands are placed at cathode potential, the voltage differential across the capacitor V_C becomes now

$$V_C = V_B \quad (3.4.1)$$

This voltage differential across the capacitor occurs mainly in the depletion layer of the p-n junction, while the rest of the n and p sections have basically zero potential gradients. The depletion layer increases in width, depending on the resultant voltage V_C (Figure III-3c.

During illumination of the target, electron-hole pairs are created. The electrons travel towards the n^+ layer while the positive holes pass through the diode, discharging the capacitor and thereby reducing the voltage V_C . The resulting potentials are shown



1A-46,366

Figure III-3 DISTRIBUTION OF POTENTIALS ACROSS STORAGE TARGET (ONLY UPPER LIMITS OF CONDUCTION BAND ARE SHOWN, CONTACT POTENTIALS BETWEEN METAL CONTACTS AND SILICON BULK MATERIAL ARE NEGLECTED)

in Figure III-3d. At the next scan the read beam electrons flow through the target into the signal connectors until the voltage V_T has become zero again (Figure III-3c).

3.4.2 The Current Voltage Characteristics

The target read beam interaction is quantitatively determined by the so-called current-voltage characteristic (I-V curve). This curve gives the instantaneous signal current I_S as a function of the target voltage V_T for a single diode. This I-V curve and its particular shape defines in principle the total tube performance, the signal generation in the tube, and the tube limitations. This I-V curve can be determined by experiment for each tube under operating conditions.

The potential V_T cannot be measured directly because V_T is the potential difference between the floating electrode of the storage target and the thermal cathode, and is therefore inaccessible for any experiment. Indirectly, however, V_T can be obtained by saturating the storage target, i.e., by discharging the capacitors in the p-n junction. In this case the potential V_C across the capacitor is reduced to the known, constant contact potentials in the target. The voltage V_T now becomes

$$V_T = V_B - v_T \quad (3.4.2)$$

This important I_V curve can now be determined experimentally by using different bias voltages V_B , correcting for v_T and measuring

the corresponding signal current I_S .^{*} A typical I-V curve for a silicon diode target is shown in Figure III-4.^{**} This curve has all the characteristics of a vacuum diode operating with a space charge limited regime. Examination of Figure III-4 shows three distinct areas: the region of exponential increase of the signal current I_S at small negative potentials V_T ; the space-charge limited region, where the signal current increases basically with $V_T^{3/2}$, and finally a saturation region where the signal current reaches the value of the saturation current and becomes independent of V_T .

The generally assumed fact, that the target simply acts as an analyzer of the energy distribution of the electrons in the read beam, cannot be supported by the experimental evidence. A detailed analysis of the effects determining the shape of the I-V curve will be the subject of a separate document to be published in the near future.

3.4.3 Approximation of the I-V Characteristic

For a mathematical model the experimentally obtained I-V curve can be approximated very closely by the mathematical form

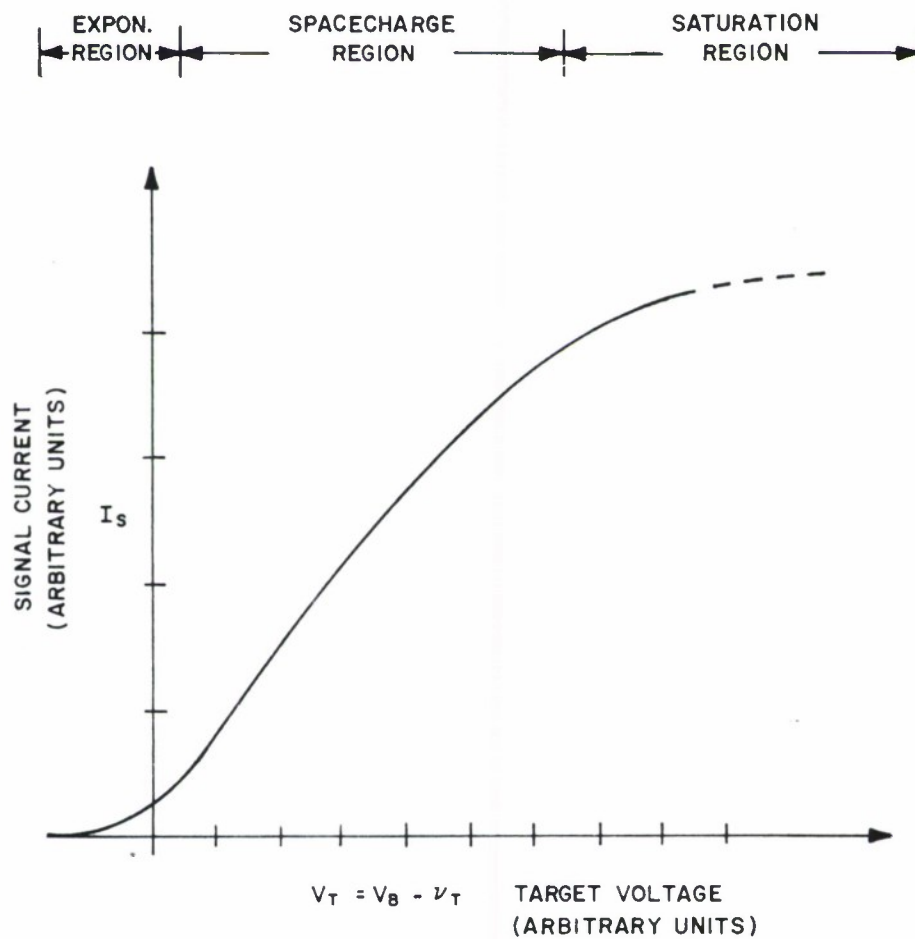
$$I_S = I_{SAT} (1 - e^{-b V_T}) \quad (3.4.3)$$

where b is a constant.

This curve gives a good representation of the linear range

^{*}Suggested by Dr. A. S. Lapovsky of Westinghouse.

^{**}Plotted from data furnished by R. E. Franseen, Army NVL.



IA-46,372

Figure III-4 TYPICAL I-V CHARACTERISTIC OF EBSICON TARGET

and the transition into the saturation region. Figure III-5 shows both curves, normalized for equal saturation current. Except for the region around the origin, both curves have very similar shape. For this reason a mathematical model should give very accurate results, except for very low lag values, which will occur only after many reads or for very slow scans. But these effects are considered of second order for which the mathematical model was not designed, since it is not intended to operate the sensor tubes in slow scan or with many read scans in a real system application.

3.4.4 The Signal Current

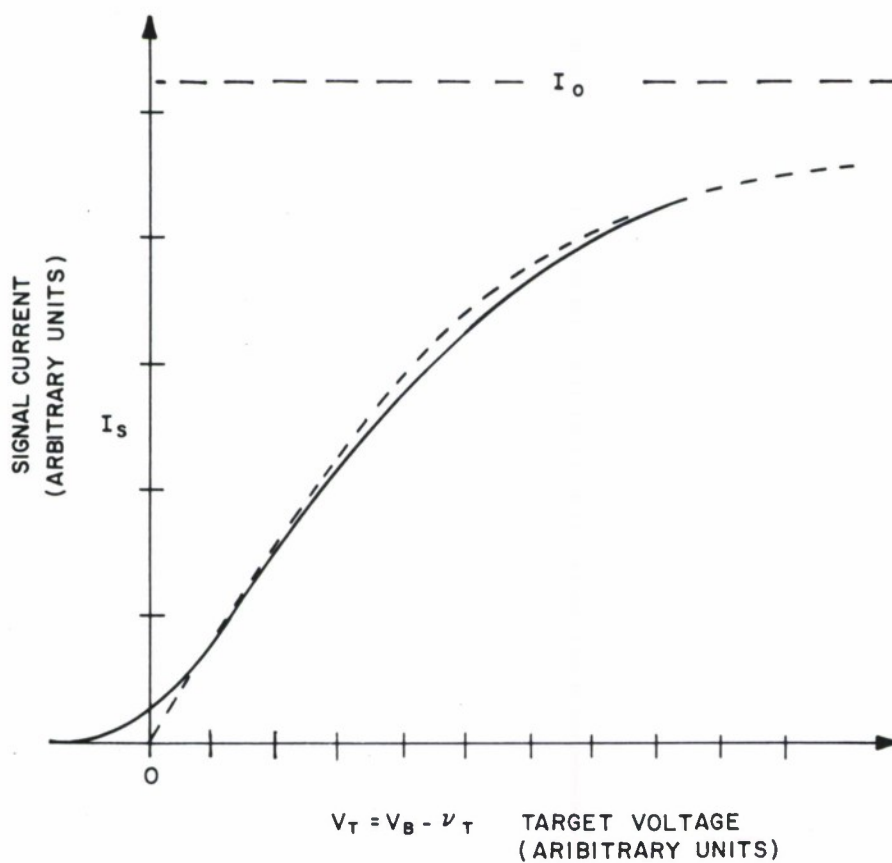
As observed from a fixed point on the target, the passing of the read-beam appears to be equivalent to the arrival of a time-varying current. If the beam scan velocity is constant, the time dependence of the current follows a curve similar to the characteristic which describes the spatial current distribution in the read-beam. If this distribution is given by a function $g(t)$ and the saturation current I_{SAT} is replaced by the total read beam current I_B , Equation (3.4.3) can be rewritten

$$I_S(t) = I_B \cdot g(t) (1 - e^{-bV_T}) \quad (3.4.4)$$

Since V_T is determined by the charge Q stored on the target and the current $I_S(t)$ is defined by

$$I_S(t) = \frac{dQ}{dt} \quad (3.4.5)$$

a differential equation for the signal current $I_S(t)$ can be derived.



IA-46,371

Figure III-5 APPROXIMATION OF EXPERIMENTALLY OBTAINED
I-V CHARACTERISTIC BY FUNCTION $I_s = I_0 (1 - e^{-bV_T})$

The detailed derivation and solution of this differential equation for a two-dimensional charge field and a two-dimensional read beam moving with constant read velocity, v , are presented in Section 4.1 of this report.

The solution for the time dependence of the signal current for a given charge field is involved and requires the use of computers.

3.4.5 The Lag

The charge stored on the target is not read out fully during one scan process; this can have two reasons, both of which limit the signal current.

a) Read beam limitation. In this case the scan beam cannot furnish enough electrons during its "dwell time" to recharge the target and a certain percentage of the original signal remains on the target. If there is true beam limitation the signal current remains constant, independent of the original illumination; the remaining charge is merely the difference between the charge created by the illumination and the total charge delivered by the full read beam during the "dwell time".

b) Lag. As the I-V curve shows, the signal currents vanish for small voltages V_T . As soon as the target potential V_T reaches cathode potential, less and less electrons are available due to the space-charge effects and cannot land on the target. This effect can

be considered a type of read-beam limitation, but here the available charge is integrated not over the whole read beam delivered during the "dwell time", but only over the number of electrons in the read beam having an energy higher than a certain cutoff energy.

Both read-beam limitation and lag are strongly dependent on the scan velocity, since this is the parameter which defines the "dwell time". Their dependence on the original illumination level, however, shows a different behavior: In case of read-beam limitation a constant amount of charge Q_{SAT} is replenished during a scan, independent of signal level, while in the case of lag a constant amount of charge Q_E is left on the storage target during each scan, independent of signal level. Since lag values are usually given as a fraction ϵ of the actually read charge to the amount of charge stored on the target Q_o , one obtains for read-beam limitation:

$$\epsilon_R = \frac{Q_o - Q_{SAT}}{Q_o} \quad (3.4.6)$$

and for lag

$$\epsilon_L = \frac{Q_E}{Q_o} \quad (3.4.7)$$

SECTION IV

THE MATHEMATICAL TUBE MODEL

The objective of this section is to establish a representative model, and to do so the qualitative results of Section 3.4 must be carried to their mathematical conclusions in the form of equations yielding quantitative values of readout current and instantaneous charge. Since these equations are functions of initial target charge, the specific probability density functions of the processes described in Sections 3.1 through 3.3 which describe the charging of the target must be derived and justified. This is accomplished in Section 4.1 below.

In Section 4.2 these results are brought together in the forms of a computer simulation of the tube operation and as programs used to evaluate the statistical performance of the tube.

4.1 DESCRIPTION AND DERIVATION OF EQUATIONS

4.1.1 The Readout Process

In Section 3.4, the relationship between diode current and voltage and hence also for the distribution of target current density, J_t , beam current density, J_b , and target voltage was shown to be closely approximated by:

$$J_t = (1 - e^{-bV_t})J_b \quad (4.1.1)$$

With knowledge of target capacitance (farads/cm²), (4.1.1) can be rewritten in terms of target charge density, q_t , as

$$J_t = (1 - e^{-\beta q_t}) J_b , \quad (4.1.2)$$

where,

$$\beta = \frac{b}{c} \quad (4.1.3)$$

The readout beam is assumed to be a moving axially-symmetric Gaussian-shaped current distribution with a total current equal to I_0 as follows:

$$J_b(x, y, t) = \frac{I_0}{\pi \alpha^2} e^{-\frac{[x-x_0(t)]^2 + [y-y_0(t)]^2}{\alpha^2}} \quad (4.1.4)$$

where (x, y) is a specific point on the target and $[x_0(t), y_0(t)]$ is the present location of the center of the beam. The forms of $x_0(t)$ and $y_0(t)$ are such as to achieve the raster scan-pattern described in Section 2.3.

The distribution of the target-charging current density is then,

$$\frac{dq_t}{dt} = - J_t \quad (4.1.5)$$

Therefore,

$$\frac{dq_t(x,y,t)}{dt} = - \left[1 - e^{-\beta q_t(x,y,t)} \right] J_b(x,y,t) \quad (4.1.6)$$

suppressing the notation x and y and rearranging terms, (4.6.5)

becomes

$$\int_{q_t(0)}^{q_t(t)} \frac{dx}{1 - e^{-\beta x}} = - \int_0^t J_b(\tau) d\tau \triangleq \Delta q(x,y,t) \quad (4.1.7)$$

The negative of the integral of the beam-current distribution, Δq , will be retained inexplicitly, for now, because it will take on different forms depending upon how it is used in final implementations.

Equation (4.1.7) can be integrated to solve for charge density and then for the target current distribution yielding the following:

$$q_t(t) = \frac{1}{\beta} \ln \left\{ e^{\beta \Delta q(t)} \left[e^{\beta q_t(0)} - 1 \right] + 1 \right\} \quad (4.1.8)$$

Then,

$$J_t(t) = - \frac{dq_t(t)}{dt} \quad (4.1.9)$$

$$= \frac{e^{\beta \Delta q(t)} \left[e^{\beta q_t(0)} - 1 \right] J_b(t)}{e^{\beta \Delta q(t)} \left[e^{\beta q_t(0)} - 1 \right] + 1}$$

Here, $J_b(t)$ also is not explicitly given since its specific form depends upon the implementation of these results.

Equations (4.1.8) and (4.1.9) are general closed-form results for any target with the J-q characteristics of (4.1.2). However, for the diode-array target of an EBSICON tube these equations must be integrated over the area of a diode so that the individual current contributions from each diode to the total target current can be determined.

Since each diode has a gold cap, as illustrated in Section 1.3, the charge and its derivative are constant over the area of each diode. It will be assumed that the read beam is also constant over a diode since its area is small compared to the read beam area. Hence, for each diode, (4.1.8) and (4.1.9) become

$$Q(x_i, y_j, t) = \frac{1}{\beta} \ln \left\{ e^{\beta \Delta Q(x_i, y_j, t)} \left[e^{\beta Q(x_i, y_j, 0)} - 1 \right] + 1 \right\} \quad (4.1.10)$$

and

$$I_t(x_i, y_j, t) = \frac{e^{\beta \Delta Q(x_i, y_j, t)} [e^{\beta Q(x_i, y_j, 0)} - 1] I_b(x_i, y_j, t)}{e^{\beta \Delta Q(x_i, y_j, t)} [e^{\beta Q(x_i, y_j, 0)} - 1] + 1} \quad (4.1.11)$$

where

$$\Delta Q(t) = \Delta q(t) \Delta A \quad (4.1.12)$$

$$I_t(t) = J_t(t) \Delta A \quad (4.1.13)$$

$$Q(t) = q_t(t) \Delta A \quad (4.1.14)$$

and

$$Q(0) = q_t(0) \Delta A \quad (4.1.15)$$

in all of which ΔA is the area of a diode and in calculating β in (4.1.3) c must also be multiplied by ΔA . The read-beam current is now

$$I_b(x_i, y_j, t) = \frac{I_0 \Delta A}{\pi \alpha^2} e^{-\frac{[x_i - x_0(t)]^2 + [y_j - y_0(t)]^2}{\alpha^2}} \quad (4.1.16)$$

where (x_i, y_j) is the center of the i, j^{th} diode. $I_t(x_i, y_j, t)$ is the independent contribution to the total target current by the i, j^{th} diode and therefore they must be summed over all i and j to determine the target current at time t .

Equations (4.1.10) and 4.1.11) provide a deterministic functional relationship for charge and current contribution for each diode in terms of the initial charge, $Q(x_i, y_j, 0)$.

4.1.2 Statistics of Photoelectrons Emitted by the Photocathode

If statistical analyses are to be performed, the probability density function (PDF) of the initial charge must be known. Therefore, in this and the following two subsections, the processes described in Sections 3.1 thru 3.3 must be analyzed to derive and verify the specific PDF's of those processes leading to the final PDF required; namely that of $Q(x_i, y_j, 0)$.

It is shown in [1, P. 496] that for the case where the observation time, T , is large compared to the coherence time, τ , the probability of the number, N , of photoelectrons emitted to each diode in the time interval T is:

$$\text{Prob } \{N=n\} = \frac{1}{n!} \left(\frac{\bar{N}}{\beta} \right)^n S_n \left(\frac{\beta T}{\tau} \right) e^{-\left[\frac{T}{\tau} (\beta - 1) \right]}$$

where

$$\beta = (1 + 2\bar{N} \frac{\tau}{T})^{1/2} \quad (4.1.17)$$

and

$$S_0(\frac{\beta T}{\tau}) = S_1(\frac{\beta T}{\tau}) = 1 \quad (4.1.18)$$

but for n greater than one, from [2] and [4, P. 467],

$$S_n(\frac{\beta T}{\tau}) = 1 + \sum_{k=1}^{n-1} \frac{(n-1+k)!}{k!(n-1-k)! 2^k} (\frac{\tau}{\beta T})^k \quad (4.1.19)$$

In the case of the EBSICON (Section 3.1), the observation time, T (integration time) is much longer than the coherence time, τ , of the light illuminating the photocathode ($\tau/T \approx 1.5 \times 10^{-13}$).

In this case, β approaches unity so that

$$\text{Prob. } \{N=n\} = \frac{\bar{N}^n}{n!} S_n(\frac{T}{\tau}) e^{-[\frac{(\beta-1)}{\tau/T}]} \quad (4.1.20)$$

However, the exponent approaches the indeterminate form $0/0$. But,

using L'Hospital's rule, it is easily shown that this form is resolved and the limit becomes $-\bar{N}$. Also except for values of n in the order of 10^6 , corresponding to extremely great illumination (ordinarily n ranges from 50 to 10^3), it is seen from (4.1.19) that $S_n(T/\tau)$ is very nearly unity. Therefore, (4.1.20) approaches the Poisson probability,

$$\text{Prob. } \{N=n\} = \frac{\bar{N}^n}{n!} e^{-\bar{N}} \quad (4.1.21)$$

4.1.3 Gain and Loss Mechanisms

As described in Section 3.2, gain is achieved in the tube by virtue of accelerating the photoelectrons emitted from the photocathode in the image section, whereupon they bombard the target and create hole-electron pairs in the n-type silicon layer. The number of hole-electron pairs created by each photoelectron determines the gain.

Since all photoelectrons arrive with essentially the same energy, and since in giving up energy, while being absorbed, it is given up in equal discrete amounts (each amount corresponding to the energy required to create a hole-electron pair, 3.4eV), the gain process is deterministic for all practical purposes for a constant rate of arrival of photoelectrons. Further since the cross section of the target is high, the holes created proceed under a slight

field gradient toward the p-islands very evenly spaced in time while the electrons remain in the n-region.

Random loss occurs through recombination of some of the hole-electron pairs in the n-silicon layer. If a given interval in time is considered as the holes travel in an evenly-spaced stream, each hole is either recombined or not with some probability, p . Therefore, the number of holes remaining in a given interval of time as they arrive at a p-island is governed by a Bernoulli distribution. This is because the success or failure of the arrival of each hole in the interval was determined by an independent Bernoulli trial.

It is stated in Section 3.2, however, that these losses are low. This statement is equivalent to the statement that the probability, p , is approximately zero and that the standard deviation of the Bernoulli distribution is

$$\sigma = \sqrt{np(1-p)} \approx 0 \quad (4.1.21)$$

thus yielding a process which is essentially deterministic.

The above discussion was based upon a constant rate of arrival of photoelectrons when, in fact, the rate of arrival was shown in Section 4.1.2 to be Poisson distributed. Therefore, in the case of the EBSICON tube the Poisson statistics of photoelectron count are passed over to stored charge by the tube gain factor, G .

The resultant distribution, which can be called a "modified" Poisson distribution [3, P. 33] is obtained by multiplying a Poisson distributed random variable, x , by a constant, G , to yield a new random variable, y .

$$y = Gx \quad (4.1.22)$$

If the mean of the distribution of x is λ , its PDF is given by:

$$f_x(x) = \sum_{k=0}^{\infty} \frac{e^{-\lambda} \lambda^k}{k!} \delta(x-k) \quad (4.1.23)$$

and the PDF of y is

$$f_y(y) = \sum_{k=0}^{\infty} \frac{e^{-\lambda} \lambda^k}{k!} \delta(y-Gk) \quad (4.1.24)$$

with

$$\mu_y = G\lambda \quad (4.1.25)$$

and

$$\sigma_y^2 = G^2 \lambda \quad (4.1.26)$$

4.1.4 Target Saturation

As described in Section 3.3, there is local diode saturation with high illumination which in turn leads to blooming. If the random variable, y , in (4.1.24) is the available or total possible charge per diode with no saturation effects, then the statistics of the actual charge, Q_t , are changed from those of y by saturation.

The functional relationship chosen between y and Q_t to describe local saturation is

$$Q_t = \frac{1}{\gamma} (1 - e^{-\gamma y}) \quad (4.1.27)$$

This function was chosen for four reasons. The first two are the facts that in the linear region where saturation is not significant, i.e., where

$$e^{-x} \approx 1 - x \quad (4.1.28)$$

the mean and variance of Q_t can be shown to approach the mean and variance of y , given in (4.1.25) and (4.1.26) respectively.

The other two reasons are that when saturation occurs (i.e., when $\lambda \rightarrow \infty$) the mean of Q_t approaches a constant, $1/\gamma$, and the variance of Q_t approaches zero. These two effects are the most significant features of local saturation and are clearly seen in the following expressions (4.1.29) and (4.1.30) for the mean and variance of Q_t respectively.

$$\mu_{Q_t} = \frac{1}{\gamma} [1 - e^{-\lambda(1 - e^{-\gamma G})}] \quad (4.1.29)$$

$$\sigma_{Q_t}^2 = \frac{1}{\gamma^2} \left\{ e^{-\lambda[1-(e^{-\gamma G})^2]} - e^{-2\lambda(1-e^{-\gamma G})} \right\} \quad (4.1.30)$$

The transformation of (4.1.27) yields the following probability function (PDF) for Q_t

$$f_{Q_t}(Q_t) = \sum_{k=0}^{\infty} \frac{e^{-\lambda} \lambda^k}{k!} \delta\left[Q_t - \frac{1}{\gamma} (1-e^{-\gamma Gk})\right] \quad (4.1.31)$$

This PDF for the initial diode charge is, therefore, the one to be used in computer implementations which evaluate the statistical performance of the tube. Blooming is accommodated in the implementations by the proper initialization of the charge of the diode array, as will become evident in Section 4.2.

4.2 IMPLEMENTATION IN TERMS OF COMPUTER PROGRAMS

Equations (4.1.10), (4.1.11) and (4.1.31) are the fundamental building blocks in implementing the mathematical model as derived in the preceding section. They can be used in two ways. One way is to simulate the video signal or the sampled video output of the tube. The other way is to determine the ensemble variance and mean at any point on the "current map" of the output and the correlation between two separated points on the current map. From these results P_D and P_{FA} can be determined for various system conditions for a given threshold. Computer programs were written to accomplish both implementations.

4.2.1 Simulation Program

In the simulation program the mean number of photoelectrons arriving from the photocathode during the integration time, λ_{ij} , is determined for each i,j^{th} diode. This number is dependent upon the optics assumed for the system, the background level assumed and the strength of the image, if any, illuminating the i,j^{th} diode. The Poisson parameter is used in the following equation to approximate a Poisson random variable with a Gaussian envelope, but taking on integer values:

$$n_{ij} = \text{Integer} \left[\sqrt{-2\lambda_{ij} \ln u_1} \cos(2\pi u_2) + \lambda_{ij} + .5 \right] \quad (4.2.1)$$

where u_1 and u_2 are two independent pseudo-random variables which are uniformly distributed over the interval ranging from zero to one. The samples of u_1 and u_2 are generated by means of a power residue method for each diode.

From (4.1.27) the charge for each diode is computed by

$$Q_{ij} = \frac{1}{\gamma} (1 - e^{-G\gamma n_{ij}}) \quad (4.2.2)$$

where $\frac{1}{\gamma}$ is the maximum or saturation value for target charge per diode and G is the tube gain, multiplied by the electronic charge.

In this application, $\Delta Q(x_i, y_i, t)$ of (4.1.12) is appropriately

$$\Delta Q(x_i, y_j, t) = \frac{I_0 \Delta A e^{-\left(\frac{y_j + nL}{\alpha}\right)^2}}{2 v \alpha \sqrt{\pi}} \left[\operatorname{erf}\left(\frac{x_i - x_0 - vt}{\alpha}\right) - \operatorname{erf}\left(\frac{x_i - x_0}{\alpha}\right) \right] \quad (4.2.3)$$

where L is the distance between scan lines and n is the line number of the present scan. The scanning beam is as defined from (4.1.16) by letting $x_0(t) = -x_0 - vt$ where v is the scan velocity and by letting $y_0(t) = y_0$. From (4.1.8), $Q(x_i, y_j, t)$ can be calculated for any time, t , along the present scan line for each diode.

$$Q(x_i, y_j, t) = \frac{1}{\beta} \ln \left\{ e^{\beta \Delta Q(x_i, y_j, t)} \left[e^{\beta Q(x_i, y_j, 0)} - 1 \right] + 1 \right\} \quad (4.2.4)$$

For the first scan line $Q(x_i, y_j, 0)$ is given by (4.2.2) and for each scan line, t varies from zero to $-2x_0/v$ where x_0 is a large negative distance relative to the diode array size.

In the particular simulation an array of 21×21 diodes was used with a spacing between diode centers of $12.5 \mu\text{m}$ or $.00125$ cm.

The origin of the coordinate system of x_i, y_j of the array was taken to be the center diode (i.e., x_{11}, y_{11}). Therefore, x and y ranged from $-.0125$

to +.0125 cm and x_0 was set at -.025 cm.

After calculating the new charge for each t on the first scan line, the individual diode current contribution is calculated as

$$I_t(x_i, y_j, t) = \left[1 - e^{-\beta Q(x_i, y_j, t)} \right] I_b(x_i, y_j, t) \quad (4.2.5)$$

Then for each t the total target current is calculated as

$$I(t) = \sum_{i=1}^{21} \sum_{j=1}^{21} I_t(x_i, y_j, t) \quad (4.2.6)$$

At the end of each scan (i.e., when $t = -2x_0/v$), the old $Q(x_i, y_j, 0)$ is updated as

$$Q(x_i, y_j, 0) = Q(x_i, y_j, -\frac{2x_0}{v}) \quad (4.2.7)$$

This value is then used in (4.2.4) to calculate the charge, current and final charge for the next scan. The above procedure is repeated until the last scan is completed.

If the "increments in time" are made fine enough, a three-dimensional plot of the simulated video output such as shown in Figure IV-1 can be made. Note that the time axis (horizontal axis)

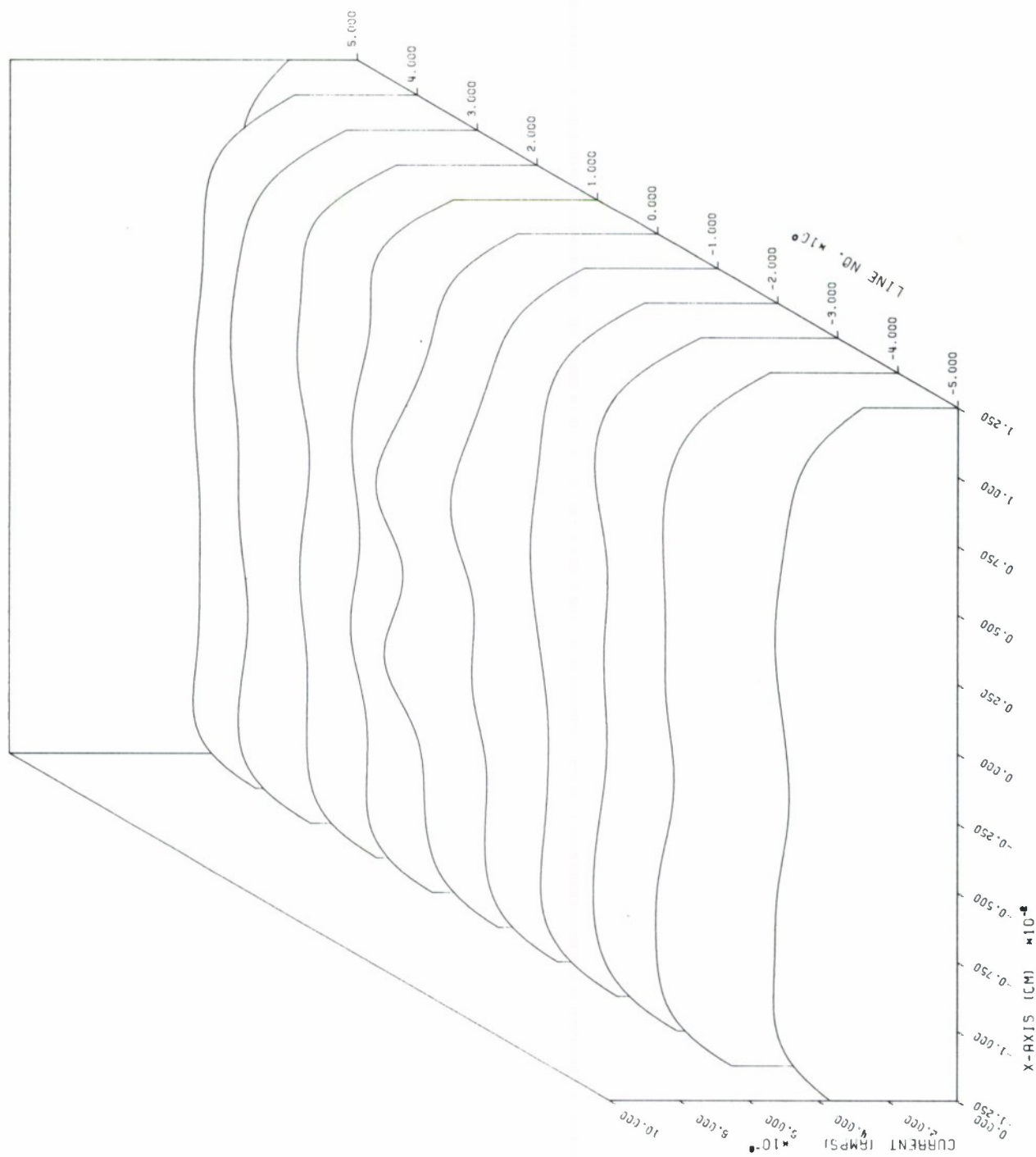


Figure IV-1 SIMULATED VIDEO OUTPUT

is labeled in centimeters and hence the use of the term "current map". Shown in Figure IV-1 is the current map for background with two point images separated by four diodes. On the other hand, one may want to make the time increments correspond to sampling intervals to be used for video sampling. Then the simulation could be used to print out just the values of the sampling points.

4.2.2 Statistical Evaluation Programs

The main idea behind the programs which calculate the ensemble statistical parameters is to first integrate the read beam to a point (in the specific case, to the center) in the current map and to write the equation for the beam current evaluated at that point also. A 13 x 13 diode array was chosen in this case to ensure that edge effects would not be a factor in computing the output. In this case, ΔQ and I_b would be calculated as follows:

(4.2.3)

$$\Delta Q(x_i, y_j) = \frac{I_0 \Delta A}{2v\alpha\sqrt{\pi}} \left[\operatorname{erf}\left(\frac{x_i + x_0}{\alpha}\right) - \operatorname{erf}\left(\frac{x_i - x_0}{\alpha}\right) \sum_{n=1}^5 e^{-\left(\frac{y_j + nL}{\alpha}\right)^2} \right. \\ \left. + \frac{I_0 \Delta A}{2v\alpha\sqrt{\pi}} e^{-\left(\frac{y_j}{\alpha}\right)^2} \left[\operatorname{erf}\left(\frac{x_i}{\alpha}\right) - \operatorname{erf}\left(\frac{x_i - x_0}{\alpha}\right) \right] \right]$$

$$I_b(x_i, y_j) = \frac{I_0 \Delta A}{\pi \alpha^2} e^{-\frac{x_i^2 + y_j^2}{\alpha^2}} \quad (4.2.9)$$

The next thing to recognize from (4.1.11) is that the target current contribution from each diode is a function of its initial charge written in a closedform expression:

$$I_t[x_i, y_j, Q(x_i, y_j, 0)] \quad (4.2.10)$$

$$= \frac{e^{\beta \Delta Q(x_i, y_j)} \left[e^{\beta Q(x_i, y_j, 0)} - 1 \right] I_b(x_i, y_j)}{e^{\beta \Delta Q(x_i, y_j)} \left[e^{\beta Q(x_i, y_j, 0)} - 1 \right] + 1}$$

Then with the probability density function (PDF) given in (4.1.31) for each diode,

$$f_{Q_t}(Q_{ij}) = \sum_{k=0}^{\infty} \frac{e^{-\lambda_{ij}} (\lambda_{ij})^k}{k!} \delta \left[Q_{ij} - \frac{1}{\gamma} (1 - e^{-k\gamma G_{ij}}) \right] \quad (4.2.11)$$

the mean, $\mu_{I_t}(x_i, y_i)$, and the mean square, $m_{I_t}(x_i, y_i)$, of the current contribution for each diode can be closely approximated as

$$\mu_{I_t}(x_i, y_j) = \sum_{k=0}^{k_f} \frac{e^{-\lambda_{ij}} (\lambda_{ij})^k}{k!} I_t \left[x_i, y_j, \frac{1}{\gamma} (1 - e^{-k\gamma G_{ij}}) \right] \quad (4.2.12)$$

$$m_{I_t}(x_i, y_j) = \sum_{k=0}^{k_f} \frac{e^{-\lambda_{ij}} (\lambda_{ij})^k}{k!} I_t^2 \left[x_i, y_j, \frac{1}{\gamma} (1 - e^{-k\gamma G_{ij}}) \right] \quad (4.2.13)$$

Since the weights in the summations are the Poisson weights of the original Poisson density of the number of photoelectrons, k_f was chosen to be equal to an integer rounded to the mean plus three times the standard deviation of that density,

$$k_f = \text{Integer} \left[\lambda_{ij} + 3 \sqrt{\lambda_{ij}} + .5 \right] \quad (4.2.14)$$

From (4.2.12) and (4.2.13) the variance for each diode current can be calculated,

$$\sigma_{I_t}^2(x_i, y_j) = m_{I_t}(x_i, y_j) - \mu_{I_t}^2(x_i, y_j) \quad (4.2.15)$$

Each contribution is statistically independent of all the others and hence the mean and the variance of the total target current can be obtained by summing the means and variances of all the contributions,

$$\mu_I = \sum_{i=1}^{13} \sum_{j=1}^{13} \mu_{I_t}(x_i, y_j) \quad (4.2.16)$$

and

$$\sigma_I^2 = \sum_{i=1}^{13} \sum_{j=1}^{13} \sigma_{I_t}^2 (x_i, y_j) \quad (4.2.17)$$

To calculate the output after the next write-read cycle the mean and variance of the charge remaining on each diode after a complete read-out must be computed. Since the charge from the next illumination is independent of the remaining charge, the two means and variances are summed. Then from the new variance and mean, the corresponding λ_{ij} and G_{ij} must be calculated for use in (4.2.11). The integrated beam current $\Delta Q(x_i, y_j)$ must correspond to the final time after a complete read-out.

$$\Delta Q(x_i, y_j) = \frac{I_0 \Delta A}{2v \alpha \sqrt{\pi}} \left[\operatorname{erf} \left(\frac{x_i + x_0}{\alpha} \right) - \operatorname{erf} \left(\frac{x_i - x_0}{\alpha} \right) \right] \sum_{n=-5}^5 e^{-\left(\frac{y_j - nL}{\alpha} \right)^2} \quad (4.2.18)$$

and again recognizing from (4.1.10) that the final charge is a function of the initial charge

$$Q_f [x_i, y_j, Q(x_i, y_j, 0)] \quad (4.2.19)$$

$$= \frac{1}{\beta} \ln \left\{ e^{\beta \Delta Q(x_i, y_j)} \left[e^{\beta Q(x_i, y_j, 0)} - 1 \right] + 1 \right\}$$

the mean, mean square and hence the variance can be found in the same manner as these parameters were found for each diode current (4.2.12), (4.2.13) and (4.2.15).

For the new illumination, the mean charge and the variance can be found from (4.1.29) and (4.1.30), respectively,

$$\mu_Q(x_i, y_j) = \frac{1}{\gamma} \left[1 - e^{-\lambda_{ij}} (1 - e^{-\gamma G}) \right] \quad (4.2.20)$$

and

$$\sigma_Q^2(x_i, y_j) = \frac{1}{\gamma^2} \left[e^{-\lambda_{ij}} (1 - e^{-\gamma G})^2 - 2\lambda_{ij} (1 - e^{-\gamma G}) \right] \quad (4.2.21)$$

To (4.2.20) is added the mean of the remaining charge on the i, j^{th} diode and to (4.2.21) the variance of the remaining charge is added. Let the resultant mean and variance be designated by $\mu_Q(x_i, y_j)$ and $\sigma_Q^2(x_i, y_j)$. Then by inverting (4.2.20) and (4.2.21) simultaneously the appropriate λ_{ij} and G_{ij} to be used in (4.2.11) can be calculated by

$$\lambda_{ij} = \frac{\left[\ln[1 - \gamma \mu_Q(x_i, y_j)] \right]^2}{\ln \left\{ \frac{1 - \gamma \mu_Q(x_i, y_j)}{\gamma^2 \sigma_Q^2(x_i, y_j) + [1 - \gamma \mu_Q(x_i, y_j)]^2} \right\}} \quad 4.2.22$$

and

$$G_{ij} = -\frac{1}{\gamma} \ln \left[\frac{\ln \left\{ \gamma^2 \sigma_Q^2 (x_i, y_j) + [1 - \gamma \mu_Q (x_i, y_j)]^2 \right\}}{\ln [1 - \gamma \mu_Q (x_i, y_j)]} - 1 \right] \quad (4.2.23)$$

The above steps, equations (4.2.8) through (4.2.23), are repeated for each subsequent read-out and illumination cycle.

Also included in the programs is the ability to calculate, in a similar manner, the means at two different points in the current map and the expectation of the product of the currents at two different points. Of course, ΔQ , I_b and hence I_t will be different at each point but obtaining the forms is straightforward and will not be explained here. However, it must be stated that in order to use the PDF of (4.2.11) and procedures such as those of (4.2.12) and (4.2.13) the illumination must be stationary background noise for each cycle. That is to say, λ_{ij} must be the same for the charge at the two points. This is not the case when only one point is used. In fact, when one point is analyzed, the procedure allows a scene to be illuminated and for the scene to change from cycle to cycle, since λ_{ij} can be chosen by the user to be different for each i and each j .

Finally, from a separate analysis, the PDF for an individual diode current contribution was determined and it was found to closely match a Gaussian PDF. Therefore, the PDF of the sum of all $I_t(x_i, y_j)$ will be even more Gaussian. Hence, by knowing σ_I and μ_I , the PDF of the target current is known. By analyzing one point first without an image present but with only background noise and then with an image in the presence of background, the two PDF's can be superimposed, thereby allowing P_D and P_{FA} to be determined for a given threshold. Further, by analyzing two points while increasing the distance between them on each analysis, the autocovariance function of the background noise can be found. Then by taking the Fourier transform, the noise power spectrum is known and from it the noise bandwidth can be determined.

4.2.3 Computer Listings

The listings of the programs described in Section 4.2 are provided in the appendices in the following order: The simulation programs (Appendix A) and the two statistical evaluation programs (Appendices B and C). The last two listings are essentially the same except that the first allows the computation of the normalized autocovariance function of background noise whereas the second does not. The second program was specifically written for the inclusion of images as well as background noise.

The specific parameter values listed and the arrangement of DO-loops are changed in all the programs to accommodate various operating conditions. As listed, only a specific tube and operating mode is represented.

SECTION V

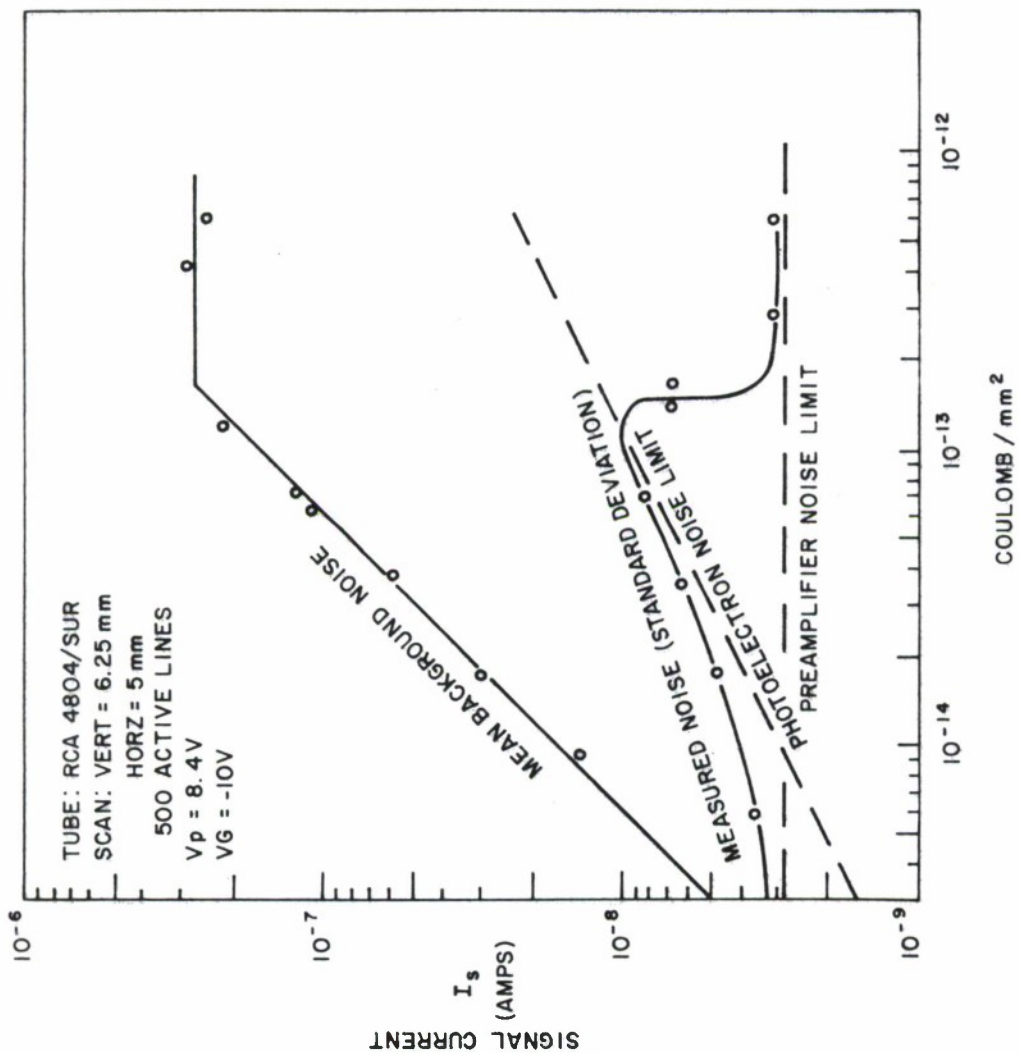
RESULTS AND COMPARISONS WITH EXPERIMENTAL DATA

The simulation program described in subsection 4.2.1 and the statistical evaluation program described in subsection 4.2.2 were run, and when available, experimental data were used to examine the trend results of the model. In some cases, specific tube and operating parameters were known and were inserted into the model so that direct instead of trend comparisons could be made.

Of interest were flat-field response (i.e., only background noise was present), point-source response, response to images in the presence of background noise, and resolution. Within these broad interests were some critical interest items of tube response. These included saturation effects, image splitting, point spread and modulation transfer functions, signal to noise ratio, probability of target detection, and probability of false alarms caused by background noise for given threshold settings.

5.1 Flat Field Response

The signal current as a function of uniform illumination of the photocathode is defined as the flat field response. In Figure V-I, typical response curves are shown for an EBSICON tube. These curves are based on measurements made by the ITEK Corporation on an RCA 4804/SUR sensor. The top curve shows the flat field response of the mean signal current while the lower curve shows the behavior of



EXPOSURE ON PHOTOCATHODE
(PHOTOCATHODE AREA EQUAL TO TARGET AREA)

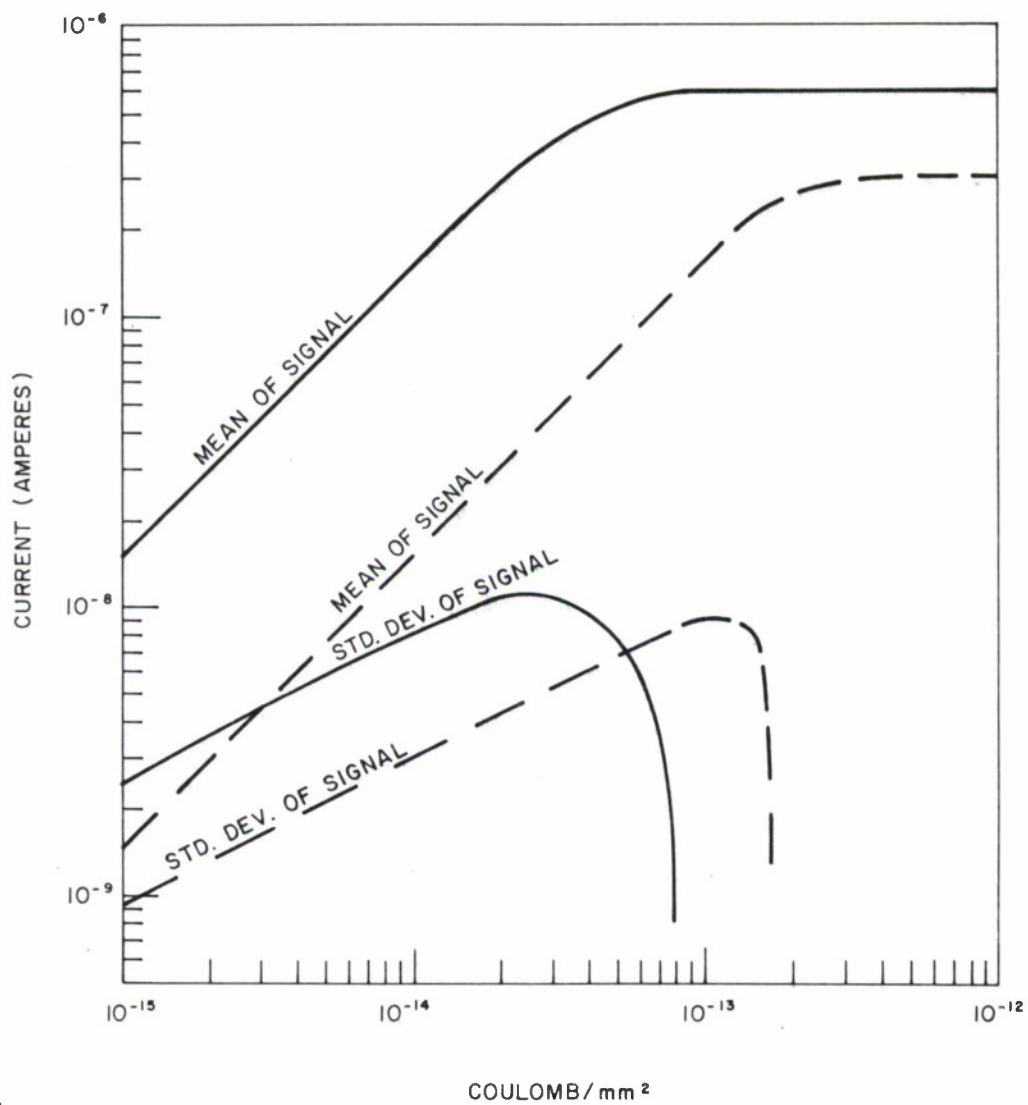
Figure V-I EBSICON CAMERA BROAD AREA TRANSFER CHARACTERISTICS AND CAMERA NOISE
(FROM TRW-ITEK REPORT 26499-6001-RU-00, DEC 74)

the RMS noise values associated with the mean signal currents. The flat field response clearly has two distinct sections: The straight line inclined at 45° representing the linear part of the sensor response ranging over about two decades, and the horizontal part of the curve indicates saturation of the sensor. The curve representing the RMS values also shows several interesting features. For both very low and very high input levels this curve approaches a constant in the vicinity of 3×10^{-9} amp., the preamplifier noise. If this preamplifier noise is subtracted* from the measured RMS values, a straight line is obtained with a slope of one half. This curve represents the photo-electron noise limit. At the saturation point the measured RMS value drops rapidly to the amplifier noise. This corresponds exactly to the expected behavior.

These experimental results were used for comparison with the output of the computer model (Figure V-2). The curves shown in Figure V-2 include those of Figure V-1, replotted with the preamplifier noise subtracted. Four curves are shown; the solid lines represent the computed values and the dotted lines are the experimental results. Both sets of results were obtained independently and several operational parameters were different, and for this reason their influence must be considered in order to make a

*Subtraction here is understood to apply to the variances of both the measured values and the preamplifier noise

$$\sigma_{\text{Photo-electrons}} = \sqrt{\sigma^2_{\text{Measured}} - \sigma^2_{\text{Preamplifier}}}$$



1A-46,414

Figure V-2 EXPOSURE ON PHOTOCATHODE
(PHOTOCATHODE NORMALIZED TO BE EQUAL TO TARGET SIZE)

quantitative comparison. But some basic facts can be obtained immediately:

- o The computed flat field response curve has the same shape as the experimental one; a linear range (unity slope) and a sharp knee, where it turns into the saturation region (horizontal line).
- o The curve representing the RMS values again has the same shape as the experimental curve; it follows a line with a slope of one half and at the saturation point it drops to zero very rapidly.

In order to compare the curves quantitatively the following facts have to be considered:

- o The areal scan speed in the case of the computer simulation was $9 \times 10^4 \text{ mm}^2/\text{sec}$, but in case of the experiments it was $9.4 \times 10^3 \text{ mm}^2/\text{sec}$. Since the signal current in case of flat field illumination is directly proportional to the areal scan velocity, it would be expected that the computer simulation values would be higher than the experimental results by a factor 10. If the experimental curve in Figure V-2 is shifted by this amount, the linear sections of both curves coincide exactly.
- o In the computer simulation, read beam saturation took place, while in the experiments, target saturation occurred. The read beam limitation for the experimental curve should be

approximately $6 \text{ to } 7 \times 10^{-7}$ amp. If the read speed in the experiments had been increased by a factor 10, beam limitation would have occurred at this value and both the experimental and computed response curves would coincide entirely.

- o The RMS noise current is proportional to the square root of the areal scan velocity; in this case the computed values would be expected to be higher than the experimental results by a factor of approximately 3.3. Figure V-2 shows that the factor is approximately 2.7. This discrepancy can be explained by correcting for the smaller read beam diameter used in the experiments, which results in a smaller integration area and therefore larger noise values. If the experiments had been run under beam limiting conditions with 10 times the scan velocity, both RMS curves would coincide also.

In other words, by properly accounting for the different operational parameters, the curves can be normalized and the resulting pairs of curves in Figure V-2 could be made to coincide in slope, absolute values and in saturation values. The comparative results are encouraging. Additional simulations with matched parameters are planned and should furnish further verification of the mathematical model.

5.2 POINT SOURCE RESPONSE

Shown in Figure V-3 is the basic point response characteristics of the model obtained from the simulation program described in section 4.2.1. The response is presented in the form of a signal

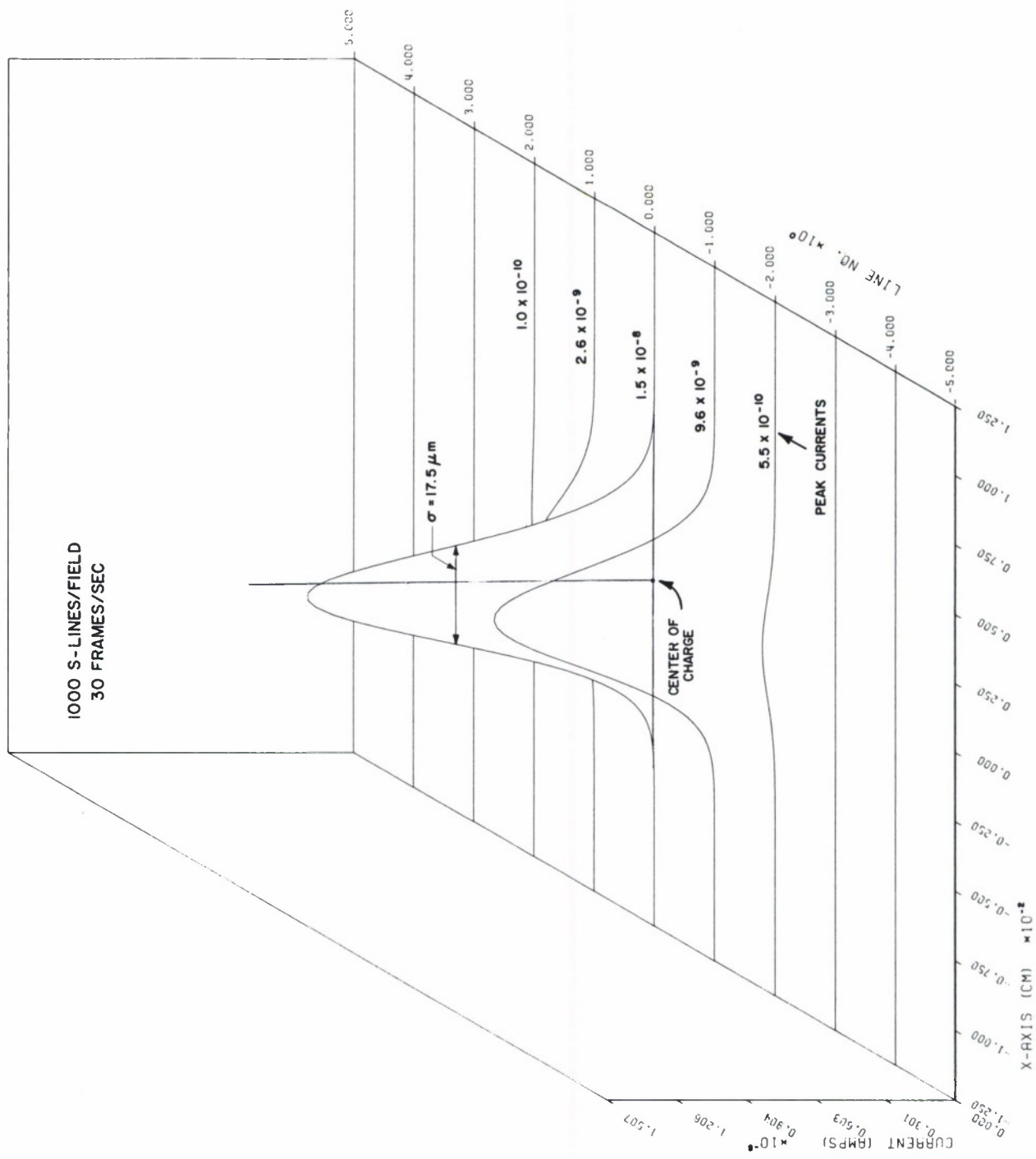


Figure V-3 POINT RESPONSE

current "map" which geometrically overlays the diode array (not shown). The read process goes from left to right and from bottom to top. Several effects are to be observed; the point readout characteristic is asymmetric in both directions and there is image splitting. That is, the image current appears on a number of lines even though the image charge is located under the zeroth line only. Experimental point-source data from the University of Rhode Island is shown in Figure V-4. These characteristics are similar, with respect to image splitting, but with regard to the apparent asymmetry, the necessary instrumentation was not available to know the actual location of the point source with respect to the scan lines. Therefore, these data may provide misleading comparisons regarding asymmetry with the response of the model.

Another feature of asymmetry is shown in Figure V-3. There is considerably more peak current read out on the line before the center line compared to that on the line after the center line. With a slower read-out velocity, as shown in Figure V-5, the main peak, in fact, occurred one line early. In Figure V-6 where the read-out speed was the same as that used to produce Figure V-3, the point appears to have been half way between the center line and the preceding line. Actually, the image charge was located on a diode only one quarter of the distance from the center line to the preceding line. This feature illustrates a flaw in the usual experimental procedure in which a point source is centered on a scan

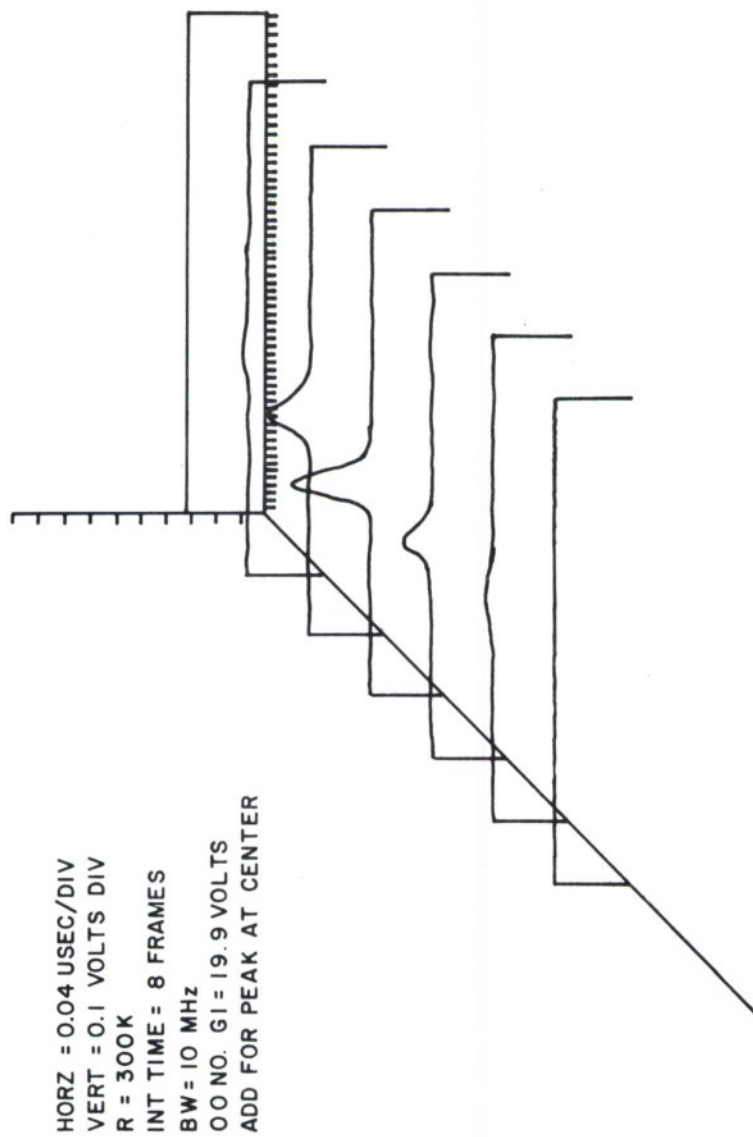


Figure V-4 EXPERIMENTALLY MEASURED POINT SOURCE RESPONSE

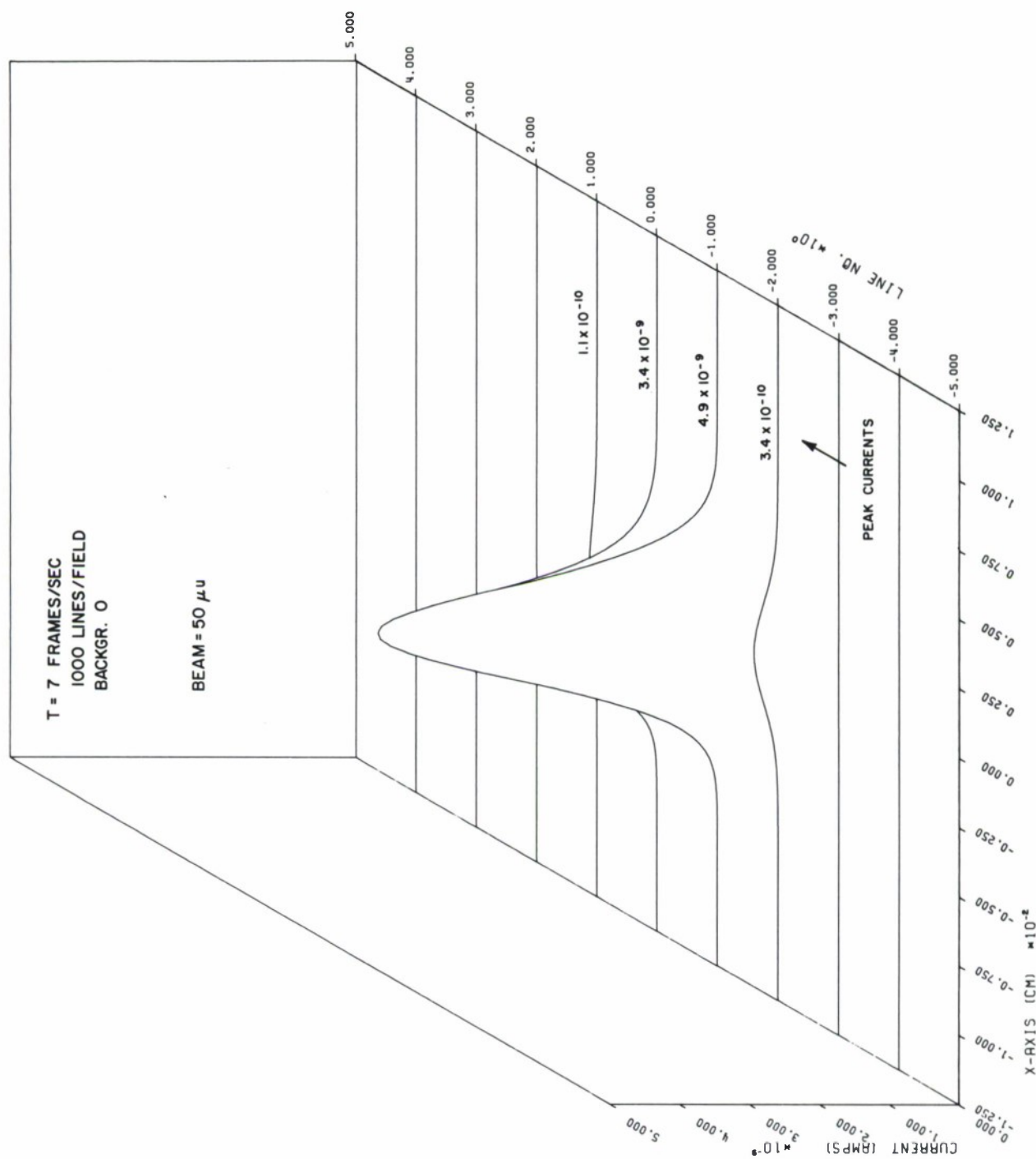


Figure V-5 POINT RESPONSE

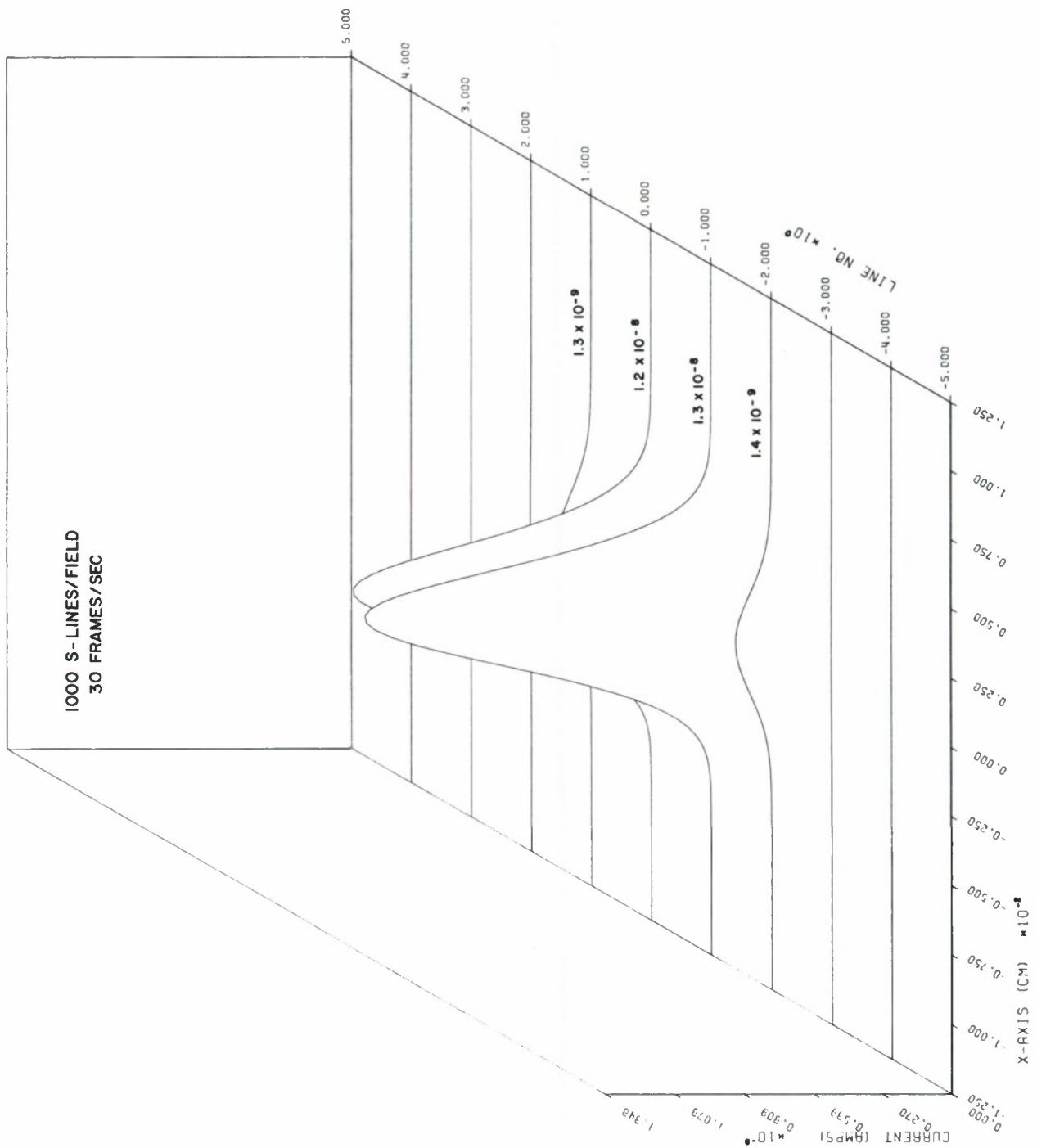


Figure V-6 POINT RESPONSE

line. In the procedure, the scan line locations are adjusted so that the equal height peaks are obtained on the two lines adjacent to the one containing the main peak. The model shows that without background (discussed in the next section), this procedure does not physically locate the point source on the target (called mechanical boresighting).

In all of the above cases the image was confined to one diode (the smallest possible image) and the background was set to zero. However, response to images distributed over a number of diodes is of interest. In particular the ratio of the mean signal current to the mean flat-field current as a function of image area on the target provides insight in cases where images are blurred by optical, atmospheric and other effects. This ratio will show a maximum image area beyond which the contribution to read-out current is no longer affected by increased image area. These data, obtained from the Night Vision Laboratory of the Army, were taken in which the illumination density was kept constant but the spot (image) size was increased. The same simulated data were taken from the model and they are compared in Figure V-7.

It is seen that the read-out process behaves as an energy analyzer for spots of less than $.004$ to $.008 \text{ m}^2$ in area and as an energy density analyzer for larger spots. In the simulation, the behavior was the same and practically the same spot area was obtained for the transition from one regime to the other. The

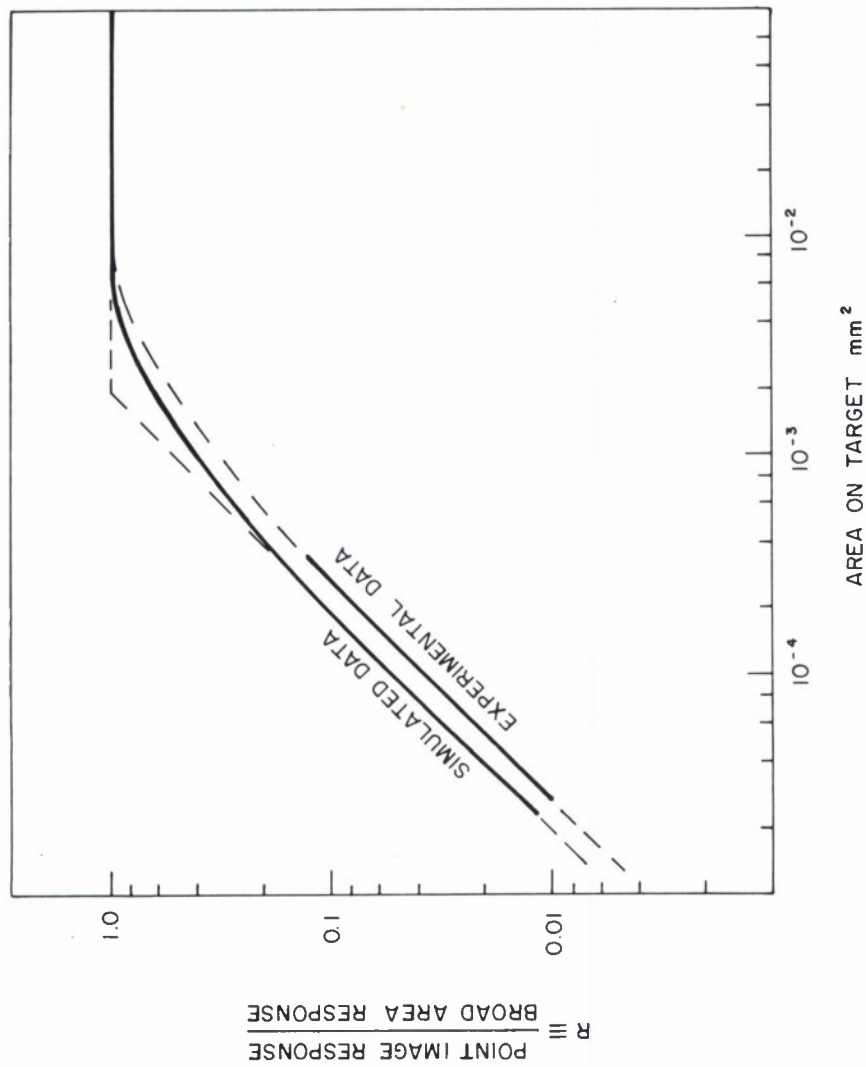


Figure V-7 SPOT IMAGE RESPONSE/BROAD AREA RESPONSE vs SPOT SIZE
(EXPERIMENTAL DATA FURNISHED BY R. GRAFT, ARMY NIGHT VISION LAB)

differences observed are due to the fact that the read-beam diameter was not determined in the experiment; it was estimated and set in the simulation to be 50 μm , which may have been too small.

5.3 POINT SOURCES IN THE PRESENCE OF BACKGROUND NOISE

The more realistic situation is where there is a point source which is to be detected but is observed in the presence of background noise. Figure V-8 shows the simulation of this situation where the intensities of the image and background were chosen to represent the most difficult GEODSS case. The point source consisted of an equivalent of 130 electrons released from the photocathode to one diode and the background consisted of the equivalent of an average of 2×10^8 electrons released by the total photocathode area.

The presence of background changes the point response considerably in a number of ways. First, it is seen that the response is more symmetrical. The peak-current location on the current map occurs more nearly to that of the location of the center of the image charge along a scan line (Figure V-8). Secondly, as shown in Figure V-9, when the point image is moved one-quarter the distance from the center line towards the preceding line, the largest peak still occurs on the center line. This is quite a different response than that shown in Figure V-6 where the image was moved to the same location, but where there was no background. It indicates that but the point response is more symmetrical in the vertical direction as

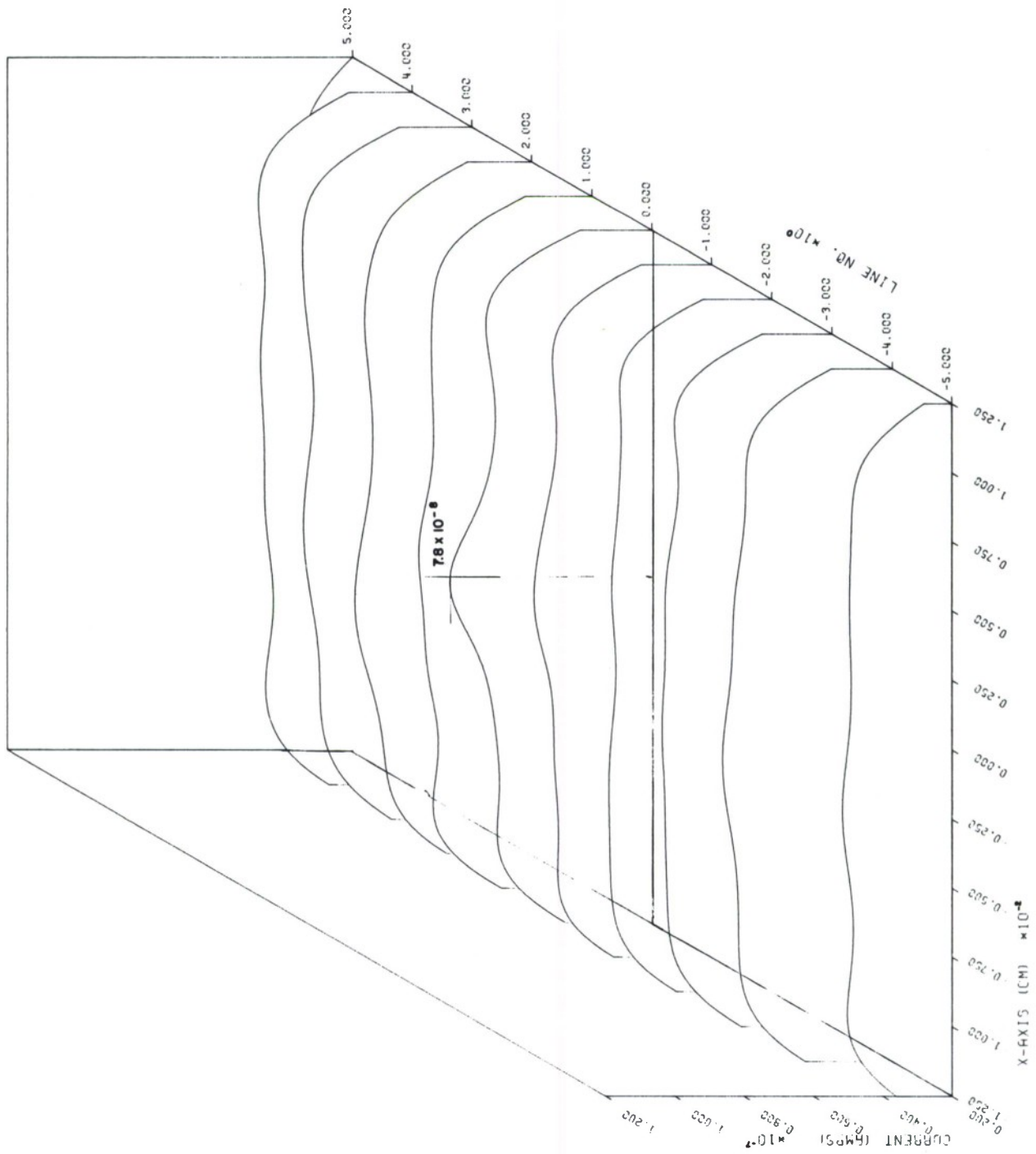


Figure V-8 POINT SOURCE PLUS BACKGROUND

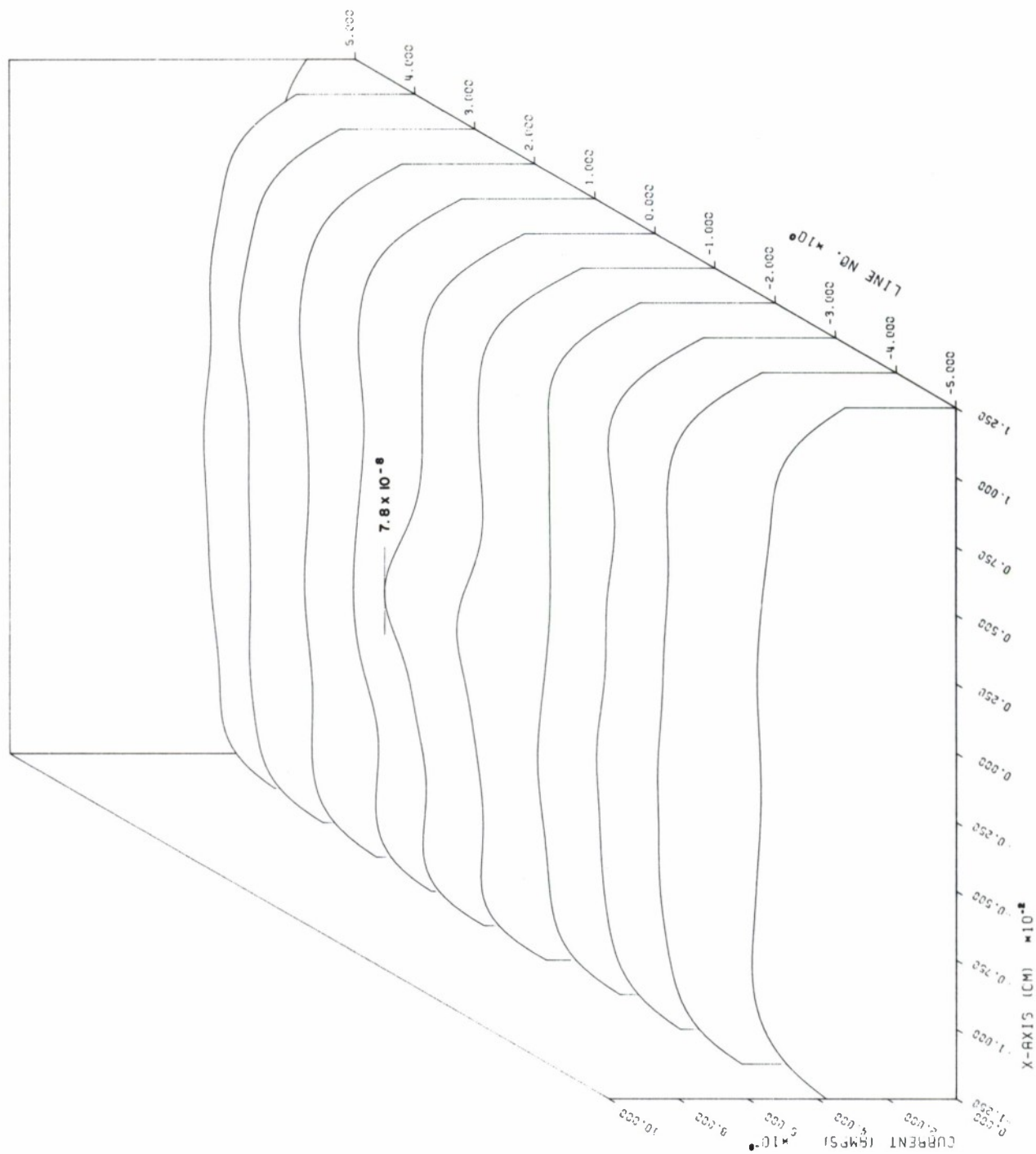


Figure V-9 POINT SOURCE PLUS BACKGROUND

well. Figure V-9 illustrates this fact better than Figure V-8, although it is somewhat visible there too, but is obscured by the response to the background noise.

Distributed point-source response was also of concern for reasons stated earlier. An image corresponding to a total of 130 photoelectrons was distributed using three simulation runs from one diode to four and then to nine diodes to observe the change in shape of peak current as well as the change in the magnitude of the peak. As shown in Figure V-10, where the image is distributed over four diodes, there is little change in either feature but it was observed that there was considerable change when the image was distributed over 9 diodes.

While the change in point response as a result of adding background is significant, probably the most important considerations are those of signal to noise ratio (SNR), probability of detection (P_D) and probability of false alarm (P_{FA}) caused by peaks in the background noise. The ability to determine these is crucial to overall GEODSS system design, and the statistical evaluation programs, described in Section 4.2.2, were and shall be used extensively to determine these numbers. Examples of the use of this program will illustrate how they are determined.

As indicated earlier, through a separate analysis (not published), the probability density function (PDF) of the current contribution from a single diode was computed and plotted. It was found that its

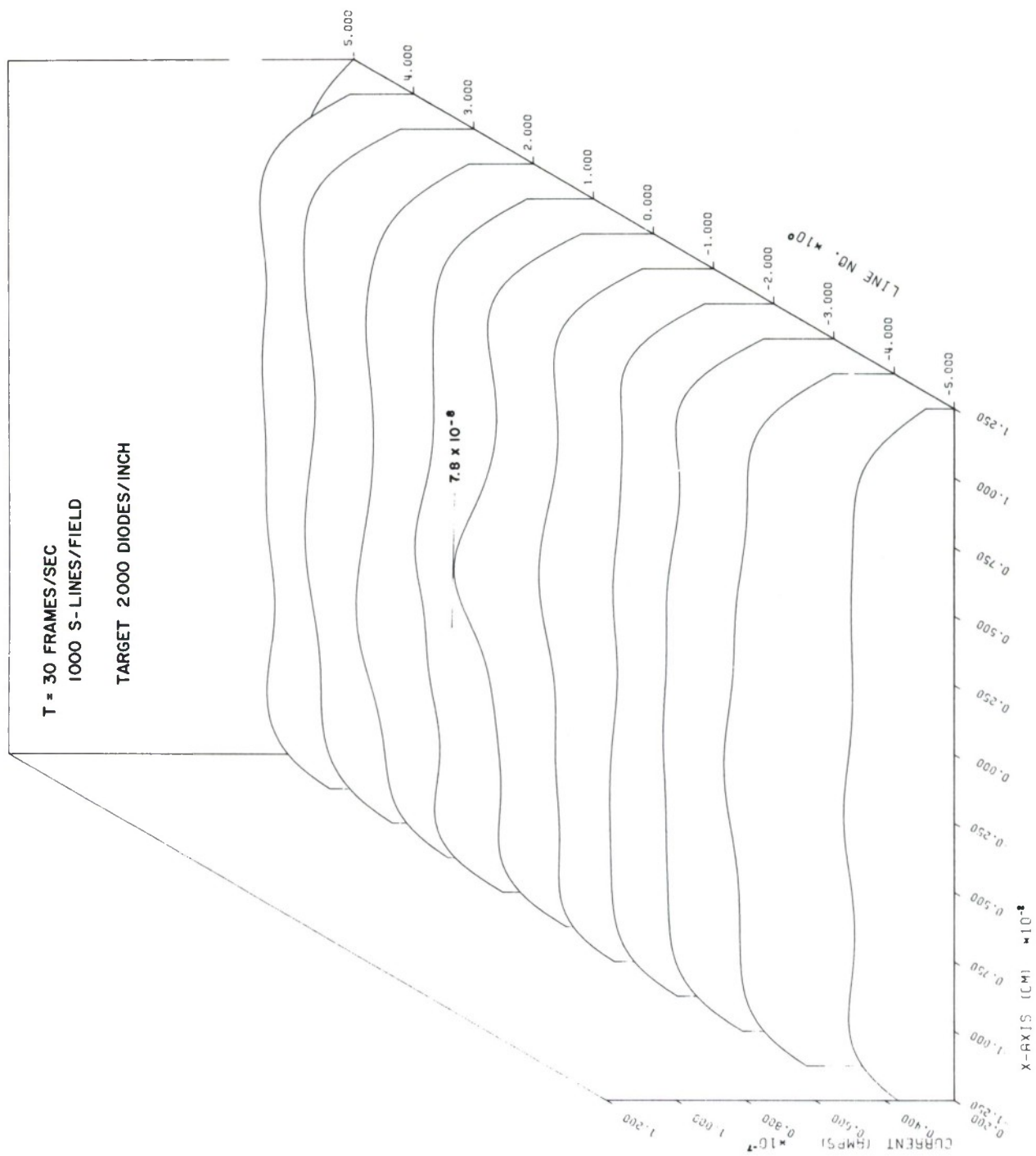


Figure V-10 EXTENDED POINT SOURCE PLUS BACKGROUND

shape matched the Gaussian PDF shape very closely over a wide range of illumination and read-out speeds. Since the read-out beam irradiates a number of diodes causing their current contribution to be weighed and summed, the PDF of the sum of the contributions will approximate a Gaussian PDF more closely. This was born out experimentally by the University of Rhode Island as shown in Figure V-11.

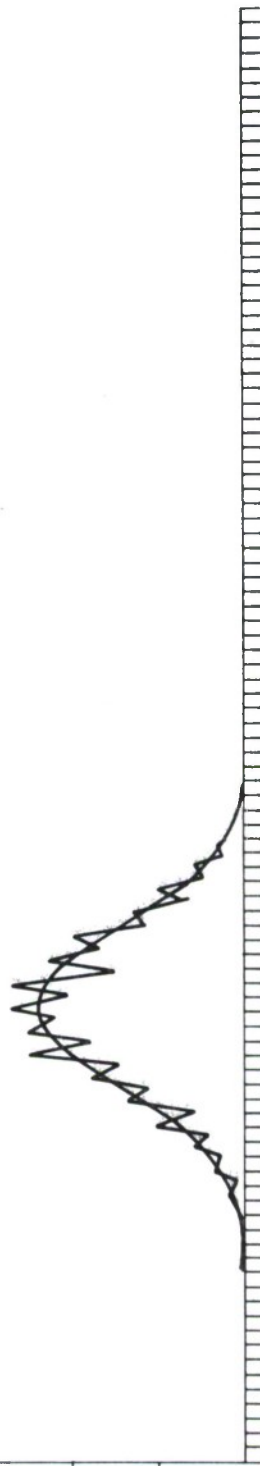
Hence, with the ensemble means and standard deviations, computed by the statistical evaluation programs at a point where the peak image signal is located, the equation for ensemble PDF's can be written. Two cases can be considered; one in which only background noise is present and the other where an image is also present. SNR can also be determined the results of these two cases as:

$$\frac{(\text{Mean of signal + background}) - (\text{Mean of background})}{(\text{standard deviation of signal + background})} \quad (5.1)$$

The PDF's of Figure V-12 and V-13 were obtained in the way just described using a set of typical tube and operating parameters and with two background illuminations but with the same image intensity. In these examples, if as shown in the figures the detection threshold is set so that a P_D of .983 required by the GEODSS system is achieved, there is a drastic difference in the P_{FA} 's. In Figure V-12 the P_{FA} is .00006 whereas in Figure V-13 the P_{FA} is .0323, a difference of more than 2 1/2 orders of magnitude. In both figures, P_D is equal to the area to the right of the threshold line under the P_{DF} curve on the right while P_{FA} is equal to the area to the

IA-46,359

PDF



SCALE = 0.156256 - 02 VOLTS / DIV

RMS NOISE = 0.104606 - 01 VOLTS

Figure X-11 MEASURED PDF OF OUTPUT NOISE

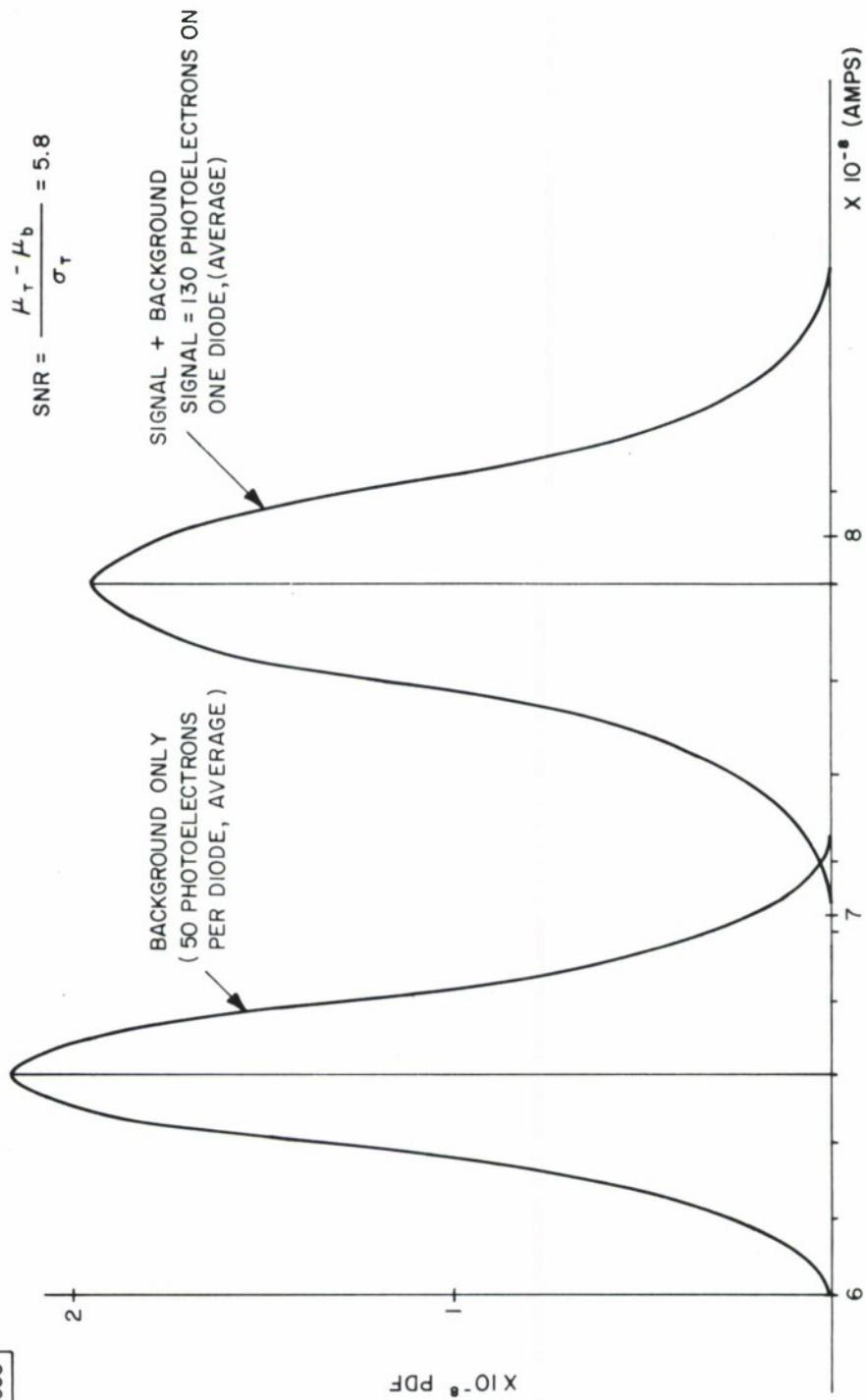


Figure V-12 PDF'S OF SIGNAL + BACKGROUND AND BACKGROUND ALONE

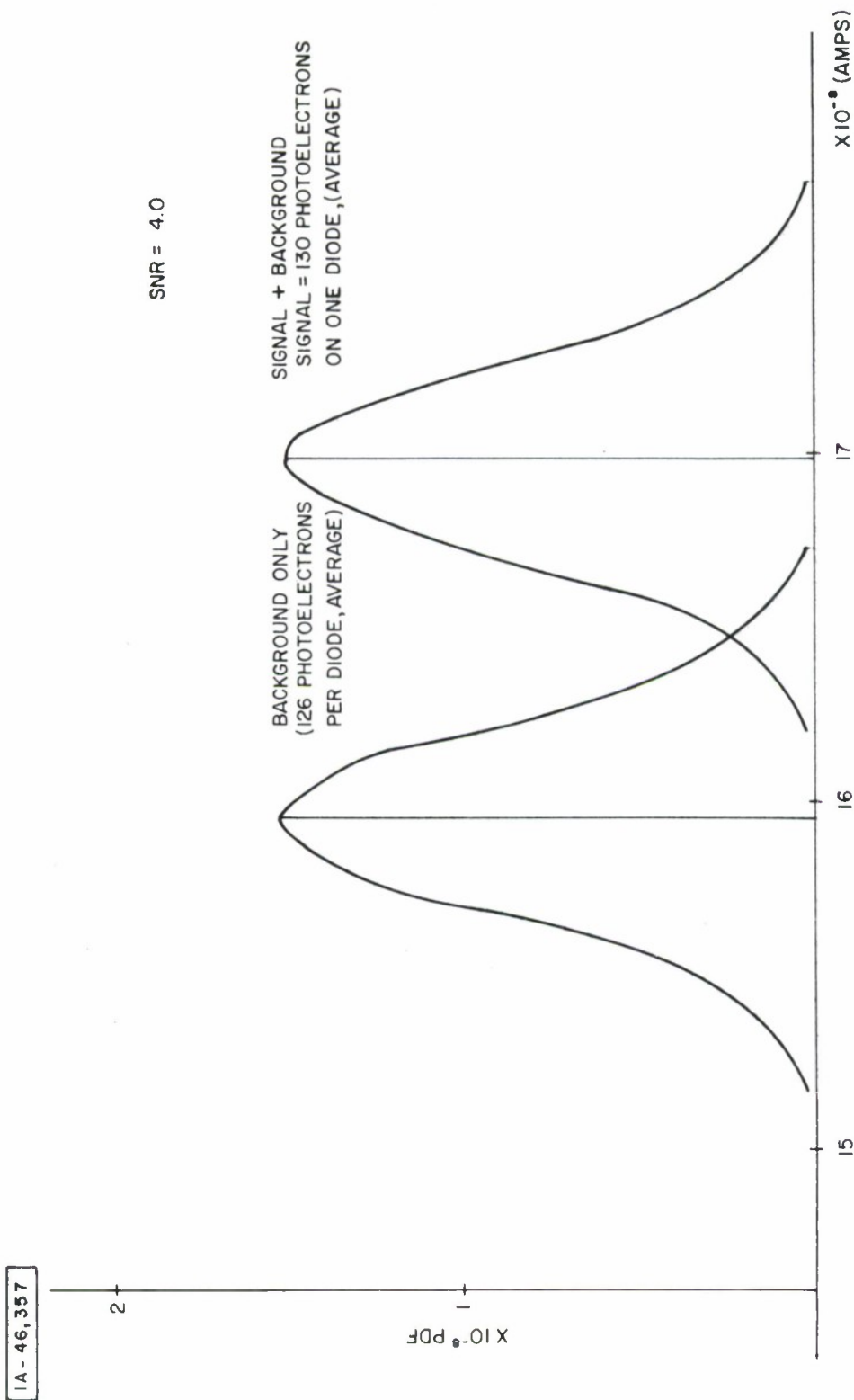


Figure V-13 PDF'S OF SIGNAL + BACKGROUND AND BACKGROUND ALONE

right of the threshold line under the P_{DF} curve on the left.

A capability of the model is the ability to easily relate SNR of the output current back to the SNR on the target, thereby defining a maximum area on the target affecting the output SNR. As described in Section 4.2.2, the mean and variance of the current is computed for each diode and, since each contribution is independent, they are summed to get the total mean and variance of the target current. Hence each diode contribution is individually identified in the model, which is not the case in the usual operation of an actual EBSICON. Herein lies a powerful capability of the model when exercised, for example, as described in the following investigation.

The authors were interested to know whether there existed a minimum area on the target so that the noise from any larger area had no effect on the SNR of the output current. So, instead of summing all the weighted contributions to determine SNR of the output, separate specialized computer runs were made. SNR was calculated, using equation 5.1, but only contributions from subarrays were used to obtain the means and standard derivations. First a one diode array was used, then a 2 x 2 diode subarray was used continuing to a 3 x 3 subarray, etc. Each subarray contains the signal peak. In Figures V-14 and V-15, the resulting SNR is plotted as a function of the number of diodes on a side of each square array. It is seen that in both cases each curve reaches

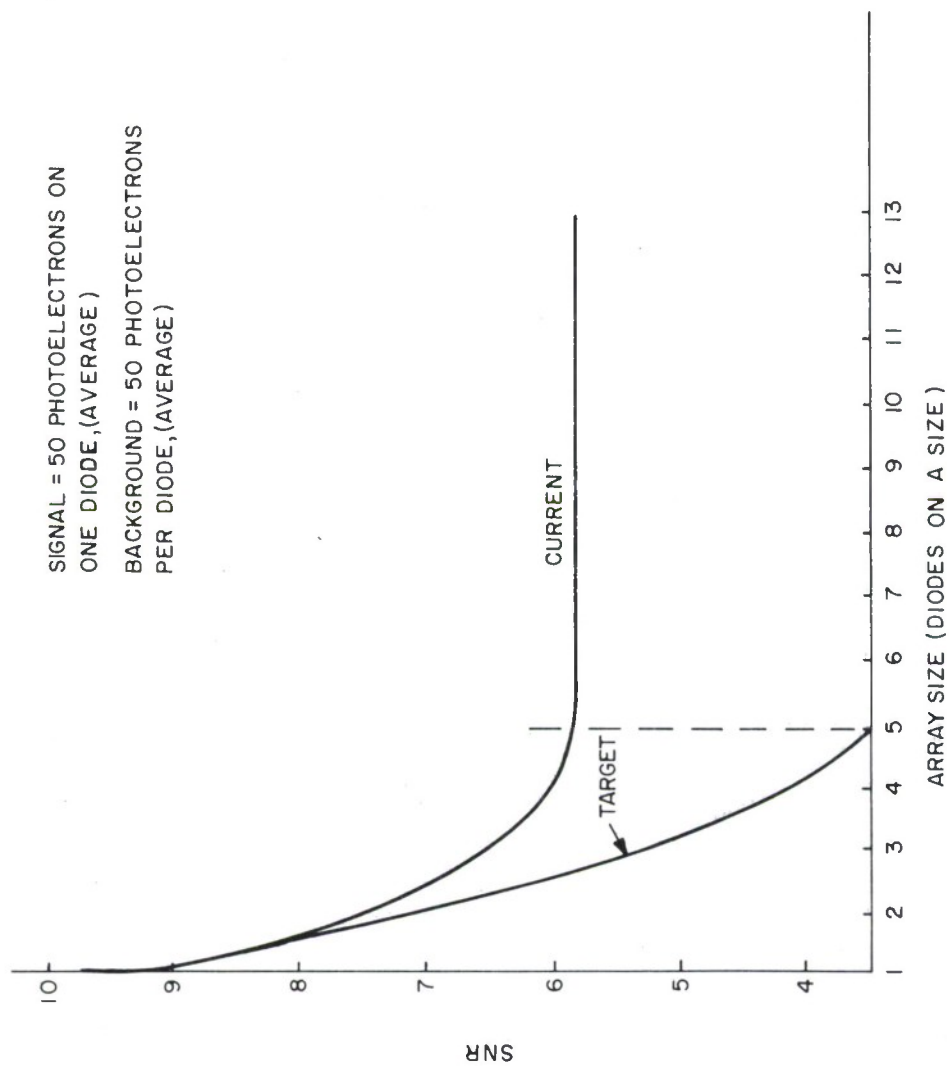


Figure V - 14 SNR TRANSFER FROM OUTPUT TO TARGET

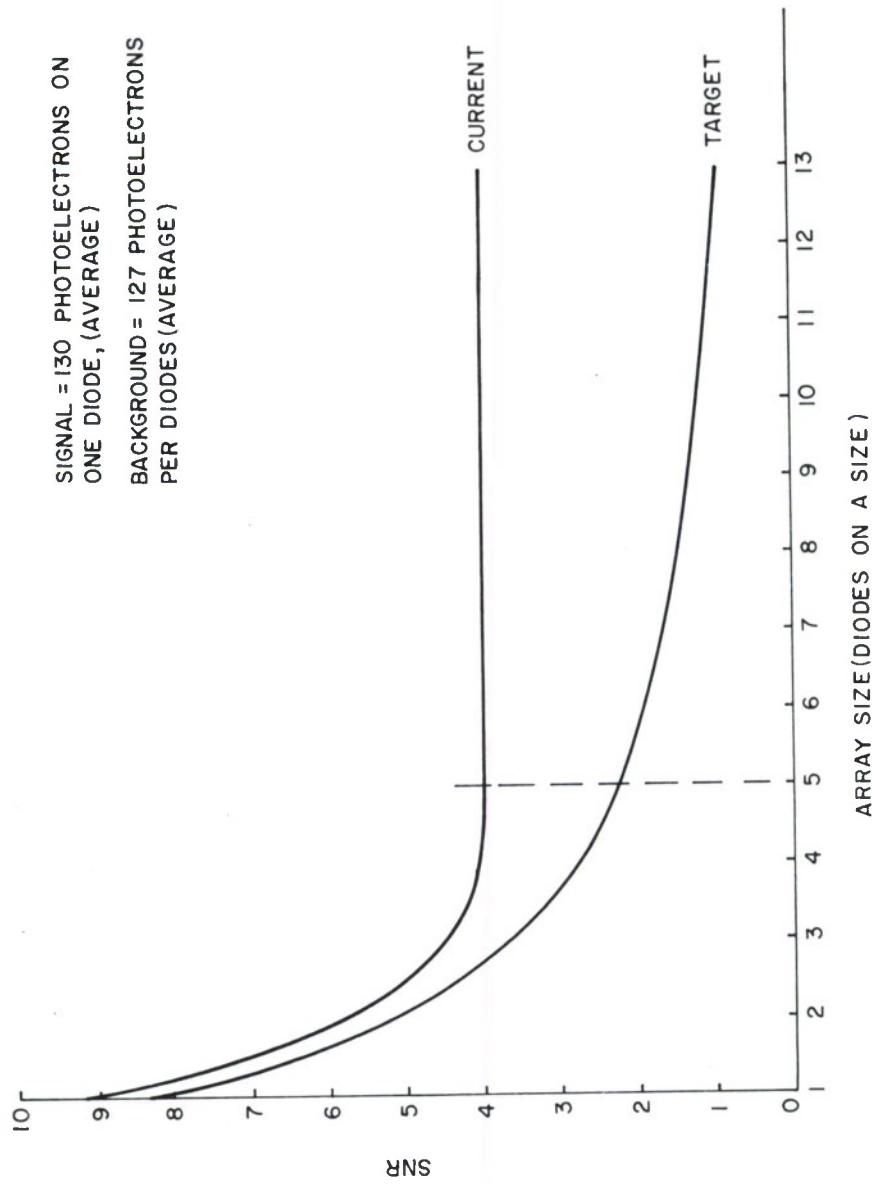


Figure V-15 SNR TRANSFER FROM OUTPUT TO TARGET

the final SNR when the contributions are summed from a subarray of 5 x 5 diodes. This area ($.004 \text{ mm}^2$) corresponds remarkably well with that determined in Figure V-7 ($.004$ to $.008 \text{ mm}^2$). Thus contributions from larger subarrays do not affect the SNR of the output. It is important to define the maximum area on the target that need be considered for SNR computations. Considering areas larger than this yields a lower SNR on the target which would require a larger telescope to regain or improve the SNR. Further consider the implications of Figure V-14, for example. If the output SNR of 5.8 is acceptable for the GEODSS system, then the required SNR on the target need be only 3.5 (not 5.8). This reduction has a large impact upon the sizing of the optical system used to illuminate the image tube. In this case the reduction represents a 40% reduction in the telescope diameter. The target area defined above is most likely signal and background dependent, but nevertheless, the above capability can be used to easily examine many anticipated conditions and which is not possible to do using an actual tube.

Another feature of the model described in Section 4.2.2 is the ability to obtain the normalized autocovariance function of the video output noise shown in Figure V-16 for typical tube and operating parameters. The Fourier transform of this function yields the power spectral density and the intrinsic bandwidth of the video noise.

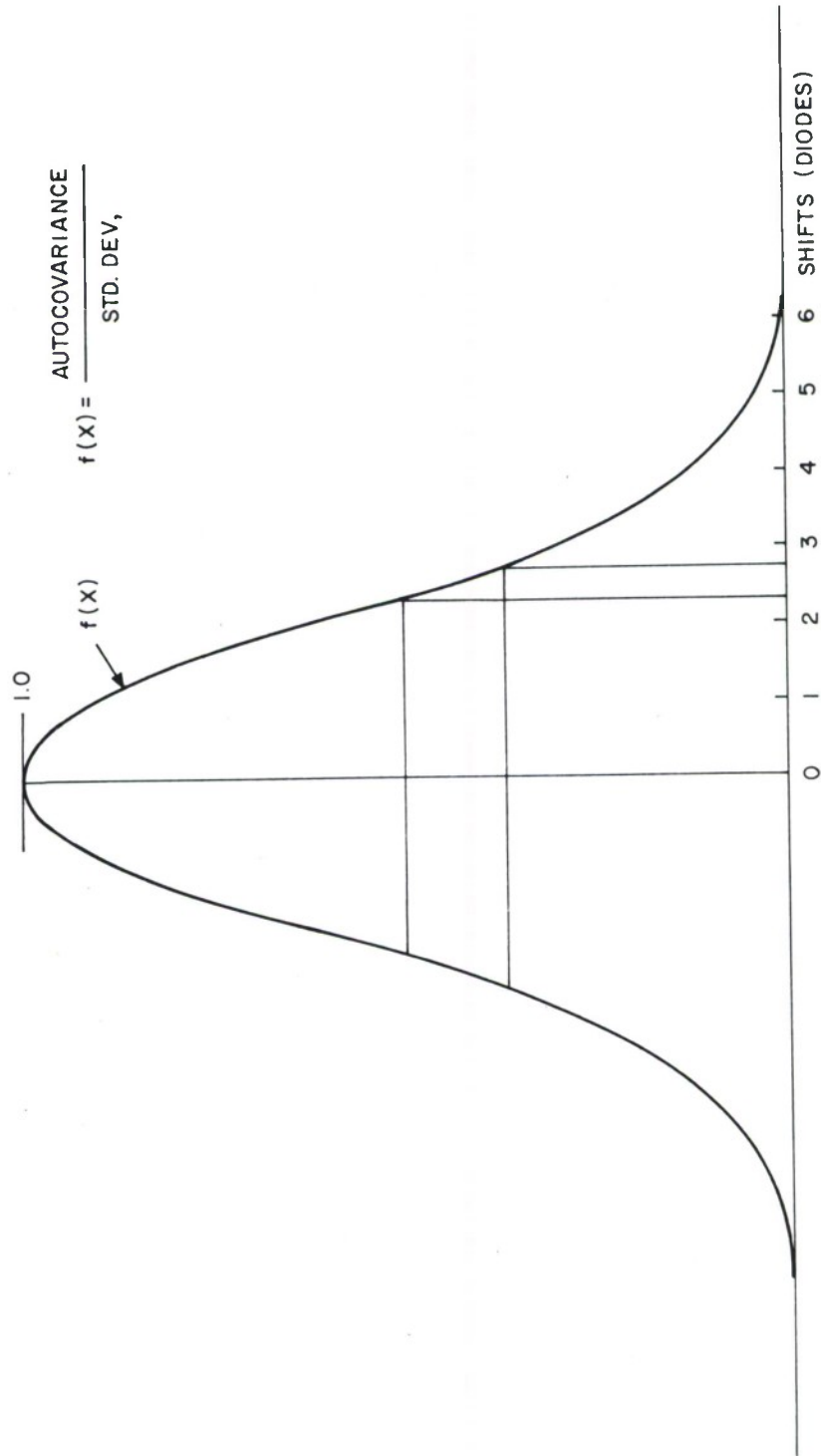


Figure V -16 NORMALIZED AUTOCOVARIANCE FUNCTION

5.4 RESOLUTION

Resolution is usually measured by illuminating the photocathode with a bar chart consisting of vertical or horizontal bars alternating from solid black to solid white and extending in length from near the bottom to near the top of the picture or from one side to the other (called TV lines). A typical output current map is shown as simulated in Figure V-17 for a particular bar chart. The output current is measured for specific spacings of the bars (i.e., the number of TV lines per raster height). As the number of TV lines per raster height is sequentially increased (i.e., different bar charts with closer spaced bars), the maximum minus the minimum output current is divided by the maximum plus the minimum output current. The resultant function is called the square wave response or modulation transfer function (MTF).

Comparison of the model was made with two sets of experimental MTF data shown in Figure V-18. The curve marked with circles shows Night Vision Laboratory data of a tube with a similar but smaller target. The curves marked with x's and triangles are simulated MTF data using a 65 μm and 50 μm read beam respectively. The dashed curve is the present estimate of the new Westinghouse 80/32 tube (Section II) MTF. It can be seen that the model has the appropriate trends and that by adjusting parameters in the model that it can be made to correspond well with experimental data.

Resolution would also include a measure of the ability to distinguish between two point sources separated by some minimum

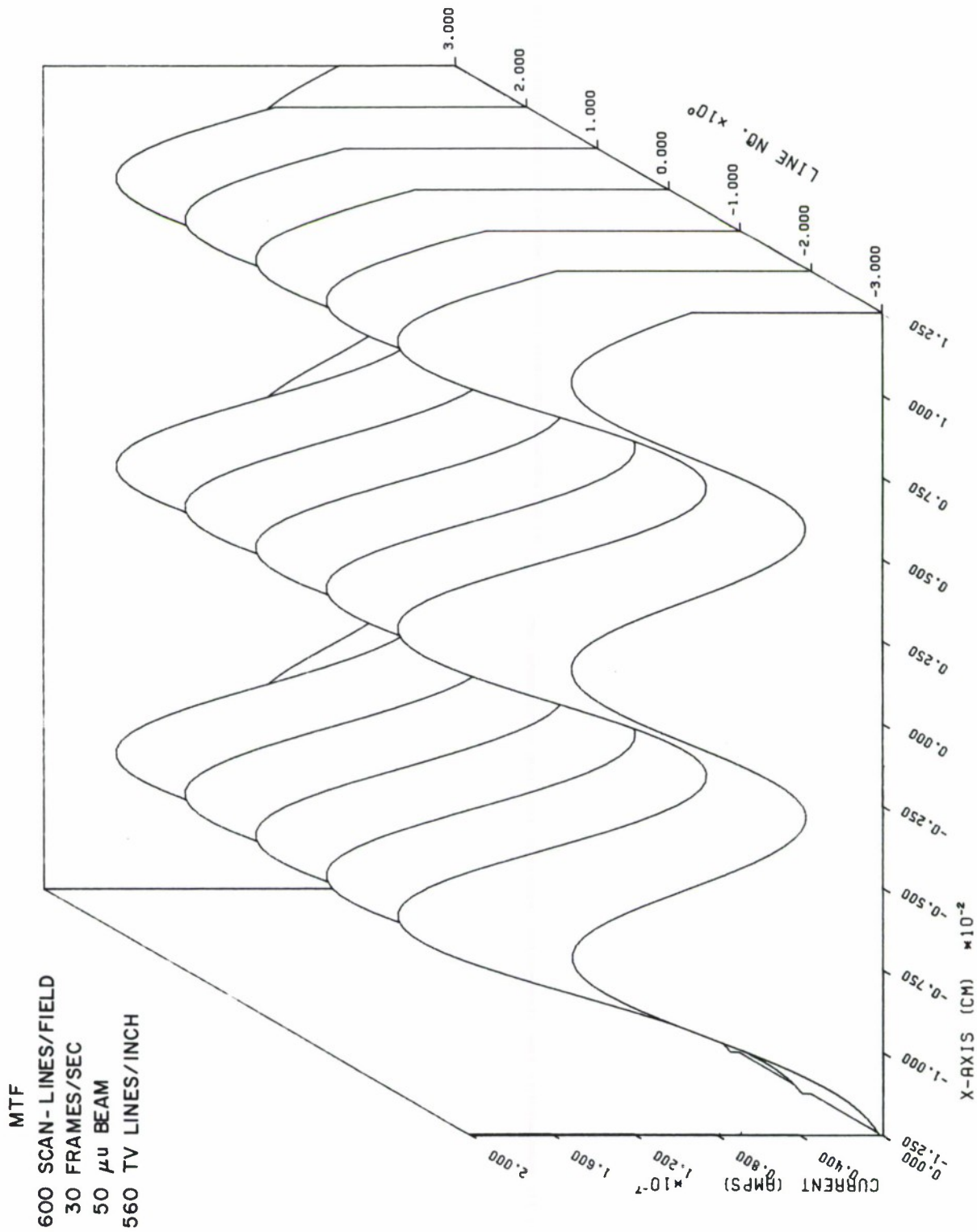


Figure V-17 TYPICAL RESPONSE TO A BAR CHART

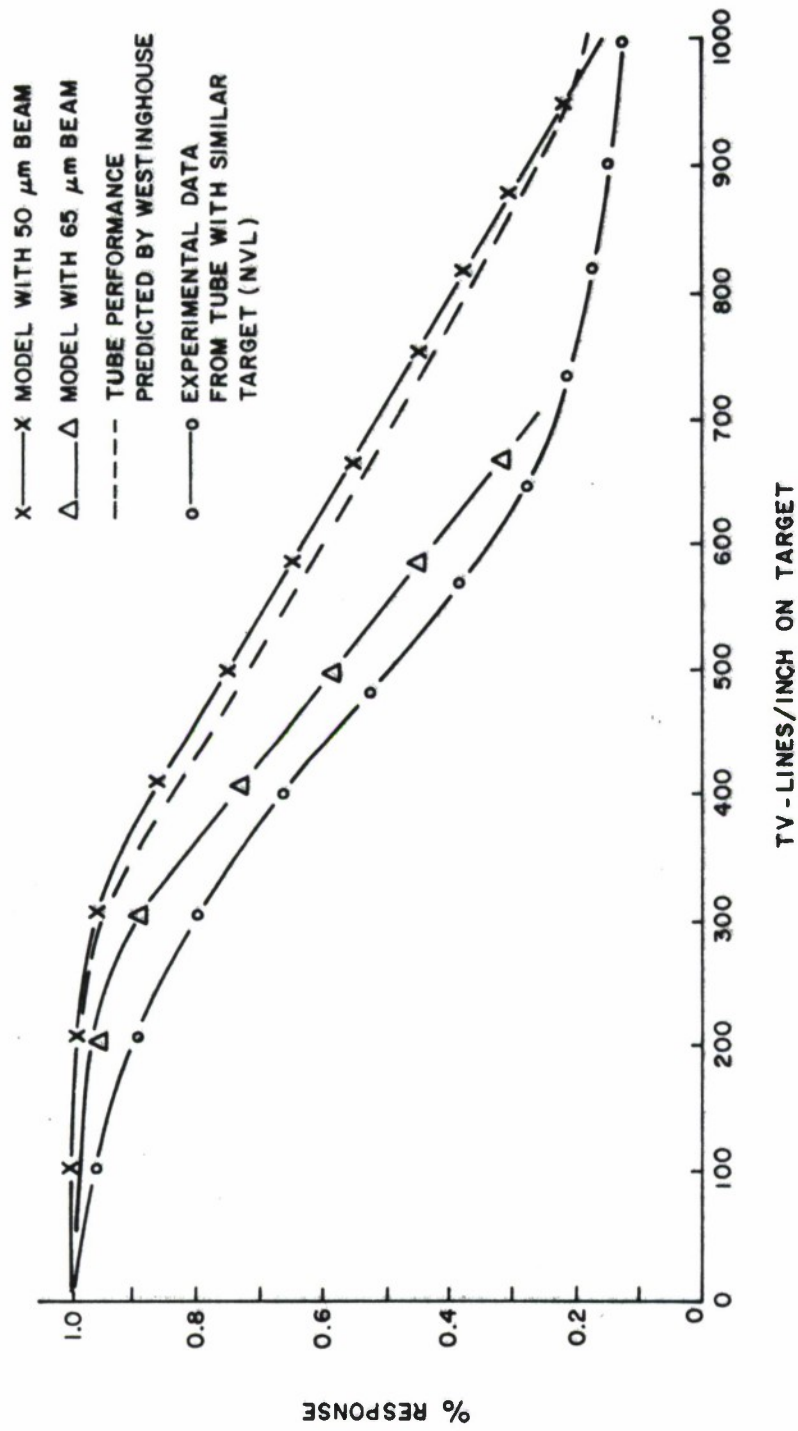


Figure **V**-18 HORIZONTAL SQUARE WAVE RESPONSE OF DIFFERENT TARGETS (EXPERIMENTAL DATA FURNISHED BY: R. GRAFT, ARMY NIGHT VISION LAB AND WEST. CORP. HORSE HEADS N.Y.)

distance. Currently, the authors have no experimental data on point source resolution. The simulation was used with a set of typical tube and operating parameters to examine two-dimensional resolution. Two point images each representing the equivalent of 130 photoelectrons released by the photocathode were localized each to a diode on a scan line and in three separate simulation runs were separated by one, two and then three diodes. Figures V-19, V-20 and V-21 respectively show the output current response maps for these three conditions. As seen, with the 50 μm beam used in the simulation, three diodes of separation are required to clearly distinguish the images along a scan line in the presence of background noise with an average of 50 photoelectrons per diode from the photocathode used in the simulation. Since the points can be placed diagonally or vertically spaced as well, a more complete investigation would be to include the Se cases also. The authors plan to accomplish this when more actual tube and operating parameters become available for the new Westinghouse 80/32 tube,

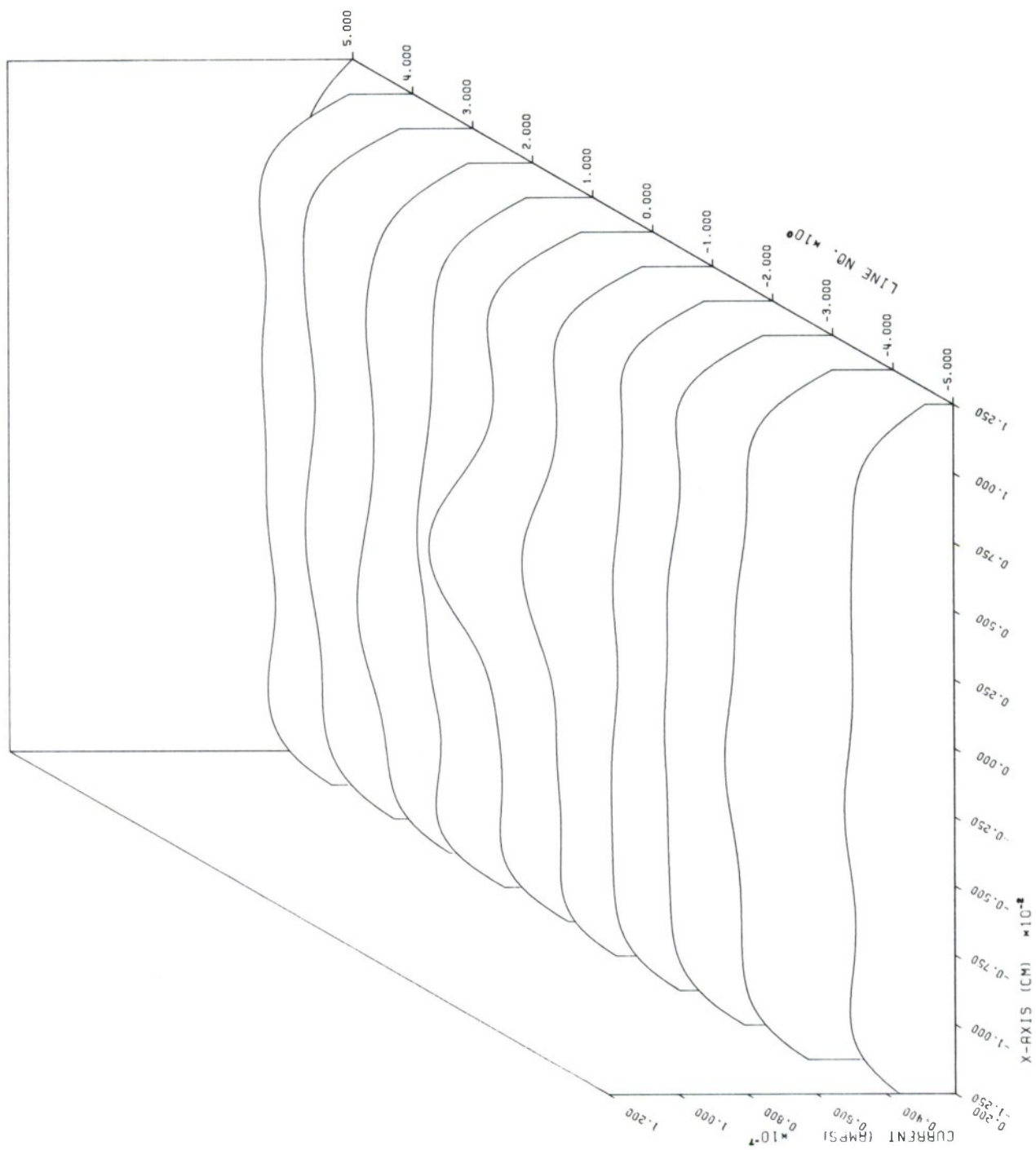


Figure V-19 POINT SOURCE RESOLUTION WITH ONE DIODE SEPARATION

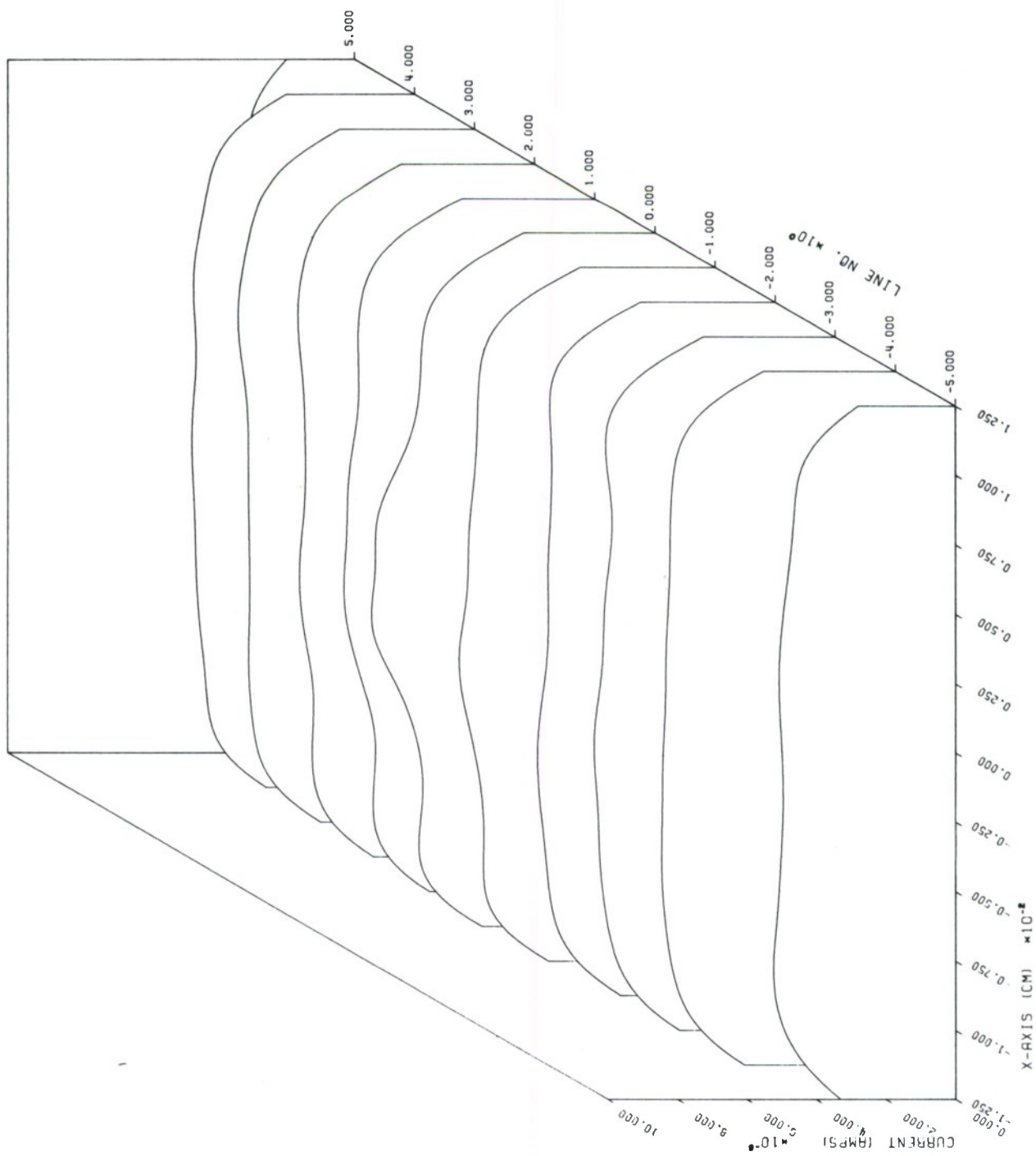


Figure V-20 POINT SOURCE RESOLUTION WITH TWO DIODE SEPARATION

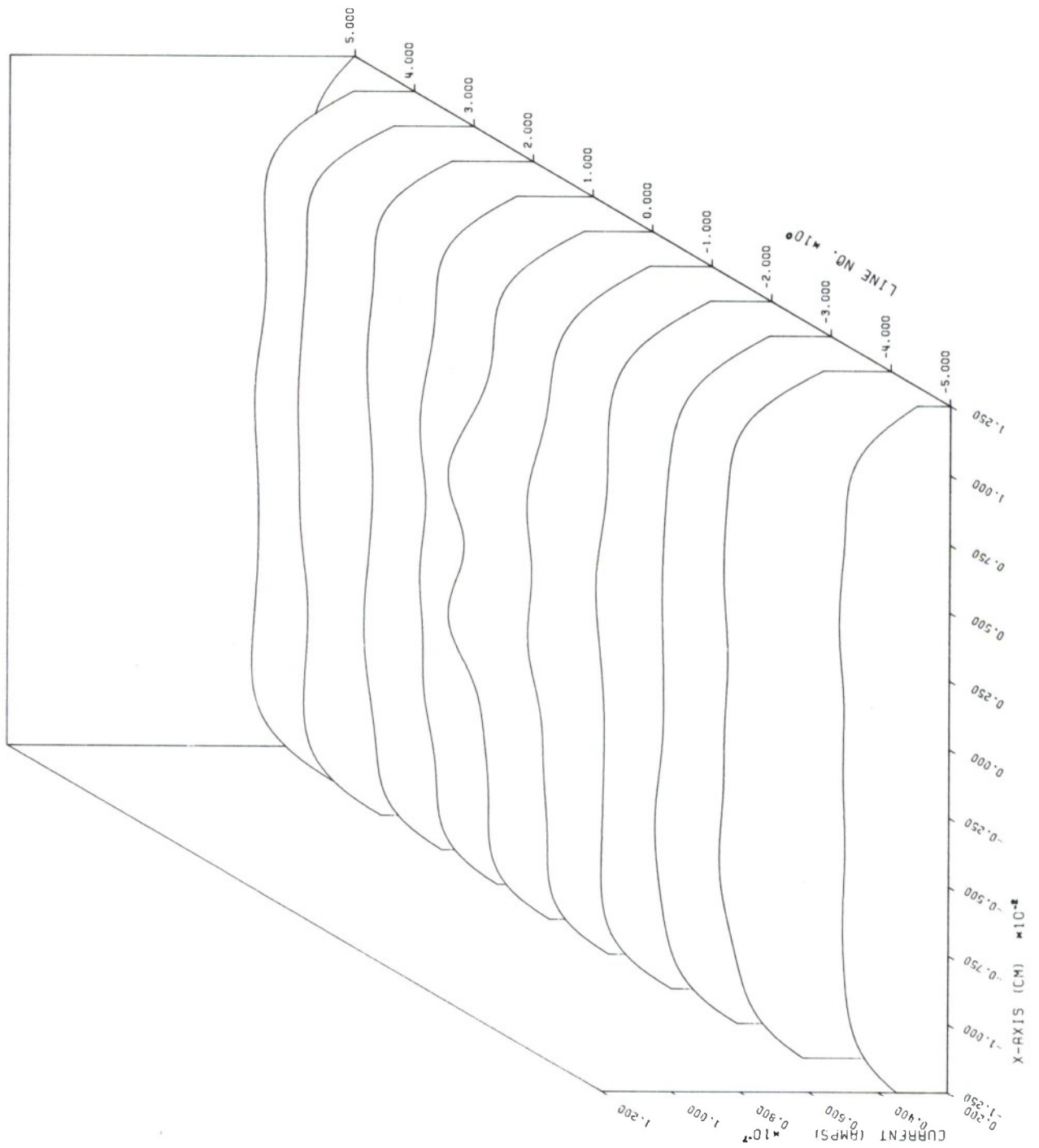


Figure V-21 POINT SOURCE RESOLUTION WITH THREE DIODE SEPARATION

SECTION VI

SUMMARY AND RECOMMENDATIONS

6.1 SUMMARY

The scene to which an EBSICON TV camera tube is exposed depletes charge stored on the target of the tube in proportion to the intensity of illumination over the two-dimensional scene. As discussed in Section III, this exposure process involves the statistical phenomena associated with the photocathode, the gain mechanism, and the charge storage mechanism of the tube target. After exposure, the tube is ready to be read out and the read-out process provides the output video signal of the tube as also described in Section III. The read-out process, as well, restores the charge depleted during exposure.

The translation of the mechanics of the read-out process into closed-form mathematical equations forms the heart of the mathematical EBSICON tube model. The remaining important features of the model are the mathematical descriptions of the statistical phenomena associated with the exposure process.

The model is structured on the basis of contributions to the total output current signal from individually identifiable target diodes. Each contribution is a function of diode capacitance, tube gain, average input signal and background intensities, read-out beam width and current, read-out scan speed, target raster height and width, read-out scan-line density, the voltage at which read-out beam

limitation occurs and the illumination intensity at which target saturation occurs. These are all adjustable parameters in the model thereby allowing the tube designer to predict, before building and testing a tube, the performance of the tube for various tube and operating parameter values and under various illumination conditions. Critical performance trade-offs which can impact cost, can be made.

In addition, due to the structure of the model, it can provide information not easily measured (nor usually measureable) in the laboratory. An important example of this is described in Section 5.3. In the model, as just indicated, each target diode contribution to the total output current can be individually identified. Using this capability, the authors were able to determine the minimum area on the tube target which contributed to the output signal to noise ratio (SNR). By knowing this area, the required SNR of the input was found. The SNR, in turn, determines the size of the telescope required for the system. The model is a highly flexible tool useable for the understanding of the behavior of EBSICON's and for translating tube and operating parameters into performance information.

As described in Section 4.2, the model is implemented in three computer programs. One program simulates the actual video output current signal of the tube and as described in Section V is useable in determining resolution of two point sources in the presence of background, the square wave response of the tube and the point spread function of the tube. The other two programs are used to evaluate

the statistical performance of EBSICON's. The outputs of these programs are used to determine the probability of detection of various images in the presence of background noise, the probability of false alarms due to the noise and signal to noise ratio for various background noise levels.

Section V, in general, compares the results obtained from the model with experimental EBSICON data that was available at the time. It is shown there that all trend-like results of the model agree with experimental data. Further, for each experiment in which tube and operating parameters were better known, then when they were set to the same values in the model, quantitative agreement improved greatly. From this, it is felt that the implementations of the model encompass every EBSICON characteristic and operating mode of interest anticipated at this time.

The system designer can use the model by varying the parameters in a systematic manner to achieve predicted optimum overall system performance. Simultaneously, with the tubes available, pertinent experiments should be performed to insure agreement of results from the model and from the experiments. Examples included in this effort would be the determination of optimal read beam size and current, scan speed and gain magnitude for various images and background levels to achieve maximum probability of detection and minimum probability of false alarms while at the same time retaining compatibility with reasonable data rates. Having arrived at an optimal set of parameters, the required tube and camera system can be specified.

6.2 RECOMMENDATIONS

Currently, under the GEODSS program, the Night Vision Laboratory (NVL) of the Army is conducting a tube development program. Westinghouse in conjunction with Texas Instruments is providing EBSICON image tubes and yokes to NVL to be tested using NVL's laboratory camera system. The experiments will provide measured tube characteristics. Many characteristics or parameters such as beam width, target saturation illumination and the illumination value causing read-out beam limitation cannot be directly measured with an actual EBSICON. In fact the effects of the last two characteristics are difficult to separate by measurement. Many characteristics must be estimated which leads, in many cases, to inaccurate values of the actual physical parameters of the tubes. The tube model can be used to support NVL in improving the accuracy of the tube parameter estimates.

Operating parameters such as read-out speed, tube gain and read-out beam current determine how the tube and camera system effect the overall system performance. The influence of these parameters on system performance can be estimated from the model and a set of recommended operating settings can be determined.

Finally, the model can be used to assist in formulating the acceptance criteria for the image tube and camera systems which will be used. Specifically, it is recommended that the image tube model be used to:

1. Support the NVL activity. This support will consist of two activities.

First the model will be used to verify those tube parameters which can only be estimated. This shall be done by setting the parameters in the model to the estimated values for a set of experiments which have been or will be performed that clearly demonstrate the effects of the actual values. The operating parameters in the model are set to the values used in the experiments, and the model is then exercised. Since these parameters are clearly identified in the model, they will be varied systematically in the model until agreement of results from the model and from the experiments is good. The resultant values obtained from the model will provide accurate estimates of the actual values of the physical parameters of the tube.

Second, using the model as an analytical tool, additional experiments designed to improve the evaluation of the tube parameters will be identified and recommended.

2. Specify Operating Parameters. For tubes with acceptable physical parameters, the model will be used to establish the optimum set of operating parameters (such as read speed, gain, etc.) which yield the required system performance. In all cases performance requirements will be based upon probability of detection, probability of false alarms, lag, resolution, blooming, etc. and shall be compatible with reasonable video signal bandwidths. The model will be used to establish these factors, but they shall also be shown experimentally for each tube under selected illumination conditions.

3. Generate Acceptance Criteria and Performance Requirements for Image Tube and Camera Systems. The interrelation between the tube model and the tube development program, as discussed above, shall be the basis on which the EBSICON tube and camera system acceptance criteria are generated as part of the overall system specification. From the knowledge of EBSICON performance and its impact upon the overall system, performance requirements for other types of tube and camera systems will be generated. These will be of a generic nature such as point source resolution, modulation transfer function, two-dimensional point spread function, lag, dark current, sensitivity, microphonic effects, and signal and noise transfer relationships. All of these can be determined by laboratory measurements which are strongly influenced by experience with the tube model and EBSICON measurements.

APPENDIX A
SIMULATION PROGRAM LISTING

```

./ ADD SEQFLD=738
./ NUMBER NEW1=00000001, INCR=00000001
REAL*8 U/.3003003003/
IEB801I NM BLOCKSIZE ASSUMED 80.
      DIMENSION A(11,101),Q(21,21),Q0(21,21)
      INTEGER LN(3)/6,8,10/
      COMMON IBUF(1000)
      REAL NL(3)/600.,800.,1000./,L,I0,LN2
      REAL XT(3)/'X-AX','IS (','CM) '/,YT(2)/'LINE',' NO.'/,ZT(4)/'CURR'
1, 'ENT ','(AMP','S) '/
      REAL NE(2)/1.6019E-14,8.0095E-15/
      VMB=19.
      VMT=16.
      GAIN=100.
      NET=.32*10.** (9.-.4*VMT)
      I0=1.0E-6
      ALPHA=.0025
      BETA=.25E+15
      PI=3.14159265
      PIR=SQRT(PI)
      DA=9.375E-7
      FACJ=I0*DA/(PI*ALPHA**2)
      H=2.5
      T=1/17.5
      W=H
      X0=-.025
      I=1
      V=NL(I)*W/T
      TS=.02*T/NL(I)
      L=H/NL(I)
      LNH=LN(I)/2.
      LN2=LNH
      EPS=0.0
      DO 70 J=1,2
      DO 5 IQ=1,21
      DO 5 JQ=1,21
      Q(IQ,JQ)=0.0
5 CONTINUE
      DO 70 K=1,6
      DO 10 IQ=1,21
1016 DO 10 JQ=1,21
      Q(IQ,JQ)=Q(IQ,JQ)+NE(J)
      IF(K.NE.6)GO TO 10
      Q(IQ,JQ)=NE(J)
      10 Q0(IQ,JQ)=Q(IQ,JQ)
      WRITE(6,1011)
1011 FORMAT('1')
      DO 1010 JQ=1,21
      WRITE(6,1071) (Q(IQ,JQ),IQ=1,11)
      WRITE(6,1072) (Q(IQ,JQ),IQ=12,21)
1010 CONTINUE
      LNI=LN(I)+1

```



```

LNII=2.*LN(I)+1
DO 60 N=1,LNII
Y0=(N-LN(I)-1)*L+EPS
N1=N-LNH
DO 40 IT=1,201
TIME=(IT-1)*TS/200.
IM=IT-50
X=V*TIME+X0
C=0.0
IY0=11.5+Y0/.00125
IX0=11.5+X/.00125
DO 35 IQ=1,21
ISQ=IQ-IX0
IF(IABS(ISQ).GT.8)GO TO 35
XD=(IQ-11)*.00125
XI=XD-X
XIO=XD-X0
E=-(XI/ALPHA)**2
FACX=0.0
IF(E.GT.(-30.))FACX=EXP(E)
DO 30 JQ=1,21
IF(((JQ-IY0)**2+ISQ**2).GT.64)GO TO 30
YD=(JQ-11)*.00125
YJ=YD-Y0
E=-(YJ/ALPHA)**2
FACY=0.0
IF(E.GT.(-80.))FACY=EXP(E)
IF(Q(IQ,JQ))30,30,20
20 DQ=(IQ*FACY*DA/(2.*V*ALPHA*PIR))*(ERF(XI/ALPHA)-ERF(XIO/ALPHA))
FACI=1.0
Q(IQ,JQ)=ALOG(EXP(BETA*(Q0(IQ,JQ)+DQ))-EXP(BETA*DQ)+1.)/BETA
C=C+(1.-EXP(-BETA*Q(IQ,JQ)))*FACJ*FACI*FACX*FACY
30 CONTINUE
35 CONTINUE
IF(IM.LT.1.OR.IM.GT.101.OR.N1.LT.1.OR.N1.GT.LNII)GO TO 40
A(N1,IM)=C
40 CONTINUE
DO 50 IQ=1,21
DO 50 JQ=1,21
50 Q0(IQ,JQ)=Q(IQ,JQ)
60 CONTINUE
WRITE(6,61)J
61 FORMAT('1J=',I2/)
DO 1060 IT=1,101
1060 WRITE(6,1061)(A(N1,IT),N1=1,LNII)
1061 FORMAT(' ',1PE11.4,10(1X,1PE11.4))
WRITE(6,1062)
1062 FORMAT(1H1)
DO 1070 JQ=1,21
WRITE(6,1071)(Q(IQ,JQ),IQ=1,11)
1070 WRITE(6,1072)(Q(IQ,JQ),IQ=12,21)
1071 FORMAT(' ',11(1PE12.3))

```



```

1072 FORMAT(' ',10X,10(1PE10.3))
70 CONTINUE
CALL EXIT
END
FUNCTION RAND(X)
REAL*8 Y,X
DATA XM/100003./
Y=X*XM
M=Y
X=Y-M
RAND=X
RETURN
END
FUNCTION GAUS(U1,U2,VM8)
AM=2.*10.**(.9-.4*VM8)
GAUS=SQRT(-2.*AM*ALOG(U1))*COS(6.28185*U2)+AM
RETURN
END
IEB818I HIGHEST CONDITION CODE WAS 00000000
IEB819I END OF JOB IEBUPDTE.

```

APPENDIX B

STATISTICAL EVALUATION PROGRAM (NO. 1) LISTING

```

./ ADD SEQFLD=738
./ NUMBER NEW1=000000001, INCR=000000001
REAL*8 A1,A2,A3,B1,B2,B3,EI1,EI12,EI1I2,COV
IEB801I NM BLOCKSIZE ASSUMED 80.
1,PIR2,FACX1,FACX2,FACX3,DQ, GIR,EPS,FMAX,VM8
REAL*8 ARG,ARG1
REAL*8 FACY,IB1,DQ1,K1, M3,M4,M5,M6,FACX31,FACX21
REAL*8 IO,NL,L,IB,K,I1,I2,IR,MU,MEAN,AM,PI,FAC1,FAC2,SIG,V,VAR,X,Y
REAL*8 VMT,QT,MUT,SIGT,M1T,M2T,M3T,M4T,M5T,M6T,NET
REAL*8 EX,EXE,HKG,HNG,HKG1,HNG1,F,F2,F1,F12
REAL*8 Z1,YN,YN1,Z
REAL*8 A,GAMA,AR
REAL*8 M1(20,13),G(20,13),M2(20,13)
REAL*8 DQ,Q,KQ,FQ,FQ2,ARG2,ARG3,HQG,HQG2,M3(20,13)
DALOG(Z)=2.77*(IXTUV(Z,1,7)-64.)
GAIN=500.
VMB=19.
A1=2.*10.**(.9-.4*VMB)
B1=GAIN*1.6019D-19
ALPHA=.0025
BETA=3.E13
GAMA=4.42858E+11
A=BETA/GAMA
X0=-.025
PI=3.141592653599793D00
DA=9.375E-7
IO=2.E-6
FAC1=IO*DA/(PI*ALPHA**2)
H=2.5
NL=1000.
W=H
NO=0
L=H/NL
PIR2=DSQRT(2.*PI)
T=1./30.
V=NL*W/T
FAC2=IO*DA/(2.*V*ALPHA*DSQRT(PI))
ISTOP=13+NO
DO 3000 I=1,ISTOP
DO 3000 J=1,13
M2(I,J)=0.0
M3(I,J)=0.0
3000 CONTINUE
DO 3010 I=1,ISTOP
DO 3010 J=1,13
M1(I,J)=A1
G(I,J)=B1
MU=(1.-DEXP(-M1(I,J)*(1.-DEXP(-GAMA*B1))))/GAMA
VAR=(DEXP(-M1(I,J)*(1.-DEXP(-2.*GAMA*B1)))-DEXP(-2.*M1(I,J)*(1.-DEXP(-GAMA*B1))))/(GAMA**2)
VAR=VAR+M3(I,J)
MU=MU+M2(I,J)

```

```

M1(I,J)= (DLOG(1.-GAMA*MU)**2)/DLOG((1.-GAMA*MU)/(VAR*GAMA**2+(1.-
1GAMA*MU)**2))
G(I,J)=-DLOG(DLOG(VAR*GAMA**2+(1.-GAMA*MU)**2)/DLOG(1.-GAMA*MU)-1.
1)/GAMA
3010 CONTINUE
MEAN=0.0
VAR=0.0
COV=0.0
WRITE(6,11)
11 FORMAT('1',8X,'K',13X,'DQ', 9X,'M122', 9X,'M12',10X,'M2',10X,'M1',
110X,'MEAN',10X,'VAR',10X,'COV',7X,'% TERMS LDST')
DO 100 I=1,ISTOP
X=(I-7)*.00125
FACX1=FAC2*(DERF((X+X0)/ALPHA)-DERF((X-X0)/ALPHA))
FACX2=FAC2*(DERF(X/ALPHA)-DERF((X-X0)/ALPHA))
FACX21=FAC2*(DERF((X-N0*.00125)/ALPHA)-DERF((X-X0-N0*.00125)/ALPHA
1))
FACX3=FAC1*DEXP(-(X/ALPHA)**2)
FACX31=FAC1*DEXP(-((X-N0*.00125)/ALPHA)**2)
DO 90 J=1,13
Y=(J-7)*.00125
FACY=DEXP(-(Y/ALPHA)**2)
IB1=FACX31*FACY
IB=FACX3*FACY
DQQ=0.0
DQ=FACX2*FACY
DQ1=FACX21*FACY
DO 10 N=1,5
DQ1=DQ1+FACX1*DEXP(-((Y+N*L)/ALPHA)**2)
DQ=DQ+FACX1*DEXP(-((Y+N*L)/ALPHA)**2)
10 CONTINUE
DO 20 N=1,10
DQQ=DQQ+FACX1*DEXP(-((Y-(N-5)*L)/ALPHA)**2)
20 CONTINUE
KQ=DEXP(BETA*DQQ)
K=DEXP(BETA*DQ)
K1=DEXP(BETA*DQ1)
AM=M1(I,J)
M=AM+4.*DSQRT(AM)+.5
EXE=0.0
IF(AM.GT.(173.))EXE=173.-AM
IF(M.GT.346)WRITE(6,6)
6 FORMAT(' MEAN PHOTOELECTRONS GREATER THAN ALLOWED')
NSTOP=M
IF(M.GT.173)NSTOP=173
EX=-AM
IF(EXE.LT.(0.0))EX=-173.
Z1=DEXP(EXE)
EQ=0.0
EQ2=0.0
F=0.0
F2=0.0

```

```

F1=0.0
F12=0.0
KOUNT=0
YN=DEXP(EX)
DO 2035 N=1,NSTOP
YN=YN*(AM/N)
AR=-N*G(I,J)*GAMA
ARG=-A
IF(AR.GT.(-173.))ARG=-A*(1.-DEXP(AR))
ARG1=0.0
IF(ARG.GT.(-173.))ARG1=DEXP(ARG)
ARG2=1.0
IF((DALOG(KQ)+DALOG(ARG1-1.)).GT.(-173.))ARG2=KQ*(ARG1-1.)+1.
ARG3=DLOG(ARG2)
HQG=0.0
IF((DALOG(ARG3)+DALOG(1./BETA)).GT.(-173.))HQG=ARG3/BETA
HQG2=0.0
IF((2.*DALOG(HQG)).GT.(-173.))HQG2=HQG**2
HKG=(K*(1.-ARG1))/(K+(1.-K)*ARG1)
HKG1=(K1*(1.-ARG1))/(K1+(1.-K1)*ARG1)
HNG=0.0
IF((2.*DALOG(HKG)).GT.(-173.))HNG=HKG**2
HNG1=0.0
IF((DALOG(HKG)+DALOG(HKG1)).GT.(-173.))HNG1=HKG*HKG1
2003 FM=0.0
XTEST=DALOG(YN)+DALOG(Z1)
IF(XTEST.GT.(-173.))FM=YN*Z1
IF((XTEST+DALOG(HQG)).GT.(-173.))FQ=FQ+FM*HQG
IF((XTEST+DALOG(HQG2)).GT.(-173.))FQ2=FQ2+FM*HQG2
IF((XTEST+DALOG(HKG)).GT.(-173.))F=F+FM*HKG
IF((XTEST+DALOG(HKG1)).GT.(-173.))F1=F1+FM*HKG1
IF(HNG.EQ.(0.0))GO TO 1010
IF((XTEST+DALOG(HNG)).GT.(-173.))F2=F2+FM*HNG
1010 IF(HNG1.EQ.(0.0))GO TO 2035
IF((XTEST+DALOG(HNG1)).GT.(-173.))F12=F12+FM*HNG1
EXPON=1.20412*IABS(IXTUV(F2,1,7)-IXTUV(FM,1,7)-IXTUV(HNG,1,7)+64)
IF(EXPON.LT.(16.))GO TO 2035
KOUNT=KOUNT+1
WRITE(6,2009)EXPON
2009 FORMAT(' EXPONENT DIFFERENCE=',1PE13.6)
2035 CONTINUE
IF(M.LE.173)GO TO 2090
YN1=1.
DO 2080 N=174,M
YN1=YN1*(AM/N)
AR=-N*G(I,J)*GAMA
ARG=-A
IF(AR.GT.(-173.))ARG=-A*(1.-DEXP(AR))
ARG1=0.0
IF(ARG.GT.(-173.))ARG1=DEXP(ARG)
ARG2=1.0
IF((DALOG(KQ)+DALOG(ARG1-1.)).GT.(-173.))ARG2=KQ*(ARG1-1.)+1.

```

```

ARG3=DLOG(ARG2)
HQG=0.0
IF((DLOG(ARG3)+DLOG(1./BETA)).GT.(-173.))HQG=ARG3/BETA
HQG2=0.0
IF((2.*DLOG(HQG)).GT.(-173.))HQG2=HQG**2
HKG=(K*(1.-ARG1))/(K+(1.-K)*ARG1)
HKG1=(K1*(1.-ARG1))/(K1+(1.-K1)*ARG1)
HNG=0.0
IF((2.*DLOG(HKG)).GT.(-173.))HNG=HKG**2
HNG1=0.0
IF((DLOG(HKG)+DLOG(HKG1)).GT.(-173.))HNG1=HKG*HKG1
2040 FM=0.0
XTEST=XTEST+DLOG(YN1)
IF((XTEST+DLOG(HQG)).GT.(-173.))FQ=FQ+FM*HQG
IF((XTEST+DLOG(HQG2)).GT.(-173.))FQ2=FQ2+FM*HQG2
IF(XTEST.GT.(-173.))FM=YN*YN1*Z1
IF((XTEST+DLOG(HKG)).GT.(-173.))F=F+FM*HKG
IF((XTEST+DLOG(HKG1)).GT.(-173.))F1=F1+FM*HKG1
IF(HNG.EQ.(0.0))GO TO 1020
IF((XTEST+DLOG(HNG)).GT.(-173.))F2=F2+FM*HNG
1020 IF(HNG1.EQ.(0.0))GO TO 2080
IF((XTEST+DLOG(HNG1)).GT.(-173.))F12=F12+FM*HNG1
EXPON=1.20412*ABS(IXTUV(F2,1,7)-IXTUV(FM,1,7)-IXTUV(HNG,1,7)+54)
IF(EXPON.LT.(16.))GO TO 2080
KOUNT=KOUNT+1
WRITE(6,2009)EXPON
2080 CONTINUE
2090 EI1=0.0
PERCNT=KOUNT*100./M
IF((DLOG(IB)+DLOG(F)).GT.(-173.))EI1=IB*F
EI12=0.0
IF((2.*DLOG(IB)+DLOG(F2)).GT.(-173.))EI12=IB*IB*F2
EI2=0.0
IF((DLOG(IB1)+DLOG(F1)).GT.(-173.))EI12=IB1*F1
EI12=0.0
IF((DLOG(IB)+DLOG(IB1)+DLOG(F12)).GT.(-173.))EI12=IB*IB1*F12
M2(I,J)=FQ
M3(I,J)=FQ2
IF((2.-DLOG(FQ)).GT.(-173.))M3(I,J)=M3(I,J)-FQ**2
MEAN=MEAN+EI1
VAR=VAR+EI12
COV=COV+EI12
IF((2.*DLOG(EI1)).GT.(-173.))VAR=VAR-EI1**2
IF((DLOG(EI1)+DLOG(EI2)).GT.(-173.))COV=COV-EI1*EI2
WRITE(6,12)K,DQ,EI12,EI2,EI1,MEAN,VAR,COV,PERCNT
12 FORMAT(' ',9(1PD13.6),3X,F6.3)
90 CONTINUE
100 CONTINUE
STDV=DSQRT(VAR)
COREL=1.0
IF(VAR.GT.(10.**(-70)))COREL=COV/VAR
WRITE(6,101)AM,MEAN,STDV,COREL

```

101 FORMAT(' AM=',1PD13.6,' MEAN=',1PD13.6,' ST. DEV.=',1PE13.6,' CORR
RELATION COEF.=',1PE13.6)

110 CONTINUE

CALL EXIT

END

IEB818I HIGHEST CONDITION CODE WAS 00000000

IEB819I END OF JOB IEBUPDTE.

APPENDIX C

STATISTICAL EVALUATION PROGRAM (NO. 2) LISTING

```

./ ADD SEQFLD=738
./ NUMBER NEW1=00000001, INCR=00000001
REAL*8 A1,A2,A3,B1,B2,B3,S11,S112,S1112,COV
IEB8011 NM BLOCKSIZE ASSUMED 30.
REAL*8 ARG,ARG1
REAL*8 FAC1,IB1,DQ1,K1, M3,M4,M5,M6,FACX31,FACX21
REAL*8 IO,NL,L,IB,N,I1,I2,IR,MJ,MEAN,AM,PI,FAC1,FAC2,SIG,V,VAR,X,Y
1,PIR2,FACX1,FACX2,FACX3,D2, GIR,EPS,FMAX,VMB
REAL*8 VMT,QT,MUT,SIGT,M1T,M2T,M3T,M4T,M5T,M6T,NET
REAL*8 EX,EXE,HKG,HNG,HKG1,HNG1,F,F2,F1,F12
REAL*8 Z1,YN,YN1,Z
REAL*8 A,GAMA,AR
REAL*8 M1(12,13),G(13,13),M2(13,13)
REAL*8 DQ,K,FQ,FQ2,ARG2,ARG3,HJG,HJG2,M3(13,13)
DALUS(Z)=2.77*(IXTUV(Z,1,7)-64.)
GAIN=500.
VMT=16.
VMB=19.
A1=2.*10.**(.9-.4*VMB)
A2=.32*10.**(.9-.4*VMT)
B1=GAIN*1.6019D-19
DO 3000 I=1,I2
DO 3000 J=1,I3
M2(I,J)=0.0
M3(I,J)=0.0
3000 CONTINUE
ALPHA=.0025
BETA=3.513
GAMA=4.423585+11
A=4*BETA/GAMA
X0=-.025
PI=3.141592653589793D00
DA=9.375E-7
IO=2.E-6
FAC1=IO*DA/(PI*ALPHA**2)
NL=1000.
H=2.5
W=H
NDL=7
L=H/NL
PIR2=DSQRT(2.*PI)
T=1./30.
DO 3010 I=1,I3
DO 3010 J=1,I3
M1(I,J)=A1
IF(I.EQ.7.AND.J.EQ.7)M1(I,J)=A1+A2
G(I,J)=B1
MU=(1.-DEXP(-M1(I,J)*(1.-DEXP(-GAMA*B1))))/GAMA
VAR=(DEXP(-M1(I,J)*(1.-DEXP(-2.*GAMA*B1)))-DEXP(-2.*M1(I,J)*(1.-DEXP(-GAMA*B1))))/(GAMA**2)
MU=MU+M2(I,J)
VAR=VAR+M3(I,J)

```

```

M1(I,J)= (DLOG(1.-GAMA*MU)**2)/DLOG((1.-GAMA*MU)/(VAR*GAMA**2+(1.-
1GAMA*MU)**2))
G(I,J)=-DLOG(DLOG(VAR*GAMA**2+(1.-GAMA*MU)**2)/DLOG(1.-GAMA*MU)-1.
1)/GAMA
3010 CONTINUE
MEAN=0.0
VAR=0.0
V=VL*W/T
FAC2=IO*DA/(2.*V*ALPHA*DSQRT(PI))
WRITE(6,11)
11 FORMAT('1',8X,'K',14X,'DQ',10X,'M12',12X,'M1',12X,'MEAN',12X,'VAR'
1,6X,'% TERMS EXCLUDED')
DO 100 I=1,13
X=(I-7)*.00125
FACX1=FAC2*(DERF((X+X0)/ALPHA)-DERF((X-X0)/ALPHA))
FACX2=FAC2*(DERF(X/ALPHA)-DERF((X-X0)/ALPHA))
FACX3=FAC1*DEXP(-(X/ALPHA)**2)
DO 90 J=1,13
Y=(J-7)*.00125
FACY=DEXP(-(Y/ALPHA)**2)
IB=FACX3*FACY
DQ0=0.0
DQ=FACX2*FACY
DO 10 N=1,5
DQ=DQ+FACX1*DEXP(-((Y+N*L)/ALPHA)**2)
10 CONTINUE
DO 20 N=1,10
DQ0=DQ0+FACX1*DEXP(-((Y-(N-5)*L)/ALPHA)**2)
20 CONTINUE
KQ=DEXP(BETA*DQ0)
K=DEXP(BETA*DQ)
AM=M1(I,J)
M=AM+4.*DSQRT(AM)+.5
EXE=0.0
IF(AM.GT.(173.))EXE=173.-AM
IF(M.GT.345)WRITE(6,6)
6 FORMAT(' MEAN PHOTOELECTRONS GREATER THAN ALLOWED')
NSTOP=M
IF(M.GT.173)NSTOP=173
EX=-AM
IF(EXE.LT.(0.0))EX=-173.
Z1=DEXP(EXE)
EQ=0.0
EQ2=0.0
F=0.0
F2=0.0
F1=0.0
F12=0.0
KOUNT=0
YN=DEXP(EX)
DO 2035 N=1,NSTOP
YN=YN*(AM/N)

```

```

AR=-N*G(I,J)*GAMA
ARG=-A
IF(AR.GT.(-173.))ARG=-A*(1.-DEXP(AR))
ARG1=0.0
IF(ARG.GT.(-173.))ARG1=DEXP(ARG)
ARG2=1.0
IF((DALOG(KQ)+DALOG(ARG1-1.)).GT.(-173.))ARG2=KQ*(ARG1-1.)+1.
ARG3=DLOG(ARG2)
HQG=0.0
IF((DALOG(ARG3)+DALOG(1./BETA)).GT.(-173.))HQG=ARG3/BETA
HQG2=0.0
IF((2.*DALOG(HQG)).GT.(-173.))HQG2=HQG**2
HKG=(K*(1.-ARG1))/(K+(1.-K)*ARG1)
HNG=0.0
IF((2.*DALOG(HKG)).GT.(-173.))HNG=HKG**2
2008 FM=0.0
XTEST=DALOG(YN)+DALOG(Z1)
IF((XTEST+DALOG(HQG)).GT.(-173.))FQ=FQ+FM*HQG
IF((XTEST+DALOG(HQG2)).GT.(-173.))FQ2=FQ2+FM*HQG2
IF(XTEST.GT.(-173.))FM=YN*Z1
IF((XTEST+DALOG(HKG)).GT.(-173.))F=F+FM*HKG
IF(HNG.EQ.(0.0))GO TO 2035
IF((XTEST+DALOG(HNG)).GT.(-173.))F2=F2+FM*HNG
EXPON=1.20412*1ABS(IXTUV(F2,1,7)-IXTUV(FM,1,7)-IXTUV(HNG,1,7)+04)
IF(EXPON.LT.(16.))GO TO 2035
KOUNT=KOUNT+1
WRITE(6,2009)EXPON
2009 FORMAT(' EXPONENT DIFFERENCE=',1P13.6)
2035 CONTINUE
IF(M.LE.173)GO TO 2040
YN1=1.
DO 2030 N=174,M
YN1=YN1*(AM/N)
AR=-N*G(I,J)*GAMA
ARG=-A
IF(AR.GT.(-173.))ARG=-A*(1.-DEXP(AR))
ARG1=0.0
IF(ARG.GT.(-173.))ARG1=DEXP(ARG)
ARG2=1.0
IF((DALOG(KQ)+DALOG(ARG1-1.)).GT.(-173.))ARG2=KQ*(ARG1-1.)+1.
ARG3=DLOG(ARG2)
HQG=0.0
IF((DALOG(ARG3)+DALOG(1./BETA)).GT.(-173.))HQG=ARG3/BETA
HQG2=0.0
IF((2.*DALOG(HQG)).GT.(-173.))HQG2=HQG**2
HKG=(K*(1.-ARG1))/(K+(1.-K)*ARG1)
HNG=0.0
IF((2.*DALOG(HKG)).GT.(-173.))HNG=HKG**2
2040 FM=0.0
XTEST=XTEST+DALOG(YN1)
IF((XTEST+DALOG(HQG)).GT.(-173.))FQ=FQ+FM*HQG
IF((XTEST+DALOG(HQG2)).GT.(-173.))FQ2=FQ2+FM*HQG2

```

```

IF(XTEST.GT.(-173.))FM=YN*YN1*Z1
IF((XTEST+DALOG(HKG)).GT.(-173.))F=F+FM*HKG
IF(HNG.EQ.(0.0))GO TO 2080
IF((XTEST+DALOG(HNG)).GT.(-173.))F2=F2+FM*HNG
EXPON=1.20412*IABS(IXTUV(F2,1,7)-IXTUV(FM,1,7)-IXTUV(HNG,1,7)+64)
IF(EXPON.LT.(16.))GO TO 2080
KOUNT=KOUNT+1
WRITE(6,2009)EXPON
2080 CONTINUE
2090 EI1=0.0
PERCNT=KOUNT*100./M
IF((DALOG(IB)+DALOG(F)).GT.(-173.))EI1=I3*F
EI12=0.0
IF((2.*DALOG(IB)+DALOG(F2)).GT.(-173.))EI12=I3*I3*F2
M2(I,J)=F2
M3(I,J)=F2
IF((2.*DALOG(F2)).GT.(-173.))M3(I,J)=M3(I,J)-F2**2
MEAN=MEAN+EI1
VAR=VAR+EI12
IF((2.*DALOG(EI1)).GT.(-173.))VAR=VAR-EI1**2
WRITE(6,12)K,00,EI12,EI1,MEAN,VAR,PERCNT
12 FORMAT(' ',5(1X,1PD13.5),1X,F5.3)
90 CONTINUE
100 CONTINUE
STDV=DSORT(VAR)
WRITE(6,101)AM,MEAN,STDV
101 FORMAT(' AM=',1PD13.6,' MEAN=',1PD13.6,' ST. DEV.=',1PD13.6)
110 CONTINUE
CALL EXIT
END

```

IEB318I HIGHEST CONDITION CODE WAS 00000000

IEB819I END OF JOB ICRUPDT.

REFERENCES

1. W. Kleen, and R. Muller; Laser; Springer-Verlag Berlin/Heidelberg, 1969.
2. R. J. Glauber; Photon Correlations, Physical Review Letters 10, (1963), 84-86.
3. F. A. Haight; Handbook of the Poisson Distribution; John Wiley & Sons, New York, 1967.
4. I. S. Gradshteyn and Im. M. Ryzhik; Table of Integrals, Series and Products; Academic Press, N. Y. and London, 1965.